THÈSE

En vue de l'obtention du

DOCTORAT DE L'UNIVERSITÉ DE TOULOUSE

Délivré par :

Institut National Polytechnique de Toulouse (Toulouse INP)

Discipline ou spécialité :

Génie Electrique

Présentée et soutenue par :

M. ANDRE MRAD

le lundi 24 octobre 2022

Titre :

Moteur à Flux Axial à Aimants Permanents et à Concentration de Flux : Réalisation, Mesure de Paramètres Statiques et Modèle Numérique 3D

Ecole doctorale :

Génie Electrique, Electronique, Télécommunications (GEETS)

Unité de recherche :

Laboratoire Plasma et Conversion d'Energie (LAPLACE)

Directeur(s) de Thèse :

M. YVAN LEFEVRE

M. JEAN-FRANCOIS LLIBRE

Rapporteurs :

M. JEAN-FREDERIC CHARPENTIER, ECOLE NAVALE

MME CAROLE HENAUX, UNIVERSITE DE MONTPELLIER

Membre(s) du jury :

M. STÉPHANE CLENET, ENSAM LILLE, Président

M. JEAN-FRANCOIS LLIBRE, TOULOUSE INP, Invité(e)

M. JÉRÔME CROS, UNIVERSITE LAVAL, Membre

M. MOHAMAD ARNAOUT, UNIVERSITE LIBANAISE, Invité(e)

M. NELSON SADOWSKI, UNIV.FED.DE SANTA CATARINA FLORIANOPOLIS, Membre

M. YVAN LEFEVRE, TOULOUSE INP, Membre

Acknowledgement

The presented work has been carried out in the research group *GREM3* "Groupe de Recherche en Electrodynamique" at LAPLACE laboratory “LAboratoire PLAsma et Conversion d’Energie” in the “Institut National Polytechnique de Toulouse-INPT”.

First of all, I would like to thank my thesis director Mr. Yvan Lefèvre - CNRS research fellow for entering me to the scientific research world. As well as through directing my work and for helping me to reach this end. I will never forget his scientific and human qualities which contributed enormously to the progression of my research work. Always he was and still my reference.

Special thanks for my co-directors Mr. Jean-François Llibre - Associate Professor in Toulouse University II who shared with him the same office along this journey, for his guidance, scientific knowledge and the jovial spirit. As well as Mr. Mohamad Arnaout - Associate Professor in the Lebanese International University and who was the godfather for my thesis and the academic relation between the two universities. Not forgetting his academic and research experiences especially in contributing and directing me along this journey. My knowledge by him started in 2016 once I was a student in his Masters classes and performing my Masters research also under his supervision. Always I consider him that he’s my great brother who refer to him in all situations.

I would like also to express my sincere thanks to Mr. Dominique Harribey – CNRS research engineer for the realization of our prototype in this thesis and by helping us on the test benchmark. Not forgetting his fruitful spirit as well as the deep technical experience in the electrical machinery domain indeed to his knowledge and discussions.

I would like to thank the reporters of my thesis, Professor Carole Henaux - University of Montpellier as well as the HDR/Assistant Professor Jean-Frédéric Charpentier - French Naval Academy Research Institute for accepting to evaluate and report my work. Indeed, a grateful thanks for the examiners who exanimate my PhD, Professor Jérôme CROS - Laval University-Canada, as well as for Professor Nelson Sadowski - Federal University of Santa Catarina-Brazil. I sincerely thank Professor Stéphane Clenet - Arts et Métiers - Institut de Technologie/L2EP-Lille, with a great honor who accepts to be the president of my thesis jury.

Not forgetting to send my deep thanks to Professor François Pigache who was the second godfather in this relation who arranged my coming to France and also for teaching with him in the INP Toulouse-ENSEEIHT.

Of course, I do not forget to thank my doctors in the Lebanese International University who was always encourage me in this thesis and give me their advices in my daily life: Ziad Noun and Khaled Al-Khatib.

Now, I would like to specially thank my colleagues: Maxime Bonnet, Sarah Touhami and Theo Carpi on their scientific and constructive discussions once I entered to the LAPLACE laboratory as well as to the happy moments spent it with them. I also thank the PhD students: Jessica, Zakaria, Ayoub, Léonard, Marion, Sophie…

I also address my respectful thanks to my nearest friends with whom I spent happy moments during the years of my PhD who was the base for me in Toulouse as well as source of encouragement and confidence. Among these people, I thank: Mohammad Issa, Abbas Hamadi, Bilal Fakih, Mohanad Alchaar and Andrea Al Haddad. Indeed, to my other friends: Kassem Asfour, Hamoud Younes, Loreine Makki and Noemi Lanciotti.

Finally, a heartfelt thanks for the persons who have supported me in all this journey as well as due to the geographical distance that separates us. Those persons are my parents Georges and Eidi, my brothers Nicolas, Elie and my sister Rita who shared with them my joys and worries. I hope that I achieved what they're waiting from me and also to be proud from what I did.

Of course, I will always try to reach the "Never-Ending Perfection".

Abstract

Green energy or sources with zero-carbon emissions plays a leading role in the worldwide electrification. Electric machinery field is a subject of attention leading to the green technology. These machines contribute mainly in the context of industrial applications as electric or hybrid cars. Avoiding the issue and price of rare-earth magnets, potential researches contribute particularly to non-rare-earth machines. For that reasons, this thesis studies the ferrite motor through the 'Spoke Type Axial Flux Permanent Magnet' (STAFPM) topology. One from the main interesting properties of this motor is the capability of the no-load magnetic flux concentration in its airgap.

The properties of this motor with ferromagnetic poles in the rotor are not so-well known. The present thesis focuses on studying its performances. Achieving this goal, consists firstly by doing a review on the analytical and numerical sizing approaches applied for radial and axial flux machines based on the magnetic field models and as well as, a review on the experimental test benchmark for salient-pole machines which provide us the identification and computation of the electromechanical parameters. Finally, a revision takes place on the 3D magnetic field modeling for sizing purposes. Thus the first section is partially devoted to review the application of the 3D finite difference method for axial machines which is a main objective in this thesis.

Afterwards, using a 1D analytical model, a performance comparison takes place between a single stator-single rotor STAFPM motor and a reference Surface Mounted Axial Flux Permanent Magnet (SMAFPM) motor. This comparison is made on the electromagnetic torque and at unified parameters. Consequently, new STAFPM prototype is sized by a consideration of some magnetic constraints. This prototype takes place on a test bench. An original method of the experimental identification of the parameters of the lumped parameter electromechanical model is developed. This method is based on the static torque measurement as a function of the rotor position.

A 3D numerical magnetic field model of the STAFPM motor is proposed. This tool studies the no-load magnetic field as well as the armature reaction fields. An original flux calculation method in the framework of the magnetic scalar potential formulation is developed. This method allows the quick calculation of the parameters of the lumped electromechanical model. The calculated parameters are compared to the experimentally identified parameters.

Résumé

L'énergie renouvelable ou les sources à zéro émission de carbone jouent un rôle de premier plan dans l'électrification mondiale. Le domaine des machines électriques fait l'objet d'une attention particulière dans le cadre de la technologie verte. Ces machines y contribuent principalement dans le contexte des applications industrielles comme des voitures électriques ou hybrides. Pour éviter les problèmes d'approvisionnement et de coût des aimants terres-rares, des recherches sont effectuées sur des machines sans aimants terres-rares. Pour ces raisons, cette thèse étudie le moteur à basé d'aimants ferrite. La topologie est celle du moteur à aimants permanents à flux axial avec concentration de flux, appelé en anglais « Spoke-Type Axial Flux Permanent Magnet » (STAFPM). L'une des principales propriétés intéressantes de ce moteur est la capacité de concentration du flux magnétique à vide dans son entrefer.

Les propriétés de ce moteur avec la présence de pièce ferromagnétiques au rotor ne sont pas aussi bien connues. La présente thèse se concentre donc sur l'étude de ses performances. Pour atteindre ce but, tout d'abord un état de l'art des approches de dimensionnement appliquées aux machines à flux radial et axial basées sur les modèles analytiques de champ magnétique est effectué. De même les états de l'art sur les tests expérimentaux des machines à pôles saillants permettant d'identifier les paramètres statiques et la modélisation 3D du champ magnétique à des fins de dimensionnement sont remis à jour. La première section est aussi partiellement consacrée à une revue de l'application de la méthode des différences finies 3D pour les machines axiales qui est un objectif principal de cette thèse.

Dans cette thèse, via un modèle analytique 1D, une comparaison des performances est faite entre un moteur mono-entrefer « STAFPM » et un moteur axial à aimants montés en surface, pris comme référence nommé en anglais « Surface Mounted Axial Flux Permanent Magnet » (SMAFPM). Cette comparaison est effectuée sur la base du couple électromagnétique. En conséquence, le nouveau prototype STAFPM est dimensionné en tenant compte de certaines contraintes magnétiques. Ce prototype prend place sur un banc d'essais. Une méthode originale de détermination des paramètres statiques du modèle électromécanique à constante localisées en anglais « lumped parameter electromechanical model » est mise au point. Cette détermination est basée sur la mesure du calcul du couple statique en fonction de la position du rotor.

Un modèle numérique 3D du champ magnétique dans le moteur STAFPM est proposé. Cet outil permet d'étudier le champ magnétique à vide ainsi que les champs de réaction de l'induit. Une méthode originale de calcul du flux magnétique dans le cadre d'une formulation en potentiel scalaire magnétique est développée. Cette méthode permet de calculer de manière très rapide les paramètres statiques du modèle électromécanique. Les paramètres calculés sont comparés aux paramètres identifiés expérimentalement.

Table of contents

Acknowledgement **3**

Abstract **5**

Résumé **6**

Table of contents **7**

List of Figures **12**

List of Tables **16**

General Introduction **17**

Chapter 1 State of the art **19**

1.1 Introduction 19

1.2 Sizing methods and magnetic field models 20

1.2.1 Quick sizing and simple analytical open circuit field model 20

1.2.2 Analytical open circuit field models 20

1.2.3 Numerical magnetic field models for sizing purpose 21

1.3 Experimental bench for salient pole machines 21

1.4 3D numerical magnetic model for sizing purpose 23

1.4.1 3D finite difference method 23

1.4.2 Specific boundary conditions 24

1.4.3 Distribution function of conductors 24

1.4.4 Electric parameters calculation 25

1.5 Conclusion 27

Chapter 2 Spoke Type Permanent Magnet Axial Flux Motor Prototype Sizing **29**

2.1 Introduction 29

2.2 General description of the existing axial flux motor 30

2.2.1 Stator 30

2.2.2 Rotor 32

2.3 Evaluation of the magnetic loads of the existing motor 34

2.3.1 No-load magnetic flux density in the airgap 34

2.3.2 No-load magnetic flux density in the stator iron 36

2.4 Characterization of the armature reaction 37

2.4.1 Thermal loads 37
2.4.2 Surface current density 38
2.5 Synthesis of the evaluation of the existing motor 39
2.6 Specifications for the new STAFPM prototype 40
2.7 Joint sizing of SMAFPM and STAFPM for comparison 41
2.7.1 Arc pole coefficient 41
2.7.2 Armature reaction 43
2.7.3 No-load magnetic flux density in the stator and the airgap 43
2.7.4 Sizing the SMAFPM rotor 44
2.7.5 Sizing the STAFPM rotor 46
2.7.6 Comparison of The SMAFPM and STAFPM motors 51
2.7.7 Conclusion of the comparative study 54
2.8 Choice of the new STAFPM prototype 54
2.9 Conclusion 57
Chapter 3 Experimental Studies of the STAFPM prototype 59
3.1 Introduction 59
3.2 STAFPM prototype 60
3.3 Electromechanical lumped parameter model 61
3.3.1 Electrical and mechanical quantities 62
3.3.2 Electrical equations 62
3.3.3 Flux-current relation 62
3.3.4 Mechanical equations 62
3.3.5 System of electromechanical equations 63
3.4 Symmetrical motor 63
3.4.1 Symmetries of the no-load flux 64
3.4.2 Symmetries of the self-inductances 64
3.4.3 Symmetries of the mutual inductances 65
3.5 Identification method of the torque model parameters 65
3.5.1 Identification of the derivative of the matrix inductance 66
3.5.2 Identification method of the cogging torque 67
3.5.3 Identification method of the derivative of no-load flux 67

3.6 Identification of the flux model parameters 67
3.6.1 Identification method of the no-load flux 68
3.6.2 Identification method of the self-inductances 68
3.6.3 Identification method of the mutual inductances 68
3.7 Experimental test bench 69
3.8 Numerical treatments of the results of measurements 71
3.9 Static torque measurements without permanent magnets 74
3.9.1 First experimental observations 74
Study around the position: $R3$ aligned with the iron pole 75
Study around the position: $R3$ facing the magnet 77
3.9.2 Single phase supply 79
3.9.3 Double phase supply 82
3.9.4 Conclusion of the tests without permanent magnets 85
3.10 Measurements with permanent magnets 85
3.10.1 Cogging torque 85
3.10.2 Derivative of the no-load flux 87
3.10.3 Conclusion 88
3.11 Validation of the identified torque model parameters 88
3.11.1 Without permanent magnets and three phase supply 88
3.11.2 With permanent magnets and single phase supply 90
3.11.3 With permanent magnets and double phase supply 91
3.11.4 With permanent magnets and three phase supply 92
3.12 Electrical measurements 94
3.12.1 No-load flux 94
3.12.2 Self and mutual inductances 94
3.12.3 Conclusion 96
3.13 Study of three phase sinusoidal supplies 96
3.13.1 DQ0 Model 96
3.13.2 Optimal torque per Ampere by the DQ0 model 99
3.13.3 Optimal torque per Ampere by the lumped parameter model 101
3.14 Conclusion 102

Chapter 4 3D NUMERICAL SIZING MODEL of STAFPM MOTOR 105

4.1 Introduction 105

4.2 Nomenclature 106

4.3 Magnetostatic field problem 107

4.4 Modeling the stator 109

4.4.1 Linear conductor distribution function 109

4.4.2 Surface current density wave 111

4.4.3 Surface current density distribution for armature reaction field problems 112

4.5 Magnetic scalar potential formulation 113

4.5.1 Airgap 114

4.5.2 Permanent magnet 115

4.5.3 Ferromagnetic pole 115

4.5.4 Nonmagnetic media 115

4.6 Continuity conditions with the ferromagnetic pole 115

4.7 Continuity conditions with the permanent magnet 116

4.8 Boundary without magnetic sources 117

4.9 Finite Difference Grid 118

4.10 Finite difference equations 121

4.10.1 FDE in interior nodes 121

4.10.2 FDE on interfaces with the ferromagnetic pole 122

4.10.3 FDE on interfaces with the permanent magnet 123

4.10.4 FDE on boundaries without magnetic sources 123

4.11 Open circuit magnetic field problem 124

4.11.1 FDE on stator bore 124

4.11.2 FDE on eastern boundary surface 124

4.11.3 FDE on western boundary surface 124

4.12 Direct armature reaction magnetic field problem 125

4.12.1 FDE on stator bore 125

4.12.2 FDE on eastern boundary surface 125

4.12.3 FDE on western boundary surface 125

4.13 Quadrature armature reaction magnetic field problem 125

4.13.1 FDE on stator bore 126
4.13.2 FDE on eastern boundary surface 126
4.13.3 FDE on western boundary surface 126
4.14 3DFDM4STAFPM software 126
4.14.1 Input data 127
4.14.2 Pre-processor 129
4.14.3 Processor 129
4.14.4 Post-processor 129
4.15 Flux model of integer distributed winding 131
4.15.1 Elementary flux 132
4.15.2 Flux in one phase 133
4.15.3 No-load and direct armature flux 133
4.15.4 Quadrature armature reaction flux 134
4.16 DQ model parameters 134
4.16.1 Distribution of the axial magnetic flux density on stator bore 135
4.16.2 Flux in function of the rotor position 138
4.16.3 Park's transformation 139
4.17 Conclusion 142
General conclusion 143
References 145

List of Figures

Figure 2-1: A photography of the stator of the existing SMAFPM 30
Figure 2-2: B(H) curve of the electrical steel M235-35A..... 31
Figure 2-3:Stator main parameters 31
Figure 2-4: A photography of the existing SMAFPM rotor 32
Figure 2-5: Intrinsic recoil curve $B(H)$ of Ferrite magnet 33
Figure 2-6: B(H) curve of the electrical steel XC12..... 33
Figure 2-7: Study domain for the evaluation of the air gap flux density..... 34
Figure 2-8: Closed path to apply Ampere's law..... 35
Figure 2-9: Flux conservation law applied on airgap and magnet surfaces S_g and S_m.. 33
Figure 2-10: Magnetic flux pattern on one pole of the existing motor..... 36
Figure 2-11: Distribution of the conductors of phase 1 along stator bore at mean radius 38
Figure 2-12: Linear distribution of conductors or distribution function of conductors... 38
Figure 2-13: Airgap magnetic flux density waveform 41
Figure 2-14: *Magnitude of the fundamental of $B_g(\theta)$ versus β for $B_{zg} = 1.0\ T$* 42
Figure 2-15: Inverse Total Harmonic Distortion τ_f versus β 43
Figure 2-16: $(B_{ty})_{max}$ versus β for SMAFPM motor.....45
Figure 2-17: Flow-chart to calculate the main sizes of the rotor of SMAFPM motor and the electromagnetic torque versus the arc pole coefficient *46*
Figure 2-18: Geometric parameters for one pair of poles for STAFPM..... *46*
Figure 2-19: Study domain for the evaluation of the airgap flux density.....*47*
Figure 2-20: Closed path to apply Ampere's law..... 47
Figure 2-21: Flux conservation law on airgap half surface S_g and magnet surface S_m.. 48
Figure 2-22: B_{ty}^{max} versus β for STAFPM motor 49
Figure 2-23: Flow-chart to calculate the main sizes of the rotor and the electromagnetic torque versus the arc pole coefficient β..... 50
Figure 2-24: Comparison of electromagnetic torque $C_{em}(\beta)$..... 51
Figure 2-25: Comparison of magnetic flux density in permanent magnet 51
Figure 2-26: Comparison of the specific torque $ST(\beta)$ 52
Figure 2-27: Comparison of the ratio $\tau_{BJ}(\beta)$ 52
Figure 2-28: Comparison of the magnitude of the airgap flux density fundamental $B_m(\beta)$ 53
Figure 2-29: Comparison of magnetic flux density in the yoke $B_{ty}(\beta)$ …….....*53*
Figure 2-30: Comparison of the total axial thickness$h_{tot}(\beta)$..... 54
Figure 2-31: New comparison of magnetic flux density in the yoke $B_{ty}(\beta)$ 55
Figure 2-32: New comparison of the total axial thickness $h_{tot}(\beta)$..... 55

Figure 2-33: New comparison of the specific torque $ST(\beta)$ 55
Figure 2-34: New comparison of electromagnetic torque $Cem\beta$ 56
Figure 2-35: New comparison of magnetic flux density in permanent magnet 56
Figure 2-36: New comparison of the ratio $\tau_{BJ}(\beta)$ 57
Figure 2-37: New stator realization 58
Figure 2-38: STAFPM realized rotor 58
Figure 3-1: Photography of the stator and the rotor 60
Figure 3-2: Three-phase integer winding developed on two pole pairs 60
Figure 3-3: STPMAFM (a) prototype realization, (b) winding distributions 61
Figure 3-4: Definition of θ_R^e in the electrical domain 64
Figure 3-5: The rotor before permanent magnet mounting on the rotor 66
Figure 3-6: A general view of the experimental test bench 69
Figure 3-7: Detailed view around the motor 70
Figure 3-8: Example of the output voltage delivered by the force sensor 71
Figure 3-9: Example of the torque applied on the rotor corresponding to Figure 3-8 71
Figure 3-10: Filtered measured torque 72
Figure 3-11: An offset is applied on the filtered measured torque 72
Figure 3-12: Results of the last treatment along horizontal and vertical axis 73
Figure 3-13: Torque over one period in function of rotor position 73
Figure 3-14: Prototype without permanent magnets on the test bench 74
Figure 3-15: Iron pole facing the R_3 return conductors of the supplied phase (phase 3) 75
Figure 3-16: Case 1 electric domain: aligned rotor axis with the R_3 return conductors .75
Figure 3-17: Magnetic field lines due to the DC supply of phase 3 76
Figure 3-18: Static torque variation around the studied position for $Ic = 2.12\ A$ 76
Figure 3-19: Location of permanent magnet facing the R_3 return conductors of phase 3 77
Figure 3-20: Case 2 electric domain: the rotor axis is aligned with the phase 3 axis 77
Figure 3-21: Case 2 magnetic field lines due to the DC supply of phase 3 78
Figure 3-22: Static torque variation around the case 2 studied position for $Ic = 2.12\ A$ 78
Figure 3-23: Torque in function of rotor angular position θ_R^m 79
Figure 3-24: Saliency torque due to different current values 80
Figure 3-25: Self-inductances variations for different current values 80
Figure 3-26: Derivatives of the self-inductances reconstituted from harmonics 81
Figure 3-27: Static torque without permanent magnet and double phase supply 82
Figure 3-28: Electric domain the rotor axis is aligned with the phase 1 axis 82
Figure 3-29: Static torques for double phase supply for two different values of the current 83
Figure 3-30: $\frac{2C_{R23}(\theta_R^m)}{I_c^2}$ for two different values of current 84
Figure 3-31: The measured cogging torque 86

Figure 3-32: Original and reconstituted cogging torques 86
Figure 3-33: Measured e.m.f at rotational speed $400\ rpm$ 87
Figure 3-34: No-load fluxes derivatives function of rotor position 87
Figure 3-35: No-load fluxes derivatives reconstitution from its harmonics 88
Figure 3-36: Measured and calculated saliency torque for $IC = 2A$ 89
Figure 3-37: Measured and calculated saliency torque for $IC = 4A$ 89
Figure 3-38: Single phase supply: measured and calculated torques for $IC = 0.6A$ 90
Figure 3-39: Single phase supply: measured and calculated torques for $IC = 1.0A$ 91
Figure 3-40: Single phase supply: measured and calculated torques for $IC = 3.6\ A$ 91
Figure 3-41: Double phase supply: measured and calculated torques for $IC = 1.0\ A$ .. 92
Figure 3-42: Double phase supply: measured and calculated torques for $IC = 2.0\ A$ .. 92
Figure 3-43: Three phase supply: measured and calculated torques for $IC = 0.6A$ 93
Figure 3-44: Three phase supply: measured and calculated torque for $IC = 2.6A$ 93
Figure 3-45: No-load flux calculated from their harmonics 94
Figure 3-46: Self and mutual inductances calculated from harmonics and mean values 96
Figure 3-47: DQ0 components of no-load flux calculated 97
Figure 3-48: Definition of the phase shift α *in the electric domain* 98
Figure 3-49: Direct inductance $L_D(\theta_R^m)$ *and quadrature inductance* $L_Q(\theta_R^m)$ *for* $\alpha = 30°$ 99
Figure 3-50: Direct inductance $L_D(\theta_R^m)$ *and quadrature inductance* $L_Q(\theta_R^m)$ *for* $\alpha = 120°$ 99
Figure 3-51: Torque and electromagnetic torque versus α 100
Figure 3-52: $\mathrm{C_R}(\theta_\mathrm{R}^\mathrm{m})$ *for* $\alpha = 87°$ 101
Figure 3-53: $\mathrm{C_R}(\theta_\mathrm{R}^\mathrm{m})$ *for* $\alpha = \alpha_{\mathrm{Opt}} = 93.3°$ 101
Figure 3-54:$C_R(\theta_R^m)$ *for* $\alpha = 100.0°$ 102
Figure 4-1: Full 3D view for the STAFPM geometry 107
Figure 4-2: Different magnetic media of the STAFPM motor on one pole 107
Figure 4-3: Reduced study domain and the parametrization of the geometry 109
Figure 4-4: Example of the linear distribution function of conductor $C_1(r,\theta)$ *at radial position* r 110
Figure 4-5: $\mathrm{C_1(r,\theta)}$ *at three different radius for the SMPMAF for the initial prototype* 111
Figure 4-6: $C_1(r,\theta)$ *viewed as a surface for the STAFPM prototype studied in chapter 3* 111
Figure 4-7: Distribution of $K_D(r,\theta)$ *on the stator bore for the direct reaction field problem* 113
Figure 4-8: Distribution of $K_Q(r,\theta)$ *on the stator bore for the quadrature reaction field problem* 113
Figure 4-9: Lines of the coarsest grid passing over lines of boundaries and interfaces 118
Figure 4-10: Example of grid obtained by increasing the line of the coarsest grid 119

Figure 4-11: Indicial numbering: neighboring of node $P_{i,j,k}$ 120
Figure 4-12: Local numbering: neighboring of node $P_0 = P_{i,j,k}$ 120
Figure 4-13: Flowchart of the 3DFDM4STAFPM software 127
Figure 4-14: 2D view of the grid on a surface inside the airgap 129
Figure 4-15: Distribution of the open circuit magnetic flux density inside the all study domain 130
Figure 4-16: Distribution of the direct armature reaction magnetic flux density inside a surface 131
Figure 4-17: Distribution of the quadrature armature reaction magnetic flux density inside a surface 131
Figure 4-18: Elementary surface on the stator bore 132
Figure 4-19: $B_z(r, \theta, z = h_m + g)$ on the stator for the no-load magnetic flux problem 135
Figure 4-20: Distribution of the direct armature surface current density on the reduced domain 135
Figure 4-21: Distribution of the quadrature armature surface current density on the reduced domain 136
Figure 4-22: Direct armature axial flux density distribution on the reduced domain stator bore 136
Figure 4-23: Quadrature armature axial flux density distribution on the reduced stator bore 137
Figure 4-24: Spanning on pair of poles the direct armature axial flux density distribution 137
Figure 4-25: Spanning on pair of poles the quadrature armature axial flux density distribution 137
Figure 4-26: Flux in function of the rotor position from the no-load magnetic field 138
Figure 4-27: Flux in function of the rotor position from the direct armature reaction magnetic field 138
Figure 4-28: Flux in function of the rotor position from the quadrature armature reaction magnetic field 139
Figure 4-29: DQ components of the no-load flux in function of the rotor position 139
Figure 4-30: DQ components due of the direct armature reaction flux in function of the rotor position 140
Figure 4-31: DQ components of the quadrature armature reaction flux in function of the rotor position 140
Figure 4-32: Torque versus phase shift α 141

List of Tables

TABLE 2-I : Main SMPM parameters 30
TABLE 2-II: Main geometrical parameters of the stator 31
TABLE 2-III:Main geometrical parameters of the rotor 32
TABLE 2-IV:B-H values of the intrinsic recoil curve of Ferrite magnet 32
TABLE 2-V: Mass of the active parts and the theoretical specific torque 39
TABLE 2-VI: Characterization of the no-load magnetic behavior 40
TABLE 2-VII: Characterization of the thermal behavior 40
TABLE 2-VIII: Characterization of the electromagnetic performance 40
TABLE 2-IX: Main parameters for the new prototype 40
TABLE 2-X: SMAFPM geometrical parameters 44
TABLE 2-XI: SMAFPM magnetic quantities 44
TABLE 2-XII: SMAFPM magnetic equations 44
TABLE 2-XIII: STAFPM geometrical parameters 47
TABLE 2-XIV: STAFPM magnetic quantities 48
TABLE 2-XV: STAFPM magnetic equations 48
TABLE 2-XVI.a : Main STAFPM new prototype stator parameters 57
TABLE 2-XVII.b :Main geometrical parameters of the STAFPM new rotor 58
TABLE 3-I: Types of supply and phases connections 70
TABLE 3-II: The first five harmonics of the self-inductances derivatives 81
TABLE 3-III: The first five harmonics of $\frac{2C_{R23}(\theta_R^m)}{I_c^2}$ *for 2.0-3.0 A* 84
TABLE 3-IV: The first five harmonics of $C_d(\theta_R^m)$ 86
TABLE 3-V: The first eleven harmonics of $\frac{d\phi_{vk}}{d\theta_R^m}(\theta_R^m)$ 88
TABLE 3-VI: The first five harmonics of $\phi_{vk}(\theta_R^m)$ 94
TABLE 3-VII: Main electrical parameters for different current values at the unstable equilibrium position 95
TABLE 3-VIII: Main electrical parameters for different rms current values 95
TABLE 3-IX: Comparison of the mean torque from the lumped parameter model and DQ model *102*
TABLE 4-I: Nomenclature *106*
TABLE 4-II: Study domain media limits *114*
TABLE 4-III: Local numbering *120*
TABLE 4-IV: Material properties *128*
TABLE 4-V.a: Radial geometry parameters *128*
TABLE 4-V.b: Azimuthal geometry parameters *128*
TABLE 4-V.c: Axial geometry parameters *128*
TABLE 4-VI: Comparison of the DQ model parameters *140*

General Introduction

This thesis is intended to be a collaboration between LAPLACE and the Lebanese International University in Beirut. For two years it was the case, until the advent of a massive explosion in Beirut in August 2020. From this date the thesis took place only in LAPLACE.
This thesis follows two theses in LAPLACE on Axial Flux Permanent Magnet (AFPM) motors. The first one is on IronLess Axial Flux Permanent Magnet (ILAFPM) motors and the second one on Surface Mounted Axial Flux Permanent Magnet (SMAFPM) motors. The main goal of these two theses is the 3D Magnetic Field model for sizing purpose. This thesis continues the effort of these two theses but it concerns Spoke Type Axial Flux Permanent Magnet (STAFPM) motors.

Neodymium iron boron (NdFeB) constitutes one of the main source of magnetic field in permanent magnet motors. NdFeB magnets are the most common rare earth magnets. Due to rare earth magnets, permanent magnet motors are applied in different industrial sectors and mainly in transport like electric vehicles (EV) or hybrid electric vehicles (HEV). One of the main drawbacks of rare earth magnets is the risk concerning the volatility of their prices. Many researches are undertaken in the world to reduce or eliminate their use in electric motors. One of the types of motor that can eliminate the use of rare earth magnet is STAFPM motor. Indeed, the topology of STAFPM motor concentrates the magnetic flux produced by the permanent magnets in the airgap. The magnetic flux concentration in the airgap allows the use of permanent magnets with low remanent flux density like Ferrite magnets. Additional torque may be achieved by higher saliency ratio which is another interesting characteristic of STAFPM motor.

This thesis does not search new topologies of STAFPM motor. It focuses on 3D magnetic field models to be associated to sizing equations in a design procedure.
Chapter 1 presents the state of the art for the sizing methods of axial flux machines based on magnetic field model. Sizing methods based on analytical magnetic field models for Surface Mounted Radial Flux Permanent Magnet (SMRFPM) motors and their extension to the SMAFPM motors are reviewed. The electromechanical properties of STAFPM motor are not so-well known, thus experimental studies are undertaken in chapter 3. In the second part of chapter 1, the experimental methods for electric motors are reviewed. The last part of the chapter is dedicated to 3D numerical magnetic field model for axial flux motors.
In Chapter 2, by means of unidimensional magnetic field models associated to sizing equations, SMAFPM and STAFPM motors are sized and compared. These two motors have the same stator. An existing SMAFPM motor with Ferrite magnet is reused. Modifications of the stator and the rotor of this motor allow to obtain a STAFPM motor dedicated to the experimental studies in Chapter 3.

In Chapter 3, the experimental studies on the STAFPM prototype are detailed. Two types of measurement are performed: with and without permanent magnets. A general electromechanical lumped parameter model is presented to guide these studies. Original identification methods of the parameters of this model are set up. This general electromechanical model provides quick and detailed static torque simulations. The results of these simulations allow to specify the goals of the 3D numerical magnetic field model.
In Chapter 4, the magnetostatic field problem that governs static operations of STAFPM motors is presented. A focus on the representation of the stator is done. The magnetic scalar potential formulation is detailed: equation in medium, continuity conditions on interfaces and boundary conditions. Strong assumptions are made to reduce the computation times. Two types of magnetic field problems are solved: open-circuit magnetic field problem and armature reaction magnetic field problems. An original method of flux calculation in the framework of 3D finite difference method is presented. This method allows to calculate the main electrical parameters of the STAFPM prototype that can be compared to some parameters deduced from the measurements performed in Chapter 3.

Chapter 1
State of the art

1.1 Introduction

The aim of this work is to propose a sizing model for ‘Spoke Type Axial Flux Permanent Magnet’ (STAFPM) motor. This chapter concerns the state of the art of the sizing of axial flux motors (AFM) based on magnetic field models. Indeed, the use of magnetic field model allows to make accurate evaluations of the electromechanical quantities of interest like the magnetic flux in the phases of the winding and the torque. For slotless surface mounted permanent magnet machine radial flux motor, one uses 2D analytical model of magnetic field. In [1], a magnetic vector potential formulation is used jointly with the method of separation of variables. Two kind of magnetic sources are considered: permanent magnets and the currents in the phase of the stator winding. In the same manner as in [2], the currents are modeled with volume current density in the media. In [3], the analytical model is extended to axial flux machines by using magnetic scalar potential. As the stator is slotted, instead of using the volume current density, the surface current density is used to model armature reaction field.

In this chapter, a state of the art of sizing method of axial flux machines based on magnetic field model is presented first and a specific section is dedicated to the surface current density wave.

It is not easy to extend the 3D hybrid model developed in [3] for ‘Surface Mounted Axial Flux Permanent Magnet’ (SMAFPM) motor to STAFPM motor due to the ferromagnetic poles in the rotor. For SMAFPM motor, such sizing methods based on magnetic field model have been developed in the past years because the behavior of these machines is well-known. To better understand the electromechanical behavior of STAFPM motor, experimental studies are proposed in Chapter 3. In this chapter, a state of the art of experimental studies on synchronous salient pole motors is presented in a second part.

As simple analytical magnetic field models seem to be difficult to set up for STAFPM motor, sizing methods based on numerical magnetic field model is proposed in Chapter 4. 3D finite element methods have been developed a lot to simulate the magnetic field inside electrical machines. These methods are the reference and very well-known to make very accurate simulations but they are very time consuming. In Chapter 4, 3D finite difference method is instead proposed. In the third part of this chapter, a state of the art on 3D finite difference method developed for electrical machines is presented.

1.2 Sizing methods and magnetic field models

The first sizing methods are based exclusively on sizing equations as the one given in [4,5,6] for 'Surface Mounted Radial Flux Permanent Magnet' (SMRFPM) motors and in [7,8,9] for SMAFPM motors.

For surface mounted permanent magnet, the torque is proportional to the airgap magnetic shear stress which can be expressed as [10]:

$$\sigma = B_{rms} K_{rms} \tag{1.1}$$

The three terms in (1.1) constitute the main loads that allow to size by hands surface mounted permanent magnet synchronous motors: B_{rms} is the rms value of the open circuit airgap magnetic flux density wave and K_{rms} is the rms value of the surface current density on the stator bore. Generally, the two waves are in phase and (1.1) is correct. If it is not the case, the expression should be multiplied by the cosine of the phase shift between the two waves [11]. The value of K_{rms} is generally fixed by the cooling system [12,13]. So the quality of the evaluation of the torque depends on the accuracy of the model used to calculate the open circuit airgap magnetic flux density [14].

Most of the time, in a sizing approach, sizing equations are associated to a magnetic field model. Generally, for surface mounted permanent magnet, the magnetic field model is used to evaluate the open circuit airgap magnetic flux density. Except, curiously in [15], where the armature reaction field is evaluated and equivalent current densities on magnets are calculated from permanent magnet geometry and physical parameters.

1.2.1 Quick sizing and simple analytical open circuit field model

To quickly size a motor, designers prefer to use very simple analytical magnetic field model to evaluate the open circuit airgap magnetic field as the one for a SMAFPM motor in [16].

The radial flux and axial flux motors with Ferrite magnets have been sometimes compared as for traction application in [17]. Rarely SMAFPM and STAFPM motors with Ferrite magnets are compared. Most of the time one affirms that STAFPM motors have better performances due to their flux concentration capabilities. In Chapter 2, simple analytical open circuit models associated with classical sizing equations of this kind are used to size SMAFPM and STAFPM motors for comparison purpose. In this comparison the two motors have the same stator.

1.2.2 Analytical open circuit field models

To have better accuracy, analytical models of the magnetic field [1,2] are preferred. Such sizing approaches have been developed for SMRFPM motors [11,13] and extended to SMAFPM motors [3,18].

For slotless SMRFPM motor, the magnetic vector potential formulation is generally used jointly with the volume current density wave to solve magnetic field problems [1,2,15].

The use of the volume current density wave is mandatory in slotless stator due to the thickness of the winding [18].

For slotted motor, to simplify the model, the stator is smoothed by using Carter's coefficient and the armature reaction is modeled by surface current density wave [18]. For slotted SMRFPM motor, in [11], a potential vector formulation is used to solve open circuit field problem and surface current density wave is used to represent the armature reaction.

To size SMAFPM motor, the magnetic field must be modeled in 3D if one wants accurate results. So, it is better to use magnetic scalar potential formulation. Using magnetic scalar potential is natural for magnetic problem with permanent magnets and without volume current density [3,18].

Due to the ferromagnetic poles on its rotor, the 3D analytical model of the open circuit magnetic field developed in [3] and [18] for SMAFPM motor cannot be applied easily to STAFPM motor. To model the open circuit magnetic field of a flux concentrating axial flux machines, an equivalent SMAFPM motor is defined. A mean radius 2D analytical model of this equivalent linear motor is developed in [19]. To calculate the open circuit magnetic field of an axial flux spoke type Vernier machine, an analytical model using the product of the permeance and MMF functions calculated at the mean radius of the airgap is developed in [20] and a 2D FEM model is needed to assess final results. A Magnetic Equivalent Circuit (MEC) has been developed for axial-flux interior permanent magnet machine [21,22]. The aim of this MEC model is to speed up the total magnetic field computation and calculate the torque by a step-by-step method as in numerical simulation by 3D finite element approach.

1.2.3 Numerical magnetic field models for sizing purpose

As 3D analytical models of the open circuit magnetic field of STAFPM motor seem to be difficult to set up, a 3D numerical model is proposed in Chapter 4 for sizing purpose. The model uses magnetic scalar potential formulation associated to 3D finite difference method. To precise the goal of this numerical model, experimental studies on STAFPM motor are undertaken in Chapter 3. The following section is focused on the state of the art on experimental bench dedicated to motors with saliency like STAFPM motors.

1.3 Experimental bench for salient pole machines

STAFPM motors have ferromagnetic poles on their rotor. The poles may contribute to very high torque ripples and saliency torque. Generally, one wants to reduce torque ripples and to use the saliency effect to obtain additional torque.

To control the saliency effect, the self and mutual inductances in function of the rotor position must be known. The computation by finite element analysis (FEA) or by measurement technics of these inductances are based on the general electric model of electrical machines which may be called by 'Coupled Circuit Model' [23]:

$$\boldsymbol{V} = \boldsymbol{RI} + \frac{d}{dt}\boldsymbol{\Phi} = \boldsymbol{RI} + \frac{d}{dt}\left(\boldsymbol{\Phi_v}(\theta_R^m) + \boldsymbol{L}(\theta_R^m)\boldsymbol{I}\right) \tag{1.2}$$

The no-load flux and the inductances in function of the mechanical rotor position θ_R^m are the parameters of the model that must be identified by FEA or measurements. The inductances are measured at different rotor positions by blocking the rotor at each position. The inductances are obtained from the method of flux linkage measurement which have been developed for switch reluctance (SR) motor [24,25]. At a locked position of the rotor θ_R^m, if phase 1 is supplied by a DC voltage U, the current reaches its steady state value I in t_I seconds and the flux, according to (1.2), is given by:

$$\Phi_1(\theta_R^m, I) = \Phi_0 + \int_0^{t_I} \big(U - Ri(t)\big)\, dt = \Phi_0 + L_1(\theta_R^m) I \tag{1.3}$$

If there are no permanent magnets, the constant Φ_0 is null. AC voltage may also be used. In both methods, DC or AC, eddy current or hysteresis phenomena may induce errors in the final flux values [26]. In [27], the harmonics of the measured self and mutual inductances in function of the rotor position are evaluated. These harmonics are used to evaluate the parameters of an extended DQ model specific to motors with non-sinusoidal waveforms. At the final step, these parameters are applied to elaborate control method for these motors.

Self and mutual inductances in function of the rotor are most of the times computed by FEA. In case of saturation, the frozen permeability method may be used [28]. To calculate the torque due to saliency during dynamical simulations, the derivatives of these inductances have to be known. The direct numerical derivatives of these inductances with respect to the rotor position may induce noises and errors. In the framework of finite element analysis to avoid these noises and errors, the inductances derivatives may be identified via the computation of torques by means of the Maxwell Stress Tensor [29]. The phases are supplied by DC currents while the rotor is moving at constant speed. Different DC current supplies are performed: single phase supply or double phase supply [30]. This approach is mainly based on the general electromechanical lumped parameter model for which the torque of a permanent magnet motor is the sum of the cogging torque $C_d(\theta_R^m)$, the saliency torque which is the second term of (1.4) and the electromagnetic torque, the last term [31]:

$$C_{mot}(\theta_R^m) = C_d(\theta_R^m) + \frac{1}{2}\boldsymbol{I}(\theta_R^m)^T \frac{d\boldsymbol{L}(\theta_R^m)}{d\theta_R^m}\boldsymbol{I}(\theta_R^m) + \boldsymbol{I}(\theta_R^m)^T \frac{d\boldsymbol{\Phi_v}(\theta_R^m)}{d\theta_R^m} \tag{1.4}$$

Indeed, in self-driven synchronous motor, the currents $\boldsymbol{I}(\theta_R^m)$ are function of the rotor position.

Instead of using FEA, the method proposed by [29] and [30] may be transposed to measurement techniques. For SR motor, at a locked position of the rotor θ_R^m, if the phase 1 is supplied by a DC voltage U, the current reaches its steady state value I, according to (1.4) the measured torque is $C_1(\theta_R^m, I)$ and the derivative of the self-inductance is:

$$\frac{\partial L_1(\theta_R^m, I)}{\partial \theta_R^m} = 2\frac{C_1(\theta_R^m, I)}{I^2} \tag{1.5}$$

For that, one must have a test bench that allows accurate torque measurements in function of the rotor position. Torque measurement is not easy at all due mainly to mechanical problems such as resonance frequencies. Static torque measurements by means of force sensors located on the stator are proposed to measure torque ripples of SMRFPM motor

[32,33]. These sensors measure reaction torque. Song et al have identify the flux linkage characteristics of a SR motor and validated these identifications by measuring static torque characteristics [34]. In Chapter 3, the derivatives of the self and mutual inductances of the STAFPM motor are identified from static torque measurements on a LAPLACE's test bench. Other static electromagnetic characteristics of this motor are also measured. These static characteristics allow to simulate the electromechanical behavior of the motor. The specifications of the 3D numerical magnetic field model that can be associated to sizing equations are defined at the end of Chapter 3.

1.4 3D numerical magnetic model for sizing purpose

For SMAFPM motors, an analytical magnetic field model associated to sizing equations has been developed [18]. For STAFPM motors, two types of magnetic field problems must be solved:

- Open circuit magnetic field problem to take into account the airgap flux concentration,
- Armature reaction field problem to take into account saliency effects.

To solve open circuit magnetic field problems in SMAFPM motors, a 3D finite difference method using magnetic scalar potential formulation has been developed [16]. The 3D code has not been exploited at all by the author. For SMAFPM motor, the author prefers to use a 2D finite difference mean radius model which is available in the software DIFIMEDI [35]. Even in SMAFPM motors, the no-load airgap magnetic flux density may depends on the radial position [36].

For STAFPM motors, 3D Finite Element magnetic field model can be used for sizing purposes, but most of 3D FEA need a lot of time to compute the magnetic field inside such motor. To speed up the solving of the open circuit and armature reaction magnetic field problems, assumptions must be made. As for SMAFPM motors, the stator is represented only by a boundary condition on the stator bore surface. In open circuit problem, as in [18], the magnetic flux density is normal to this surface. In armature reaction field problem, the armature reaction field is modeled by surface current density waves [18].

1.4.1 3D finite difference method

Finite difference method is based on numerical differentiations that transform partial derivative equation (PDE) in finite difference equation (FDE) [37,38]. To solve Laplacian's or Poisson's equation, one may use high order finite difference approximation scheme [39]. Second order finite difference approximation may be sufficient to solve Poisson's equation in cylindrical coordinates [40]. Using magnetic scalar potential formulation, the magnetic field problems to be solved for STAFPM motors can be reduced to Laplacian's or Poisson's equation. A second order finite difference approximation scheme on irregular grid is chosen for both types of problem.

For a scalar function at a point P of coordinates (x, y, z), its value is given by $f(x, y, z)$. At a particular point P_0 of coordinates (x_0, y_0, z_0) its value is:

$$f_0 = f(x_0, y_0, z_0) \tag{1.6}$$

The first and second order partial derivatives of f with respect to x at point P_0 are noted:

$$\begin{cases} \left(\frac{\partial f}{\partial x}\right)_0 = \frac{\partial f}{\partial x}(x_0, y_0, z_0) \\ \left(\frac{\partial^2 f}{\partial x^2}\right)_0 = \frac{\partial^2 f}{\partial x^2}(x_0, y_0, z_0) \end{cases} \tag{1.7}$$

In the neighborhood of point P_0 the values of the function can be evaluated with a second order approximation using Taylor's development at order two:

$$\begin{cases} f_1 = f(x_0 + h_1, y_0, z_0) = f_0 + h_1 \left(\frac{\partial f}{\partial x}\right)_0 + \frac{h_1^2}{2}\left(\frac{\partial^2 f}{\partial x^2}\right)_0 + o(h_1^2) \\ f_3 = f(x_0 - h_3, y_0, z_0) = f_0 - h_3 \left(\frac{\partial f}{\partial x}\right)_0 + \frac{h_3^2}{2}\left(\frac{\partial^2 f}{\partial x^2}\right)_0 + o(h_3^2) \end{cases} \tag{1.8}$$

Inversely, knowing the values of the function at a point P_0 and at its neighborhood allows to approximate the partial derivatives [3,54]:

$$\begin{cases} \left(\frac{\partial f}{\partial x}\right)_0 \approx \frac{h_1 - h_3}{h_1 h_3} f_0 + \frac{h_3}{h_1(h_1+h_3)} f_1 - \frac{h_1}{h_3(h_1+h_3)} f_3 \\ \left(\frac{\partial^2 f}{\partial x^2}\right)_0 \approx -\frac{2}{h_1 h_3} f_0 + \frac{2}{h_1(h_1+h_3)} f_1 + \frac{2}{h_3(h_1+h_3)} f_3 \end{cases} \tag{1.9}$$

These expressions are used in Chapter 4 to transform Laplace's equation of the magnetic scalar potential into a system of finite difference equations.

1.4.2 Specific boundary conditions

For the open circuit magnetic field problem, the boundary conditions are the classical tangential magnetic field or normal magnetic flux density.

For armature reaction magnetic field problem, there is a specific boundary condition on the surface of the stator bore. The tangential component of the magnetic field intensity is equal to the surface current density [18]. The boundary condition on the surface of the stator bore is given by:

$$\vec{H} \wedge \overrightarrow{e_z} = \vec{K} = K(r, \theta, t)\overrightarrow{e_r} \tag{1.10}$$

The surface current density wave is the sum, over all phases of the stator winding, of the product of the linear distribution function of the conductors $C_k(\theta)$ of phase k and the current $I_k(t)$ feeding this phase [11,13].

1.4.3 Distribution function of conductors

A surface distribution function of conductors $C_k(\theta)$ of phase k has been defined for slotless radial flux machine in [2,41] which lead to volume current density wave $j(\theta, t)$:

$$j(\theta, t) = \sum_{k=1}^{q} C_k(\theta)\, I_k(t) \tag{1.11}$$

The distribution function of conductors $C_k(\theta)$ can be decomposed in Fourier series which components are calculated from the winding characteristics [1]. Some authors prefer to use the term "winding functions" from which are obtained the magneto motive force wave of each phase around the stator and the distribution functions of conductors are the "winding function derivatives" [42]. Winding theory is classically based on "winding functions" [42]. An attempt

to use the "distribution functions of conductors" as basics of winding theory is done in [11] and [13]. Indeed, the winding coefficients may be calculated from the harmonics of the distribution functions of conductors [11].

For radial flux motor with slotted stator, the linear distribution function of conductors $C_k(\theta)$ of phase k depends only on the azimuthal position θ and the surface current density wave $K(\theta, t)$ is given by [11]:

$$K(\theta, t) = \sum_{k=1}^{q} C_k(\theta)\, I_k(t) \tag{1.12.a}$$

For axial flux motor, the dependency with the radial position must be taken into account [3]:

$$K(r, \theta, t) = \sum_{k=1}^{q} C_k(r, \theta)\, I_k(t) \tag{1.12.b}$$

1.4.4 Electric parameters calculation

Once the magnetic field in the study domain is obtained by 3D finite difference method, the parameters of the electric model must be calculated.

1.4.4.1 Magnetic energy method

The inductances may be identified from the calculation of the magnetic energy. The use of magnetic potential vector $\vec{A}$ may speed up the calculation of energy because, in this case, the integration is done only over the winding region V_{wind} and not over all the study domain. Using the volume current density $\vec{J}$, the energy is given by the integral [43]:

$$W = \iiint_{V_{wind}} \vec{A}\vec{J}\, dV \tag{1.13}$$

When the magnetic circuit is not saturated, the energy of SR motor can be also expressed as:

$$W(\theta_R^m) = \frac{1}{2}\boldsymbol{I}(\theta_R^m)^T \boldsymbol{L}(\theta_R^m)\boldsymbol{I}(\theta_R^m) \tag{1.14}$$

If only the phase 1 is supplied by a current I, its inductance at the rotor position θ_R^m is identified as:

$$L_1(\theta_R^m) = 2\frac{W(\theta_R^m)}{I^2} \tag{1.15}$$

In a sizing procedure, this method can be hardly used for axial flux machine because it may be very time consuming.

1.4.4.2 Magnetic flux method

For radial flux motor, a 2D model can be used with the magnetic vector potential formulation:

$$\vec{A} = A_z(r, \theta, t)\overrightarrow{e_z} \tag{1.16}$$

Considering the invariance by translation along an axial line parallel to $\overrightarrow{e_z}$, the radial component of the magnetic flux density is:

$$B_r(r, \theta, t) = \frac{1}{r}\frac{\partial A_z(r,\theta,t)}{\partial \theta} \tag{1.17}$$

A surface $S(\theta)$ is defined on the stator bore of radial position r_0 with an axial length L and with an angular width $\frac{\pi}{p}$ situated between two angular positions, $\theta - \frac{\pi}{p}$ and θ, on the stator bore. The magnetic flux, $\varphi(\theta, t)$, crossing this surface is given by:

$$\varphi(\theta,t) = \iint_{S(\theta)} \vec{B}.\overrightarrow{dS} = L\, r_0 \int_{\theta-\frac{\pi}{p}}^{\theta} B_r(r_0,\theta,t)d\theta \tag{1.18}$$

According to (1.17), the last integral is put in the form:

$$\int_{\theta-\frac{\pi}{p}}^{\theta} B_r(r_0,\theta,t)d\theta = \frac{1}{r_0}\int_{\theta-\frac{\pi}{p}}^{\theta} \frac{\partial A_z(r_0,\theta,t)}{\partial\theta} d\theta = \frac{1}{r_0}\left(A_z(r_0,\theta,t) - A_z\left(r_0,\theta-\frac{\pi}{p},t\right)\right) \tag{1.19}$$

The flux crossing $S(\theta)$ is [1]:

$$\varphi(\theta,t) = L\left(A_z(r_0,\theta,t) - A_z\left(r_0,\theta-\frac{\pi}{p},t\right)\right) \tag{1.20}$$

All the conductors of a phase k are located inside a surface S_k of the study domain. The flux per unit length in the phase k is easily calculated by means of the distribution function of conductors $C_k(\theta)$ [1,2,41]:

$$\Phi_k(t) = \iint_{S_k} A_z(r,\theta,t)C_k(\theta)rdrd\theta \tag{1.21}$$

This expression of flux can be adapted to axial flux machine. If we consider, fictively, for a while, that the one component magnetic potential vector formulation can be used for axial flux machine, the magnetic potential vector would have been [44]:

$$\vec{A} = A_r(\theta,z,t)\overrightarrow{e_r} \tag{1.22}$$

Considering the supposed invariance by translation along a radial line parallel to $\overrightarrow{e_r}$, the 2D problem would have been solved at a given radius r_m [36,44]. The axial component of the magnetic flux density would have been:

$$B_z(\theta,z,t) = \frac{1}{r_m}\frac{\partial A_r(\theta,z,t)}{\partial\theta} \tag{1.23}$$

A surface $S(\theta)$ is defined on the stator bore of axial position z_0 with a radial length δr and with an angular width $\frac{\pi}{p}$ situated between two angular positions, $\theta-\frac{\pi}{p}$ and θ, on the stator bore. The magnetic flux, $\varphi(\theta,t)$, crossing this surface would have been given by:

$$\varphi(\theta,t) = \iint_{S(\theta)} \vec{B}.\overrightarrow{dS} = \delta r\, r_m \int_{\theta-\frac{\pi}{p}}^{\theta} B_z(\theta,z_0,t)d\theta \tag{1.24}$$

According to (1.23), the last integral could have been put in the form:

$$\int_{\theta-\frac{\pi}{p}}^{\theta} B_z(\theta,z_0,t)d\theta = \frac{1}{r_m}\int_{\theta-\frac{\pi}{p}}^{\theta} \frac{\partial A_r(\theta,z_0,t)}{\partial\theta} d\theta = \frac{1}{r_m}\left(A_r(\theta,z_0,t) - A_r\left(\theta-\frac{\pi}{p},z_0,t\right)\right) \tag{1.25}$$

The flux crossing $S(\theta)$ would have been:

$$\varphi(\theta,t) = \delta r\left(A_r(\theta,z_0,t) - A_r\left(\theta-\frac{\pi}{p},z_0,t\right)\right) \tag{1.26}$$

To model axial flux machine in 3D, in chapter 4, a magnetic scalar potential is used. The similarity of the flux expressions (1.20) and (1.26) suggests that expression (1.24) may be useful. Instead of having finite length δr, the elemental surface $S(\theta)$ should have an infinitesimal length dr and the expression (1.24) would define a flux derivative with respect to radial position:

$$\frac{d\varphi}{dr}(r,\theta,z_0,t) = r\int_{\theta-\frac{\pi}{p}}^{\theta} B_z(r,\theta,z_0,t)d\theta \tag{1.27}$$

In chapter 4, with the help of this expression, an original model of the magnetic flux in the phases of the stator winding is developed in the framework of the 3D Finite Difference Method combined with the magnetic scalar potential formulation.

1.5 Conclusion

This chapter sets the main contexts in which this work intends to contribute.

The first main context is the development of magnetic field model associated to sizing equations. In chapter 2, quick sizing associated to simple analytical model of the open circuit field are used to compare SMAFPM and STAFPM motors having the same stator.

For surface mounted permanent magnet motor, the sizing equations could have been associated to analytical magnetic field model because they are very well known. For STAFPM motor, the ferromagnetic poles in the rotor do not facilitate the setting up of 3D analytical magnetic field models that can be easily associated to sizing equations. Instead a 3D numerical magnetic field model is proposed.

To know the goals of this numerical field model, experimental studies are undertaken in chapter 3 to better know the electromechanical behavior of STAFPM motor. The second main context is the experimental identification of the parameters of the general electromechanical model of an electric motor from static torque measurements. The identification of these parameters in chapter 3 allows to make quick and detailed simulations of a STAFPM motor specially sized for these experimental studies. The obtained results allow to specify the goals of the numerical magnetic field model.

The last main context in which this work contributes is the flux calculation in the framework of 3D finite difference method associated to magnetic scalar potential formulation.

Chapter 2

Spoke Type Permanent Magnet Axial Flux Motor Prototype Sizing

2.1 Introduction

The sizing procedure of surface mounted permanent synchronous motor (SMPMSM) is well established. The loadability properties of non-salient synchronous motor are very well known [12]. From these properties, an accurate analytical sizing model has been developed for radial flux surface mounted permanent magnet synchronous motor [10,13]. This analytical sizing model has been extended to surface mounted permanent magnet axial flux machines [3,18].

The extension of this type of analytical model to salient permanent magnet motors is difficult. It is in part due to the fact that the loadability concepts established so far do not take specifically into account the effects of saliency because these motors are not so well-known as SMPMSM. In order to better know this kind of motor, experimental studies on a spoke-type motor are undertaken in chapter 3. The main goal of this chapter is to size the spoke type axial flux permanent magnet (STAFPM) prototype for these experimental studies.

The fabrication of laminated ferromagnetic material for the stator is extremely difficult for axial flux machines [45]. In order to avoid this difficulty, an existing axial flux motor in the LAPLACE laboratory is reused. The great advantage of this motor is that the ferromagnetic part of the stator is already laminated [16].This motor is a single rotor-single stator axial flux topology with theoretically surface mounted and axially polarized ferrite permanent magnets.

One of the main properties of spoke-type motor is the no-load magnetic flux concentration in the airgap. Thus, the stator and rotor of the existing motor must be modified to fulfill this important property. In order to make the best use of the stator, thermal and magnetic loads of the existing motor are theoretically evaluated first. The results of this theoretical evaluation are the basis for sizing the new STAFPM prototype.

The no-load magnetic flux concentration in the airgap is better fulfill by a high number of poles. Thus the number of poles is increased. The fabrication of a rotor containing ferromagnetic poles, Ferrite permanent magnets and no ferromagnetic yoke is not common at all and may be difficult for an academic laboratory. To reduce this difficulty, the axial airgap length is increased. This increase of the airgap allows reducing the axial attractive force that may applied on ferromagnetic pole or magnets.

To show the benefits of concentrating magnetic flux in the airgap, a comparative sizing of surface mounted axial flux permanent magnet (SMAFPM) motor and STAFPM motor is proposed with the same conditions: same number of poles and airgap. This comparative sizing is done after the evaluation of thermal and magnetic loads of the existing motor. The results of this evaluation are used to make the specifications of the two motors. Their specific torque is one of the criteria to compare the two motors.

After the comparison of the performances of these two motors, the choice of the prototype for experimental study is done.

2.2 General description of the existing axial flux motor

The existing axial flux motor is a three-phase motor with four pole pairs (*Figure 2-1* and *Figure 2-4*). The stator has two slots per pole and per phase.

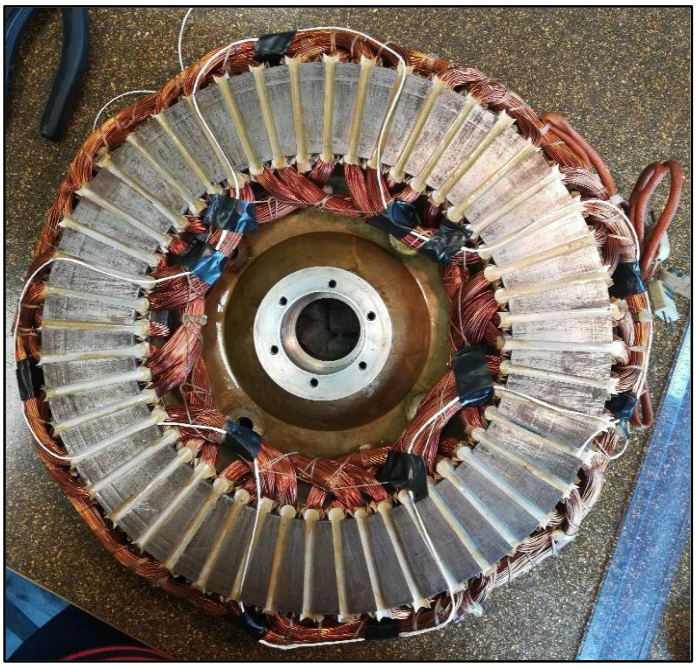

Figure 2-1: A photography of the stator of the existing SMAFPM

In each slot there are 95 conductors and in each phase all conductors are in series [16]. The number of slots n_e and the number of turns per phase n_s are deduced from the expression *(2-1):*

$$\begin{cases} n_e = 2pqn_{epp} \\ n_s = \dfrac{n_e n_c}{2q} = pn_{epp}n_c \end{cases} \qquad (2\text{-}1)$$

The main parameters are reported in *TABLE 2-I.*

TABLE 2-I : Main SMAFPM motor parameters

Number of phases, q	3
Number of pairs of poles, p	4
Number of slots per pole and per phase, n_{epp}	2
Number of conductors per slot, n_c	95
Number of slots, n_e	48
Number of turns, n_s	760
Copper filling factor, k_{fill}	0.3
Air gap thickness, $e_g(mm)$	1.0

2.2.1 Stator

The ferromagnetic material of stator is made of non-oriented grain electrical steel and approximated by the alloy *Iron-Silicium* (FeSi) “M235-35A” with 0.35 mm sheet thickness [46]. *Figure 2-2* presents its *B(H)* curve.

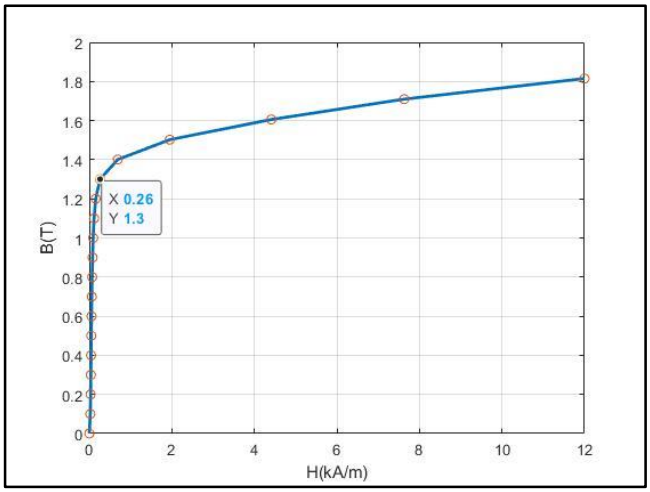

Figure 2-2: B(H) curve of the electrical steel M235-35A

The slots are rectangular which means that their azimuthal width is independent of the radial position r. The main geometrical parameters are summarized in *TABLE 2-II*.

TABLE 2-II: Main geometrical parameters of the stator

Internal radius, $R_1(mm)$	100.0
External radius, $R_2(mm)$	150.0
Slot axial height, $h_e(mm)$	12.5
Slot azimuthal width, $w_e(mm)$	8.0
Azimuthal width of slot opening, $o_e(mm)$	4.8
Axial height of slot opening, $h_o(mm)$	1.0
Stator yoke axial thickness, $h_{cs}(mm)$	8.0
Conductor diameter, $d_c(mm)$	0.63

Indeed, *Figure 2-3* shows some geometrical parameters of this stator.

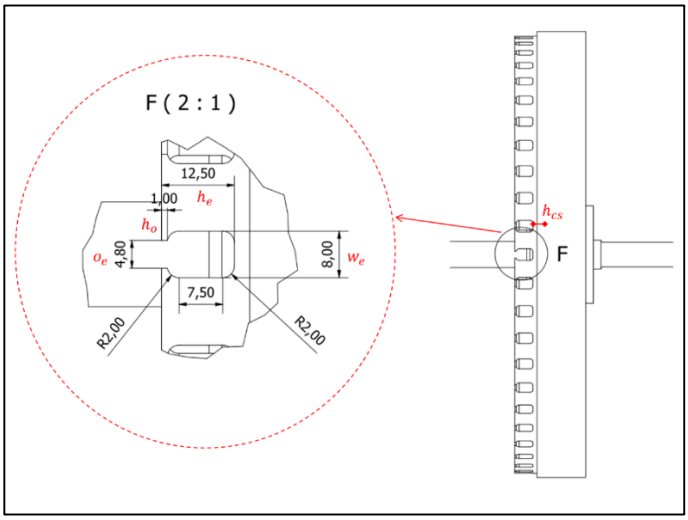

Figure 2-3:Slot geometric parameters

2.2.2 Rotor

Figure 2-4 shows a photography of the rotor of the existing SMAFPM motor. The parallelepiped Ferrite permanent magnets are axially polarized and buried between ferromagnetic parts. The measured geometrical parameters are summarized in *TABLE 2-III*. Furthermore, *Table 2-IV* gives the values of B and H on the intrinsic recoil curve.

TABLE 2-III:Main geometrical parameters of the rotor

Number of pairs of pole, p	4
PM internal radius, R_{int}	91.50 mm
PM external radius, R_{ext}	160.0 mm
Axial thickness of the rotor yoke, h_{cr}	8.0 mm
PM axial thickness, h_m	5.0 mm
PM azimuthal width at the mean radius, L_m	65.45 mm
PM radial length, l_a	50.0 mm

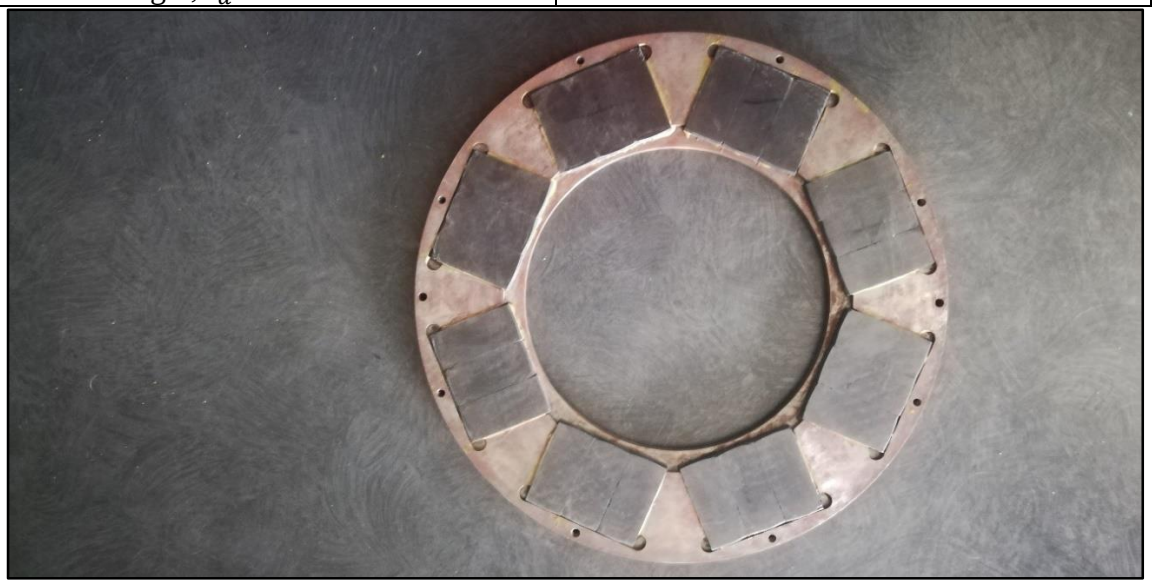

Figure 2-4: A photography of the existing SMAFPM rotor

Figure 2-5 shows the intrinsic recoil curve of the magnets mounted on the rotor surface:

$$B(H) = J + \mu_0 \mu_{ra} H \qquad (2\text{-}2)$$

TABLE 2-IV:B-H values of the intrinsic recoil curve of Ferrite magnet

$B(T)$	$H(kA.m^{-1})$	μ_{ra}
0.37	0.0	
0.305	-50	1.03
0.30	-55	1.01
0.245	-100	1.0
0.2	-135	1.0
0.18	-150	1.0
0.15	-175	1.0
0.12	-200	1.0
0.1	-215	1.0

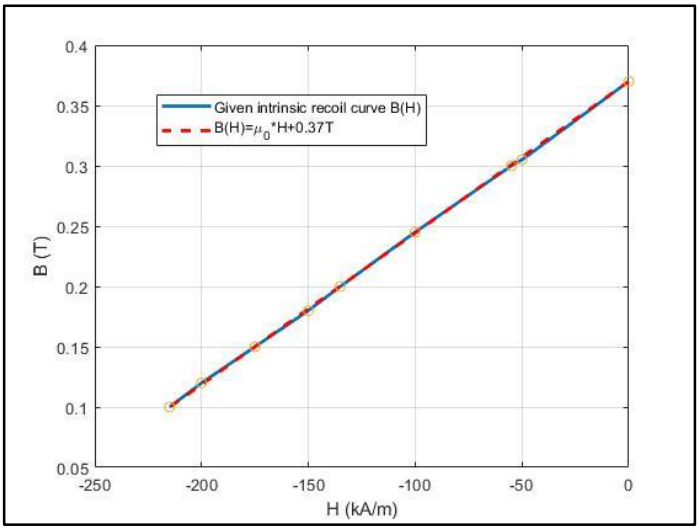

Figure 2-5: Intrinsic recoil curve $B(H)$ of Ferrite magnet

The axial polarization J, relative magnetic permeability μ_{ra} and the optimal magnetic flux density B_{opt} where the BH product is maximal are shown in *(2-3)*.

$$\begin{cases} J = 0.37\ T \\ \mu_{ra} = 1.0 \\ B_{opt} = \dfrac{J}{2} = 0.185\ T \end{cases} \qquad (2\text{-}3)$$

The ferromagnetic material of the rotor is the electrical steel *XC12*. *Figure 2-6* presents its *B(H)* curve.

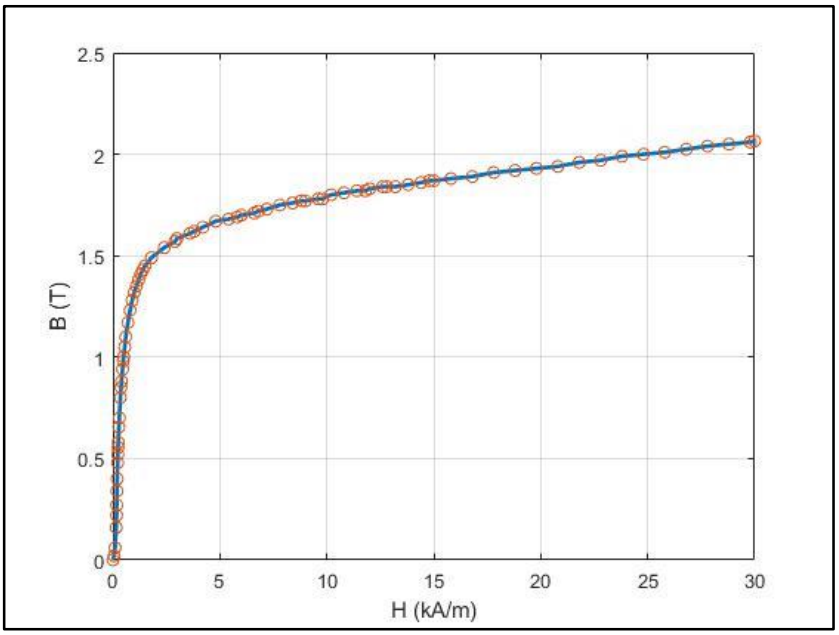

Figure 2-6: B(H) curve of the electrical steel XC12

2.3 Evaluation of the magnetic loads of the existing motor

The no-load magnetic flux densities in the airgap, in the yokes and teeth of the existing motor are theoretically evaluated in this section. This evaluation is done according to the sizing approach developed in [10][13] based on loadability concepts. To guarantee the best use of the stator in a magnetic point of view, these values of magnetic loads chosen in [16] are kept and used to size the new STPMAFM prototype.

2.3.1 No-load magnetic flux density in the airgap

To calculate the no-load magnetic flux density, the motor is assimilated to a linear motor developed at the mean radius:

$$R_m = \frac{R_1 + R_2}{2} = 125.0\ mm \qquad (2\text{-}4)$$

The permanent magnets which are parallelepipeds are approximated by sectorial magnets whose arc pole coefficient β is equal to [16]:

$$\beta = \frac{2}{3}$$

They are axially polarized and supposed to be surface mounted and not buried. The following assumptions are made:

- The magnetic fields in the magnet and airgap are axial;
- The magnetic field does not depend on the radial position r (1D mean radius model);
- Iron permeability is infinite;
- The slot effects on the magnetic field are neglected.

The geometrical parameters are given in *TABLE 2-II* and *TABLE 2-III*. The study domain at the mean radius R_m with smoothed stator is presented on *Figure 2-7*. The azimuthal length of one pole at the mean radius is L_p and L_m is the azimuthal length of one magnet. Due to the assumptions, only the magnetic field in the permanent magnets and the air gap are involved and the material properties of these media are given by the following equations:

$$\begin{cases} \overrightarrow{B_a} = \mu_a \overrightarrow{H_a} + \vec{J} \\ \overrightarrow{B_g} = \mu_0 \overrightarrow{H_g} \end{cases} \qquad (2\text{-}5)$$

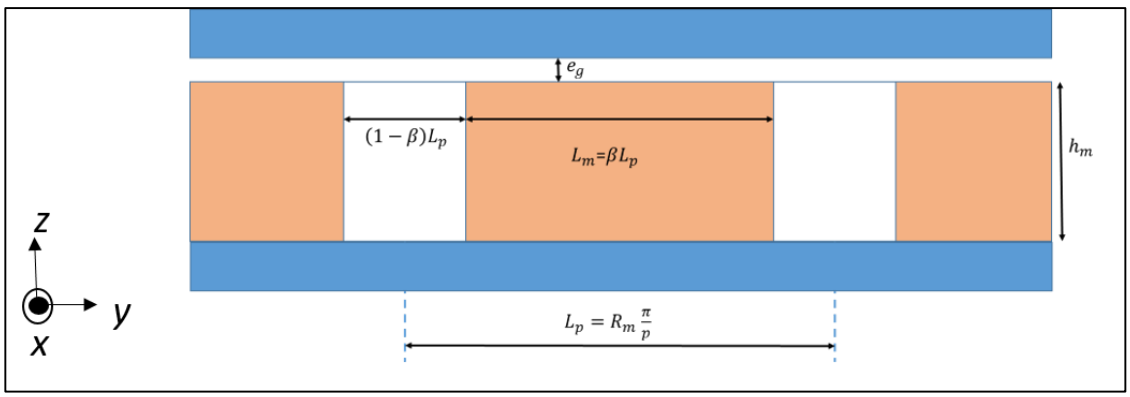

Figure 2-7: Study domain for the evaluation of the air gap flux density

The Ampere's law is applied on the closed path shown in *Figure 2-8.*

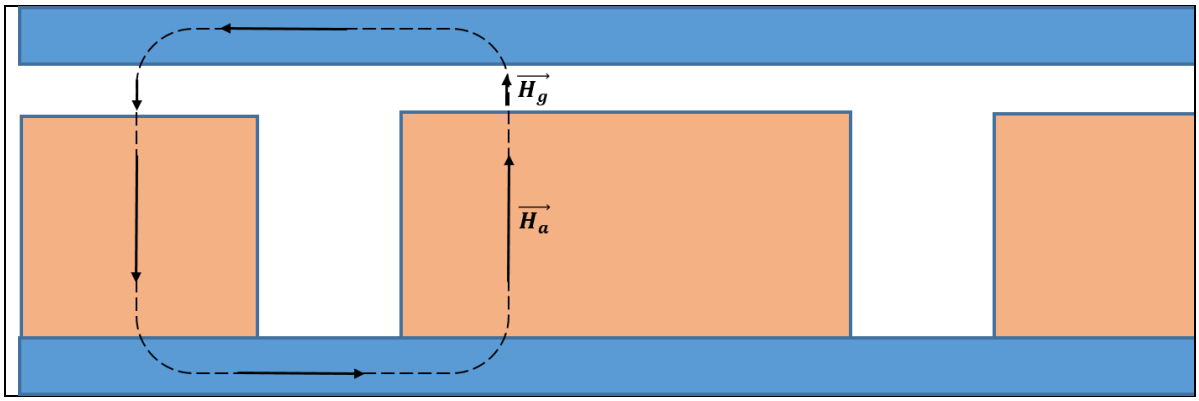

Figure 2-8: Closed path to apply Ampere's law

The axial magnetic field intensities in the permanent magnet (H_{za}) and in the air gap (H_{zg}) are linked by the following equation *(2-6)*.

$$H_{za}h_m + H_{zg}e_g = 0 \qquad (2\text{-}6)$$

Magnetic flux conservation law is applied using surfaces S_g and S_m on *Figure 2-9.*

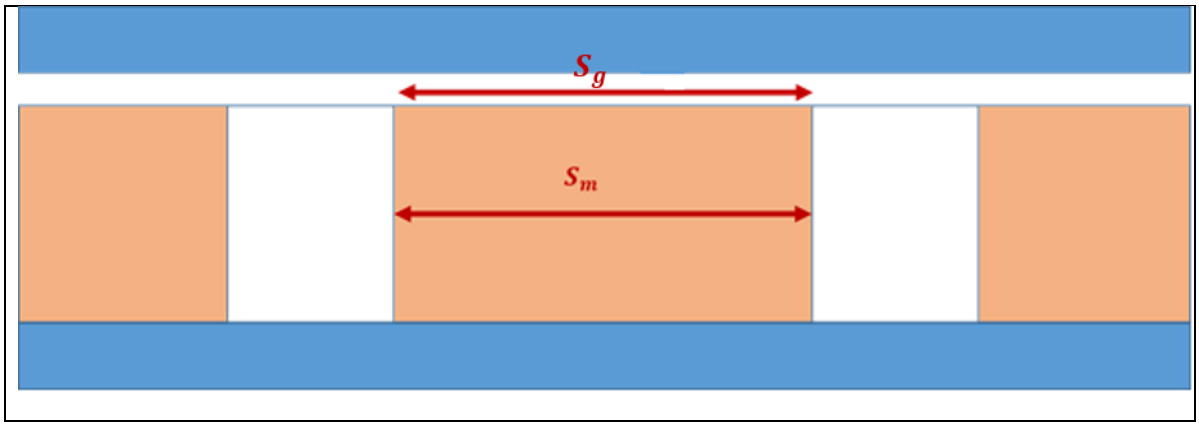

Figure 2-9: Flux conservation law applied on airgap and magnet surfaces S_g and S_m

As the two surfaces are equal and due to the assumptions, the axial magnetic flux densities in the airgap (B_{zg}) and the magnet (B_{za}) are equal too. Equations *(2-5)* and *(2-6)* lead to the expression of the axial flux density written in *(2-7)*.

$$B_{zg} = B_{za} = \frac{Jh_m}{h_m + \mu_{ra}e_g} = 0.31\ T \qquad (2\text{-}7)$$

The magnetic flux density in the magnet is thus higher than the optimal magnetic flux density in the magnet *(2-3)*. According to the assumptions, the airgap magnetic flux density has a rectangular waveform. For surface mounted permanent magnet machine with sinusoidal current waveforms, the main magnetic load is the magnitude of the fundamental of airgap magnetic flux density. Its value, for a rectangular wave form, is given by the following expression:

$$B_m = \frac{4B_{zg}sin\left(\beta\frac{\pi}{2}\right)}{\pi} = 0.34\ T \qquad (2\text{-}8)$$

Therefore, it's 'rms' value is:

$$B_{rms} = \frac{B_m}{\sqrt{2}} = 0.24\ T \tag{2-9}$$

2.3.2 No-load magnetic flux density in the stator iron

As the SMAFPM existing motor has six teeth per pole, according to the assumptions, the magnetic flux on one pole has the pattern shown on *Figure 2-10*. From *Figure 2-9* and *Figure 2-10*, the no-load airgap flux per pole φ_p is given by:

$$\varphi_p = B_{zg} S_g \tag{2-10}$$

According to *Figure 2-10*, the magnetic flux conservation law gives the expression of the azimuthal magnetic flux density B_{tys} in the stator yoke and B_{tyr} in the rotor yoke and its numerical value:

$$B_{tys} = B_{tyr} = \frac{L_m B_{zg}}{2h_{cs}} = 1.26\ T \tag{2-11}$$

At the mean radius, the tooth pitch and the width of a tooth are expressed in *(2-12)*.

$$\begin{cases} p_d = \dfrac{2\pi R_m}{n_e} = 16.36\ m \\ w_d = p_d - w_e = 8.36\ mm \end{cases} \tag{2-12}$$

The no-load axial magnetic flux density in teeth are thus given by*(2-13)*.

$$B_{zd} = \frac{L_m B_{zg}}{4w_d} = 0.6\ T \tag{2-13}$$

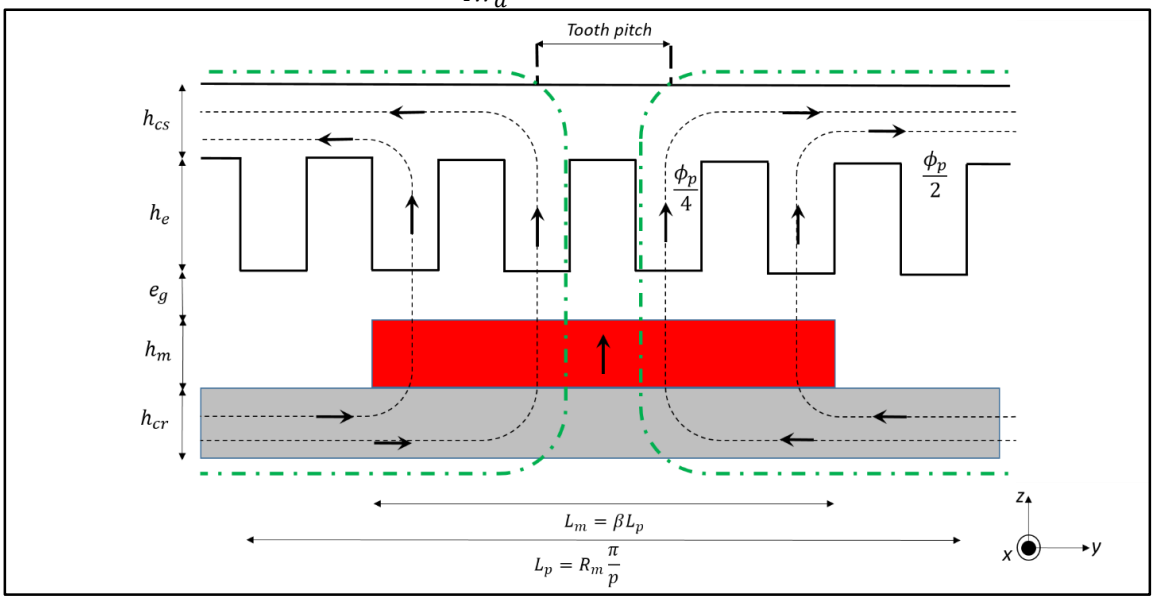

Figure 2-10: Magnetic flux pattern on one pole of the existing motor

These estimated values of the no-load magnetic flux density in yokes and teeth are compatible with the $B(H)$ curves of the ferromagnetic media in the stator and the rotor (*Figure 2-2* and *Figure 2-6*). These values guarantee that even with a strong armature reaction the values of magnetic flux density in the ferromagnetic media will stay in the linear zone of $B(H)$ curves.

2.4 Characterization of the armature reaction

The armature reaction is characterized by the thermal loads which are the 'rms' values of the current density j_{rms} in the conductors of the stator and the linear current density A_{rms} around the stator bore. These two values have a great effect on thermal behavior of the motor because their product are proportional to the Joule loss in the stator winding [2]-[5].

The armature reaction is also characterized by the 'rms' value of the surface current density waveform K_{rms} around the stator bore. It is worth recalling that the electromagnetic torque is proportional to the shear stress σ [12]:

$$\sigma = B_{rms}K_{rms} \tag{2-14}$$

2.4.1 Thermal loads

The 'rms' value of the current density chosen in [16] is:

$$j_{rms} = 5.0\ A.mm^{-2} \tag{2-15}$$

Knowing the filling factor (*TABLE 2-I*) and the sizes (*TABLE 2-II*) of each slot leads to the slot Ampere Turns:

$$AT_e = k_{fill}S_e j_{rms} \tag{2-16}$$

The 'rms' value of the rated current is then:

$$I_{rms} = \frac{AT_e}{n_c} = 1.5\ A \tag{2-17}$$

The expression of the linear current density at the mean radius is:

$$A_{rms} = \frac{n_e AT_e}{2\pi R_m} \tag{2-18}$$

The thermal behavior of the motor is characterized by the thermal loads which are the current density, the linear current density and their product [12]:

$$\begin{cases} j_{rms} = 5.0\ A.mm^{-2} \\ A_{rms} = 8727\ A.m^{-1} \\ A_{rms}j_{rms} = 4.36\ 10^{10} A^2.m^{-3} \end{cases} \tag{2-19}$$

These values correspond to the thermal behavior of an electric motor cooled by natural convection.

2.4.2 Surface current density

The distribution of conductors of the phase 1 along the stator bore at the mean radius is shown on *Figure 2-11*.

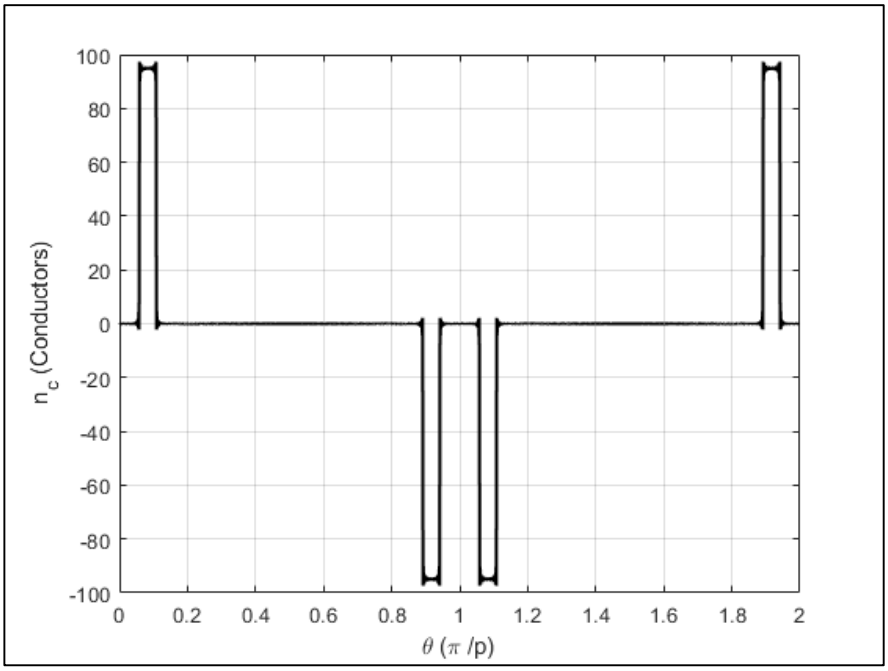

Figure 2-11: Distribution of the conductors of phase 1 along stator bore at mean radius

Figure 2-12 shows the linear distribution of conductors of phase 1 [11], $C_1(\theta)$and its fundamental:

$$C_{1f}(\theta) = C_{fm}cos(p\theta) \qquad (2\text{-}20)$$

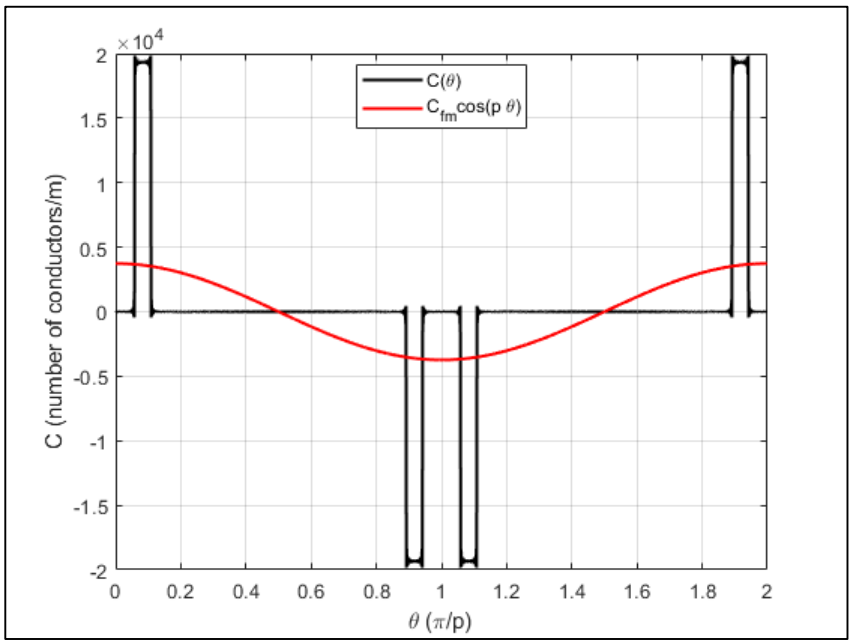

Figure 2-12: Linear distribution of conductors or distribution function of conductors

The magnitude of the fundamental of the current distribution function is given by [11]:

$$C_{fm} = \frac{4n_c}{\pi R_m \alpha} sin\left(\frac{p\alpha}{2}\right) \frac{sin\left(\frac{1}{2} n_{epp} p\theta_d\right)}{sin\left(\frac{1}{2} p\theta_d\right)} \quad (2\text{-}21)$$

where α is the azimuthal angular width of the slot opening and θ_d azimuthal angular width of the tooth pitch. With the numerical values of the parameters involved in this expression the magnitude is:

$$C_{fm} = 3734.8\ conductors/m$$

The magnitude of the surface current density wave is given by [11,13]:

$$K_m = \frac{3}{2} I_m C_{fm} \quad (2\text{-}22)$$

Its 'rms' value is:

$$K_{rms} = 8421\ A.m^{-1}$$

The electromagnetic torque for sinusoidal currents is given by [3,18]:

$$C_{em} = 2\pi(R_2 - R_1) R_m^2 B_{rms} K_{rms} \quad (2\text{-}23)$$

With the numerical data of the parameters in this expression, the value of torque is:

$$C_{em} = 9.94\ N.m$$

The loads characterizing the electromagnetic performances of the motor are:

$$\begin{cases} B_{rms} = 0.24\ T \\ K_{rms} = 8421\ A.m^{-1} \\ \sigma = B_{rms} K_{rms} = 2024\ N.m^{-2} \end{cases} \quad (2\text{-}24)$$

With the geometrical parameters of the motor, the theoretical active mass of the existing motor, its total axial height and its specific torque can be evaluated. The results of this evaluation are summarized in (*TABLE 2-V).*

TABLE 2-V: Mass of the active parts and the theoretical specific torque

Mass of permanent magnets, $M_{AP}(kg)$	0.65
Mass of rotor yoke, $M_{CR}(kg)$	2.45
Theoretical active mass of the rotor , $M_{Rot}(kg)$	3.10
Theoretical active mass of the stator, $M_{Stat}(kg)$	6.6
Theoretical active mass of the motor, $M_{Mot}(kg)$	9.7
Theoretical specific torque, $ST(N.m.kg^{-1})$	1.024
Total axial height, $h_{ref}(mm)$	34.5 mm

2.5 Synthesis of the evaluation of the existing motor

The goal of this first theoretical study is to evaluate the thermal and magnetic loads characterizing the performances of the existing motor.

The values characterizing its no-load magnetic behavior are summarized in *TABLE 2-VI.*

TABLE 2-VI: Characterization of the no-load magnetic behavior	
Magnetic flux density in yoke, $B_{ty}(T)$	1.26
Magnetic flux density in teeth, $B_{zd}(T)$	0.6

The value characterizing its thermal behavior is summarized in *TABLE 2-VII.*

TABLE 2-VII: Characterization of the thermal behavior	
RMS value of current density, $j_{rms}(A.mm^{-2})$	5.0
RMS value of the linear current density, $A_{rms}(A.m^{-1})$	8727.0
Product, $A_{rms}j_{rms}(A^2.m^{-3})$	$4.36\ 10^{10}$

The values that characterize the electromagnetic performance are summarized in *TABLE 2-VIII.*

TABLE 2-VIII: Characterization of the electromagnetic performance	
RMS value of the no-load airgap magnetic flux density, $B_{rms}(T)$	0.24
RMS value of the surface current density , $K_{rms}(A.m^{-1})$	8421.0
Shear stress, $B_{rms}K_{rms}(N.m^{-2})$	2024.0

These values are used to modify the stator and size the rotor of the STAFPM prototype. As the existing motor was sized to have a minimal axial height, it is recalled as a reference height for the followings:

$$h_{ref} = 34.5\ mm$$

2.6 Specifications for the new STAFPM prototype

The existing motor has four pairs of poles and its airgap thickness is $1.0\ mm$. To keep an integer distributed winding, the number of pairs of poles for the new prototype is increased to eight. Thus the number of slots per pole and per phase is unity. The airgap is doubled to $2\ mm$ in order to reduce the axial attractive magnetic force between stator and rotor. This reduce constraints of the fabrication of the rotor. The main parameters are summarized in *TABLE 2-IX*.

TABLE 2-IX: Main parameters for the new prototype

Number of phases, q	3
Number of pairs of poles, p	8
Number of slots per pole per phase, n_{epp}	1
Number of conductors per slot, n_c	95
Number of slots, n_e	48
Number of turns, n_s	760
Copper filling factor, k_{fill}	0.3
Air gap thickness, $e_g(mm)$	2.0

The winding of the stator is changed but all the others parameters like geometrical parameters of the stator are unchanged. The loads for thermal behavior are kept (*TABLE 2-VII*). For the magnetic load only the no-load magnetic flux density in the yoke B_{ty} in *TABLE 2-VI* is kept . The other loads and the other parameters like the geometrical parameters of the rotor are to be calculated.

2.7 Joint sizing of SMAFPM and STAFPM for comparison

To show the benefits of the magnetic flux concentration in the airgap, joint sizing of SMAFPM and STAFPM is done in this section. The two motors have the same specifications and the permanent magnet are Ferrite magnets. For the STAFPM prototype, the Ferrite magnets used are *'FERRAM 27/23'* with $\mu_{ra} = 1.0$ and $J = 0.37\ T$ [47]. These properties are very close to the Ferrite magnets used in the existing SMAFPM motor [16]. Both motors are sized by considering only the electromagnetic torque. The torque due to the saliency of the STAFPM is not taken into account. At first order approximation, the no-load magnetic flux concentration have no effect on this torque. Saliency torque is studied in Chapter 3. Furthermore, the sizing approach at our disposal is mainly based on the loadability concepts and do not take into account saliency.

2.7.1 Arc pole coefficient

The azimuthal angular width θ_{arcpol} of the arc pole of both motors is assumed to be independent of the radial position r and it's defined by the arc pole coefficient β:

$$\theta_{arcpol} = \beta \frac{\pi}{p} \qquad (2\text{-}25)$$

To simplify equations, the half of this coefficient is noted by γ:

$$\gamma = \frac{\beta}{2}$$

The waveform of the no-load magnetic flux density in airgap is rectangular as shown on *Figure 2-13.*

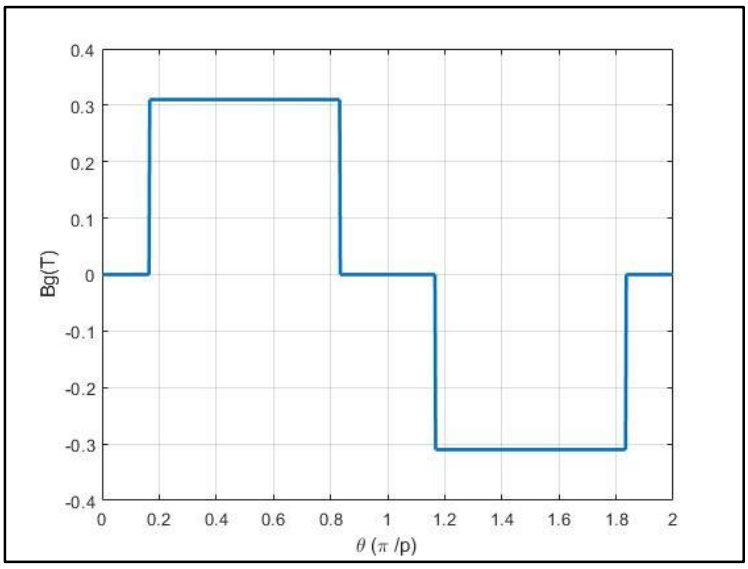

Figure 2-13: Airgap magnetic flux density waveform

If θ is the angular azimuthal position, the magnetic flux density in the airgap $B_g(\theta)$ is the function:

$$\begin{cases} B_g(\theta) = B_{zg} \ , & \left|\frac{\pi}{2p} - \theta\right| \leq \gamma\frac{\pi}{p} \\ B_g(\theta) = -B_{zg} \ , & \left|\frac{3\pi}{2p} - \theta\right| \leq \gamma\frac{\pi}{p} \\ B_g(\theta) = 0 \ , & \left|\frac{\pi}{2p} - \theta\right| > \gamma\frac{\pi}{p} \ \cap \left|\frac{3\pi}{2p} - \right| > \gamma\frac{\pi}{p} \end{cases} \qquad (2\text{-}26)$$

The rectangular signal can be decomposed in its harmonics:

$$B_g(\theta) = \sum_{n=1,3,5\ldots}^{\infty} \frac{4}{\pi}\frac{B_{zg}}{n}\sin(n\frac{\pi}{2})\sin(n\gamma\pi)\sin(np\theta) = \sum_{n=1,3,5\ldots}^{\infty} B_{sn}sin(np\theta) \qquad (2\text{-}27)$$

Figure 2-14 shows the fundamental magnitude B_{s1} as a function of the arc pole coefficient.

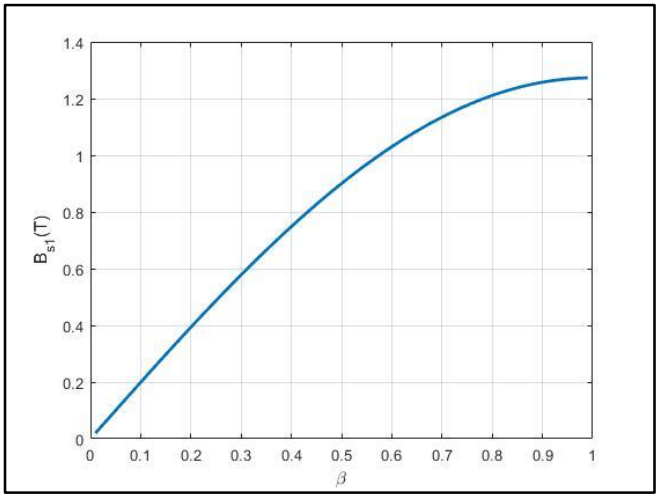

Figure 2-14: Magnitude of the fundamental of $B_g(\theta)$ versus β for $B_{zg} = 1.0\ T$

The Inverse Total Harmonic Distortion τ_F can be defined as:

$$\tau_F = 100\frac{B_{s1}}{\sqrt{\sum_{k=1}^{\infty} B_{S2k-1}^2}} \qquad (2\text{-}28)$$

It can quantify the fundamental ratio in the signal. *Figure 2-14* shows τ_F as a function of the arc pole coefficient. *Figure 2-15* shows that the fundamental ratio is maximal at 97% for an arc pole coefficient of 0.74. The fundamental ratio exceeds 94% for an arc pole coefficient lying between 0.6 and 0.9. In the following, the performances of the two motors are calculated in function of the arc pole coefficient with:

$$0.6 \leq \beta \leq 0.9$$

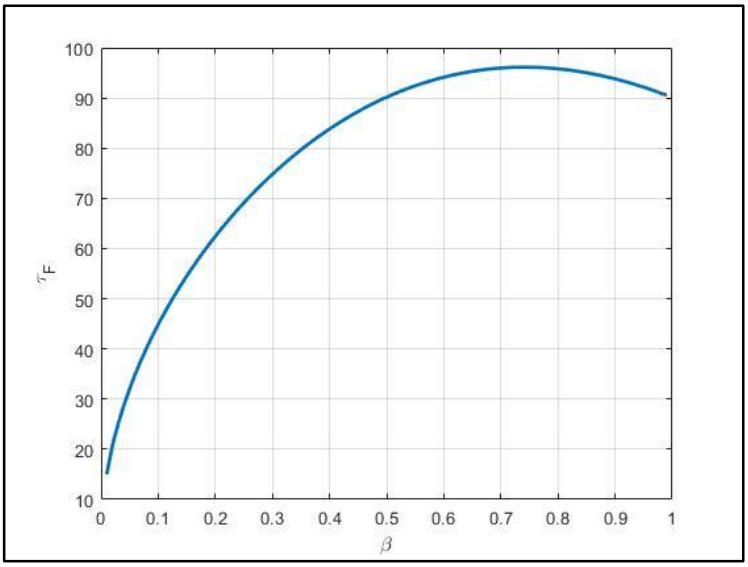

Figure 2-15: Inverse Total Harmonic Distortion τ_F versus β

2.7.2 Armature reaction

The number of poles has changed but the thermal loads on *TABLE 2-VII* and the fill factor did not change. Hence the 'rms' value of the current I_{rms} does not change. But the linear distribution function changes because the number of slots per pole and per phase already changed in (2-19) the new value of the fundamental component is:

$$C_{fm} = \frac{4n_c}{\pi R_m \alpha} sin\left(\frac{p\alpha}{2}\right) = 3854\ conductors/m \qquad (2\text{-}29)$$

From *(2-22)*, the new 'rms' value of the surface current density is:

$$K_{rms} = 8690A.m^{-1}$$

2.7.3 No-load magnetic flux density in the stator and the airgap

To best use magnetically the ferromagnetic circuit of the stator, the maximal value of the magnetic flux density in the yoke must not exceed the value chosen in [16] and evaluated previously:

$$B_{ty} \leq 1.26T$$

The magnetic flux conservation law allows to calculate the new value of the axial airgap flux density B_{zg} which depends on the arc pole coefficient β:

$$B_{zg} = \frac{2h_{cs}B_{ty}}{L_m} = \frac{2h_{cs}B_{ty}}{\beta R_m \frac{\pi}{p}} \qquad (2\text{-}30)$$

The axial magnetic flux density in the teeth is also evaluated by means of the conservation law (see *Figure 2.10* where the flux passes only in two teeth in front of one magnet).

$$B_{zd} = \frac{L_m B_{zg}}{2w_d} = \frac{h_{cs}B_{ty}}{w_d} \qquad (2\text{-}31)$$

2.7.4 Sizing the SMAFPM rotor

The SMAFPM motor is sized only for the purpose of comparison. The sizing model for this motor has been quickly described during the evaluation of the performances of the existing motor. It is now presented in a more formal manner.

The geometrical parameters involved in the sizing model of SMAFPM are summarized in *TABLE 2-X*.

TABLE 2-X: SMAFPM geometrical parameters

Azimuthal length of one pole at mean radius, L_p	$L_p = R_m \frac{\pi}{p}$
Azimuthal length of one magnet at mean radius, L_m	$L_m = \beta L_p$
Axial thickness of airgap, e_g	$e_g = 2.0\ mm$
Permanent magnet axial thickness, h_m	h_m (to be calculated)

The magnetic quantities involved in the sizing model of SMAFPM are summarized in *TABLE 2-XI*.

TABLE 2-XI: SMAFPM magnetic quantities

Airgap axial magnetic flux density	B_{zg}
Permanent magnet axial magnetic flux density	B_{za}
Airgap axial magnetic field intensity	H_{zg}
Permanent magnet axial magnetic field intensity	H_{za}
Permanent magnet axial magnetic polarization	$J = 0.37\ T$
Permanent magnet magnetic relative permeability	$\mu_{ra} = 1.0$

The magnetic equations in the 1D analytical mean radius model of the airgap magnet field are summarized in *TABLE 2-XII*.

TABLE 2-XII: SMAFPM magnetic equations

Magnetic media law in airgap	$B_{zg} = \mu_0 H_{zg}$
Magnetic media law in permanent magnet	$B_{za} = \mu_0 \mu_{ra} H_{za} + J$
Ampere's law *(Figure 2-7)*	$H_{za} h_m + H_{zg} e_g = 0$
Magnetic flux conservation law *(Figure 2-8)*	$B_{zg} = B_{za}$

Constraint related to the axial permanent magnet thickness

From *TABLE 2-XII*, the permanent magnet axial thickness, h_m, is given by:

$$h_m = \mu_{ra} \frac{B_{zg}}{J - B_{zg}} e_g \qquad (2\text{-}32)$$

As the permanent magnet thickness is strictly positive, the airgap magnetic flux density must be strictly less than the magnet polarization:

$$B_{zg} = \frac{2 h_{cs} B_{ty}}{L_m} < J \qquad (2\text{-}33)$$

This strict inequality defines a maximum value of the yoke magnetic flux density:

$$B_{ty} < \left(B_{ty}\right)_{max} = \frac{J\beta L_p}{2h_{cs}} \qquad (2\text{-}34)$$

Figure 2-16 shows $\left(B_{ty}\right)_{mx}$ in function of arc pole coefficient β. It can be seen that $\left(B_{ty}\right)_{max}$ is always less than $1.26\ T$ which is the value chosen to best use the stator.

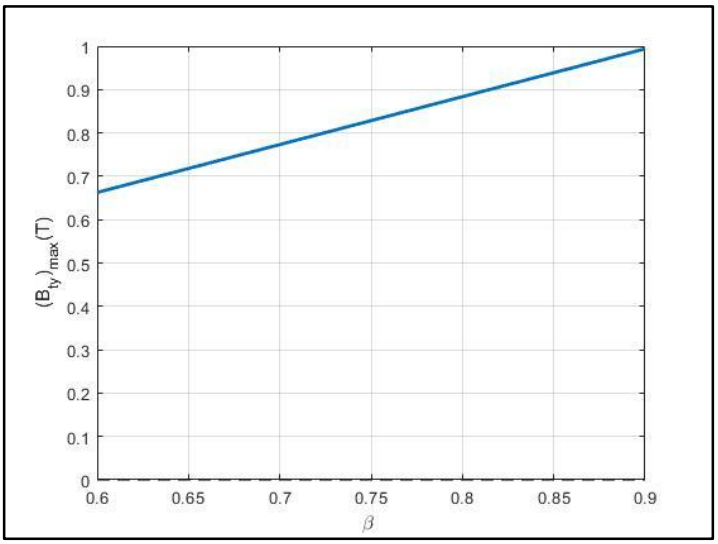

Figure 2-16: $\left(B_{ty}\right)_{max}$ versus β for SMAFPM motor

To fix the value of the magnetic flux density in the yoke, a safety coefficient c_{smpm} is introduced:

$$B_{ty} = c_{smpm}\left(B_{ty}\right)_{max} \qquad (2\text{-}35)$$

For the existing motor, this coefficient is equal to:

$$c_{smpm_{ref}} = \frac{B_{ty}}{\left(B_{ty}\right)_{max}} = \frac{1.26T}{1.51T} = 0.83$$

For the sake of comparison with STAFPM motor, the value chosen is:

$$c_{smpm} = 0.9$$

Knowing the relation between B_{zg} and B_{ty}, leads to simplify the expression of the axial flux density in airgap:

$$B_{zg} = c_{smpm}\, J \qquad (2\text{-}36)$$

Due to magnetic conservation law, B_{za} is equal to B_{zg}, so with the value chosen for the safety coefficient, the no-load magnet flux density in permanent magnet is always higher than B_{opt}. The permanent magnet axial thickness is then given by:

$$h_m = \mu_{ra}\frac{c_{smpm}}{1 - c_{smpm}}e_g \qquad (2\text{-}37)$$

The 'rms' value of the fundamental of the airgap magnetic flux density is calculated from (2-8). The torque is given by [3,18]:

$$C_{em} = 2\pi(R_2 - R_1)R_m^2 B_{rms} K_{rms} \qquad (2\text{-}38)$$

Eventually as for the existing motor, the axial thickness of the rotor yoke is equal to the axial thickness of the stator yoke. The flow chart to calculate the axial thickness of magnets and the electromagnetic torque is given in *Figure 2-17*.

For β from 0.6 to 0.9 *do*

$$(B_{ty})_{max} = \frac{J\beta L_p}{2h_{cs}}$$

$$B_{ty} = c_{smpm}(B_{ty})_{max}$$

$$B_{zg} = c_{smpm}J$$

$$h_m = \mu_{ra}\frac{c_{smpm}}{1 - c_{smpm}}e_g$$

$$B_{za} = B_{zg}$$

$$B_m = \frac{4B_{zg}sin\left(\beta\frac{\pi}{2}\right)}{\pi}$$

$$B_{rms} = \frac{B_m}{\sqrt{2}}$$

$$C_{em} = 2\pi(R_2 - R_1)R_m^2 B_{rms}K_{rms}$$

End for

Figure 2-17: Flow-chart to calculate the main sizes of the rotor of SMAFPM motor and the electromagnetic torque versus the arc pole coefficient β

2.7.5 Sizing the STAFPM rotor

The STAFPM motor has the same stator as the SMAFPM motor. The armature reaction quantities such as j_{rms}, A_{rms}, I_{rms} and K_{rms} have the same values as those of the SMAFPM motor. Same remarks are done considering the relations between B_{zg}, B_{zd} and B_{ty}.

The geometrical parameters involved in the sizing model of STAFPM are defined on *Figure 2-18* an reported in *TABLE 2-XIII.*

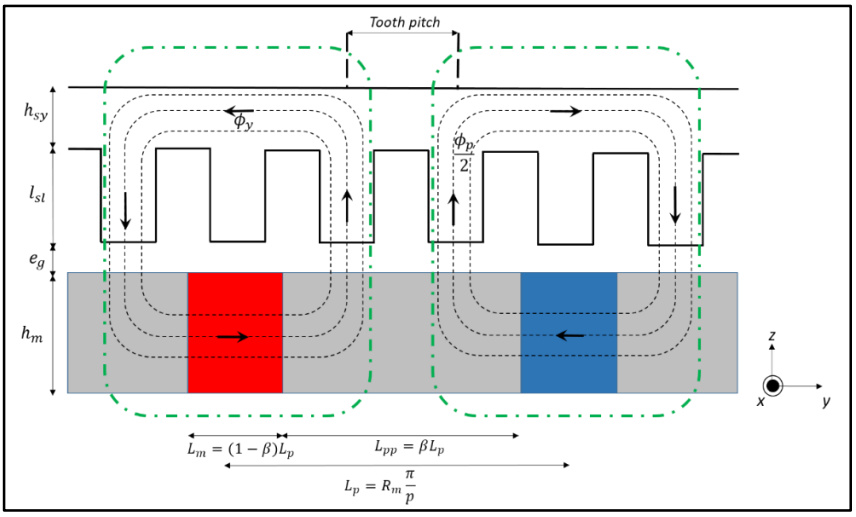

Figure 2-18: Geometric parameters for one pair of poles for STAFPM

TABLE 2-XIII: STAFPM geometrical parameters

Azimuthal length of one pole piece at mean radius, L_{pp}	$L_{pp} = \beta L_p$
Azimuthal length of one magnet at mean radius, L_m	$L_m = (1-\beta)L_p$
Axial thickness of airgap, e_g	$e_g = 2.0\ mm$
Permanent magnet radial thickness, h_m	h_m (to be calculated)

The study domain at the mean radius R_m with smoothed stator is presented on *Figure 2-19*. The azimuthal length of one pole piece at the mean radius is L_{pp} and L_m is the azimuthal length of a magnet. Due to the assumptions, only the magnetic fields in the permanent magnets and the airgap are involved and the material properties of these media are given by the following equations:

$$\begin{cases} \overrightarrow{B_a} = \mu_a \overrightarrow{H_a} + \vec{J} \\ \overrightarrow{B_g} = \mu_0 \overrightarrow{H_g} \end{cases} \quad (2\text{-}39)$$

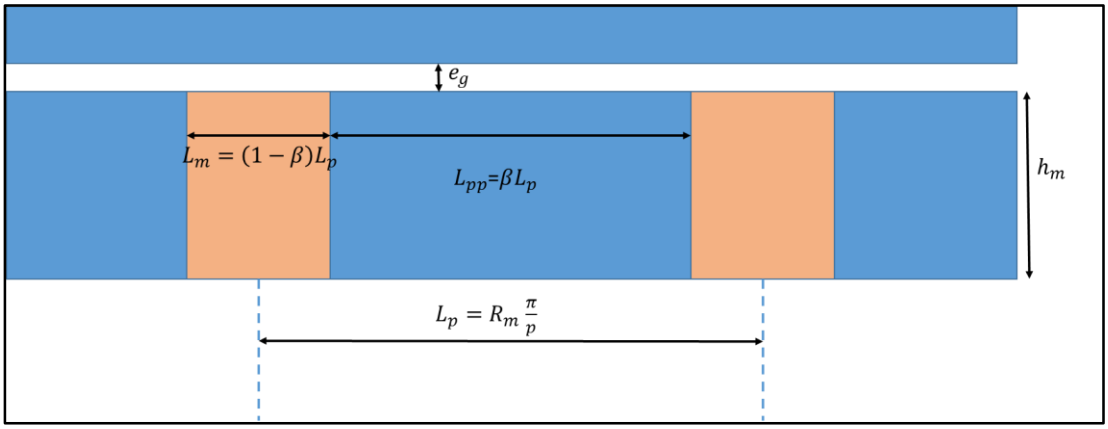

Figure 2-19: Study domain for the evaluation of the airgap flux density

The Ampere's law is applied on the closed path shown in *Figure 2-*.

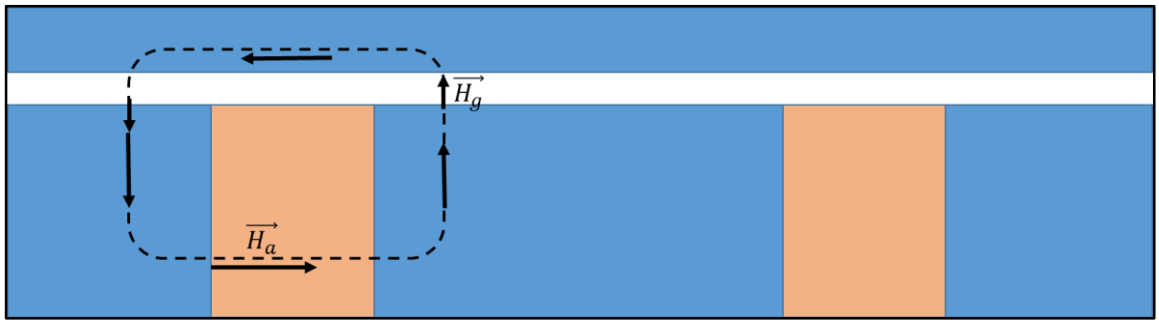

Figure 2-20: Closed path to apply Ampere's law

The azimuthal magnetic field intensities in the permanent magnet (H_{ta}) and in the axial magnetic field intensity in the airgap (H_{zg}) are linked by the following equation *(2-40)*.

$$H_{ta}L_m + 2H_{zg}e_g = 0 \quad (2\text{-}40)$$

Magnetic flux conservation law is applied using surfaces S_g and S_m on *Figure 2-21*.

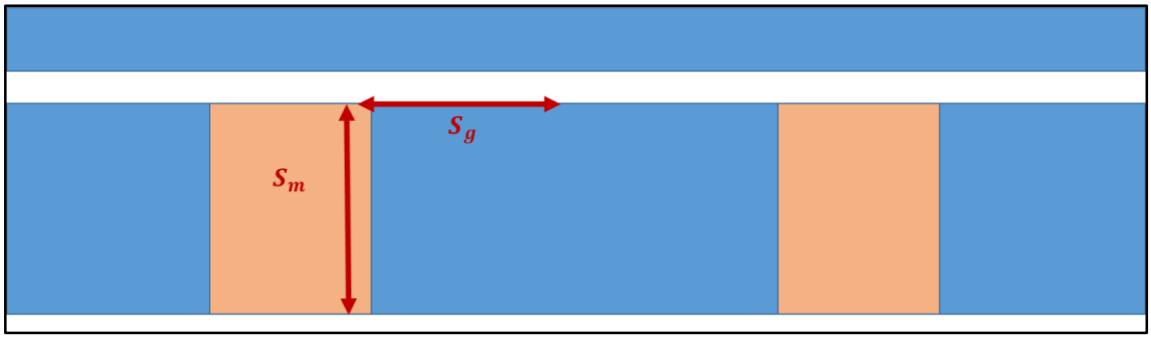

Figure 2-21: Flux conservation law on airgap half surface S_g and magnet surface S_m

The azimuthal magnetic flux density in the permanent magnet (B_{ta}) and the axial magnetic flux density in the airgap (B_{zg}) are linked by the flux conservation law:

$$B_{ta}S_m = B_{zg}S_g \tag{2-41}$$

The following relation is deduced:

$$2h_m B_{ta} = L_{pp}B_{zg} \tag{2-42}$$

The magnetic quantities involved in the sizing model of STAFPM are summarized *TABLE 2-XIV*.

TABLE 2-XIV: STAFPM magnetic quantities

Airgap axial magnetic flux density	B_{zg}
Permanent magnet azimuthal magnetic flux density	B_{ta}
Airgap axial magnetic field intensity	H_{zg}
Permanent magnet azimuthal magnetic field intensity	H_{ta}
Permanent magnet azimuthal magnetic polarization	$J = 0.37\ T$

The magnetic equations in the 1D analytical mean radius model of the airgap magnet field are summarized in *TABLE 2-XV*.

TABLE 2-XV: STAFPM magnetic equations

Magnetic media law in airgap	$B_{zg} = \mu_0 H_{zg}$
Magnetic media law in permanent magnet	$B_{ta} = \mu_0 \mu_{ra} H_{ta} + J$
Ampere's law *(Figure 2-20)*	$H_{ta}L_m + 2H_{zg}e_g = 0$
Magnetic flux conservation law *(Figure 2-21)*	$2h_m B_{ta} = L_{pp}B_{zg}$

Constraint related to the axial permanent magnet thickness

From *TABLE 2-XV*, the permanent magnet axial thickness, h_m, is given by:

$$h_m = \frac{L_m L_{pp} B_{zg}}{2JL_m - 4B_{zg}e_g\mu_{ra}} \tag{2-43}$$

As the thickness must be always strictly positive, this leads to the inequality *(2-44)*.

$$B_{zg} = \frac{2h_{cs}B_{ty}}{L_{pp}} < \frac{JL_m}{2e_g\mu_{ra}} \tag{2-44}$$

To guarantee this inequality, the magnetic flux density in the yoke must be less than a maximal value:

$$B_{ty} < (B_{ty})_{max} = \frac{L_m L_{pp} J}{4 h_{cs} e_g \mu_{ra}} \quad (2\text{-}45)$$

To best use the stator, the magnetic flux density in the yoke must also be less than $1.26T$. According to the numerical values of the parameters involved in the expression *(2-45)*, *Figure 2-22* shows the value of $(B_{ty})_{max}$ in function of arc pole coefficient β.

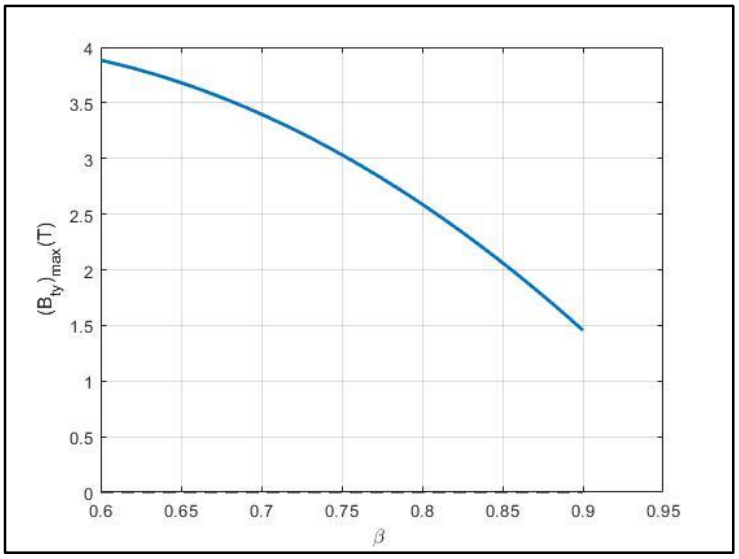

Figure 2-22: $(B_{ty})_{max}$ versus β for STAFPM motor

Figure 2-22 shows that $(B_{ty})_{max}$ is always higher than 1.26 T. So, for STAFPM motor, the magnetic flux density in stator yoke is fixed at:

$$B_{ty} = 1.26\ T$$

Constraint related to the magnetic flux density in permanent magnet

From *TABLE 2-XV*, the azimuthal magnetic flux density in permanent magnet is given by:

$$B_{ta} = \frac{J L_m L_{pp} - 4 B_{ty} h_{cs} e_g \mu_{ra}}{L_{pp} L_m} \quad (2\text{-}46)$$

The permanent magnet must not be demagnetized by a strong armature reaction. For that, the no-load magnetic flux density in permanent magnet must be higher than the optimal magnetic flux density in permanent magnet:

$$B_{ta} > B_{opt} = \frac{J}{2} \quad (2\text{-}47)$$

This constraint leads to the inequality:

$$J L_m\, L_{pp} - B_{opt} L_{pp} L_m > 4 B_{ty} h_{cs} e_g \mu_{ra} \quad (2\text{-}48)$$

From *TABLE 2-XIII*, the arc pole coefficient is submitted to the constraint:

$$(1-\beta)\beta > \frac{8 B_{ty} h_{cs} e_g \mu_{ra}}{J L_p^2} \quad (2\text{-}49)$$

The function defined $y(\beta)$ is introduced:

$$y(\beta) = \beta^2 - \beta + \frac{8B_{ty}h_{cs}e_g\mu_{ra}}{JL_p^2} \quad (2\text{-}50)$$

This function must always be negative for:

$$0.6 \leq \beta \leq 0.9$$

The function $y(\beta)$ can be put in the form:

$$y(\beta) = (\beta - \beta_1)(\beta - \beta_2) \quad (2\text{-}51)$$

The discriminant of the equation $y(\beta) = 0$ is:

$$\Delta = 1 - \frac{32B_{ty}h_{cs}e_g\mu_{ra}}{JL_p^2} = 0.204$$

And:

$$\begin{cases} \beta_1 = \dfrac{1-\sqrt{\Delta}}{2} = 0.274 \\ \beta_2 = \dfrac{1+\sqrt{\Delta}}{2} = 0.7259 \end{cases} \quad (2\text{-}52)$$

It can be shown that:

$$\forall\beta, \qquad max(0.6, \beta_1) < \beta < min(0.9, \beta_2), \qquad y(\beta) < 0$$

Then for the STAFPM motor the valid arc pole coefficient values are:

$$0.6 < \beta < 0.7259 \quad (2\text{-}53)$$

The flow chart to calculate the axial thickness of magnets and the electromagnetic torque is given in *Figure 2-23.*

For β 0.6 to 0.7259 *do*

$L_{pp} = \beta L_p$

$L_m = L_p - \beta L_p$

$B_{zg} = 2B_{ty}\dfrac{h_{cs}}{L_{pp}}$

$h_m = \dfrac{L_m L_{pp} B_{zg}}{2JL_m - 4B_{zg}e_g\mu_{ra}}$

$B_{ta} = \dfrac{L_{pp}}{2hm}B_{zg}$

$B_m = \dfrac{4B_{zg}sin\left(\beta\frac{\pi}{2}\right)}{\pi}$

$B_{rms} = \dfrac{B_m}{\sqrt{2}}$

$C_{em} = 2\pi(R_2 - R_1)R_m^2 B_{rms}K_{rms}$

End for

Figure 2-23: Flow-chart to calculate the main sizes of the rotor and the electromagnetic torque versus the arc pole coefficient β

2.7.6 Comparison of The SMAFPM and STAFPM motors

By respecting the choice of thermal (j_{rms}, A_{rms}) and magnetic (B_{ty}) loads made in [16], the comparison of the electromagnetic torque of the two motors in function of the arc pole coefficient is shown in *Figure 2-24*. The torque of the STAFPM is much higher.

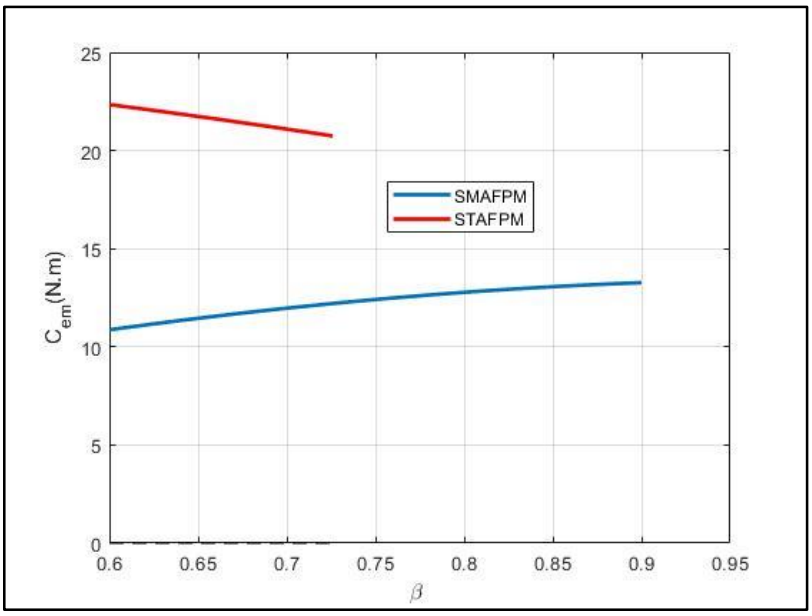

Figure 2-24: Comparison of electromagnetic torque $C_{em}(\beta)$

The performances of the STAFPM is calculated on a shorter interval of the arc pole coefficient because outside this interval *(2-53)* the magnetic flux density in magnet is less than the optimal magnetic flux density in the magnet. *Figure 2-25* shows that SMAFPM motor offers more resistance to demagnetization than STAFPM motor.

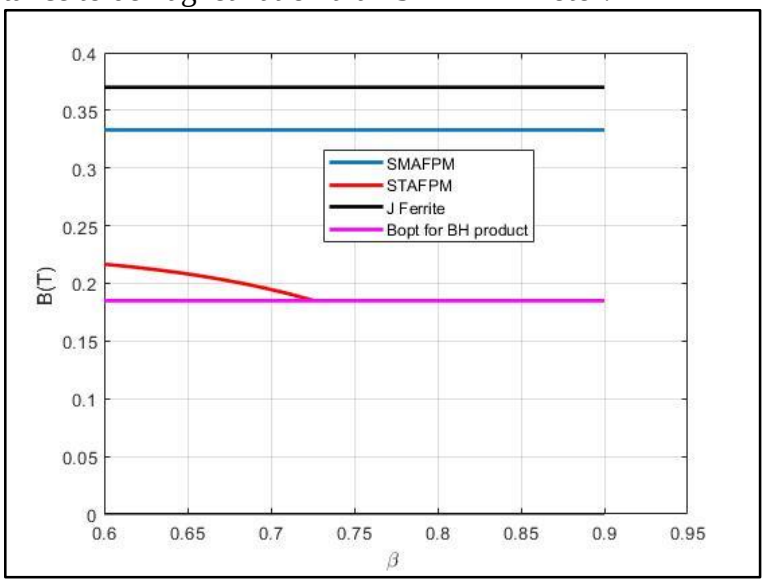

Figure 2-25: Comparison of magnetic flux density in permanent magnet

Figure 2-26 shows that the specific torque of STAFPM motor for an arc pole coefficient β in the interval $[0.6\ ,\ 0.7]$ is always higher than the one of SMAFPM for any value of β

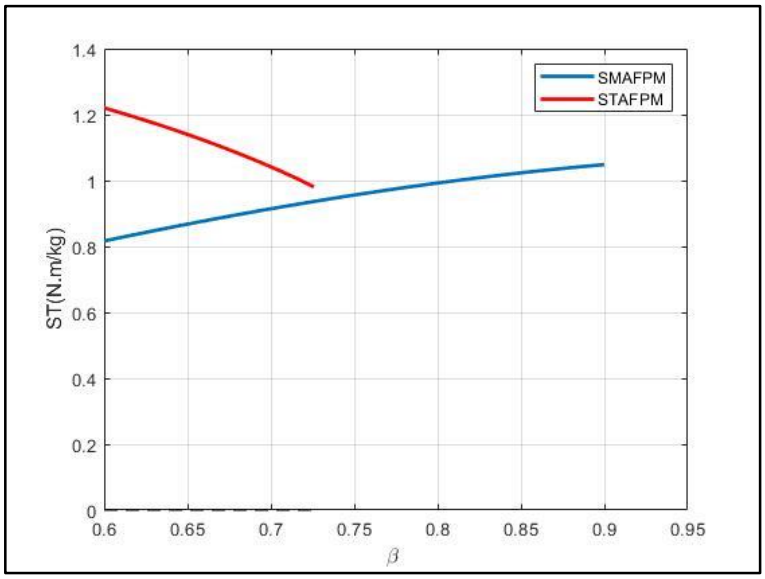

Figure 2-26: Comparison of the specific torque $ST(\beta)$

To characterize the concentration of the no-load magnetic flux in the airgap, the ratio between the no-load magnetic flux density in the airgap and the Ferrite magnet polarization may be used:

$$\tau_{BJ} = \frac{B_{zg}}{J}$$

Figure 2-27 shows that this ratio is less than unity for SMAFPM motor. For STAFPM motor this ratio is decreasing but is always higher than unity. This result shows that the structure in 'spoke-type' allows to concentrate the magnetic flux in the airgap. This is confirmed by the comparison of the magnitude of the fundamental of the no-load flux density in the airgap shown on *Figure 2-28.*

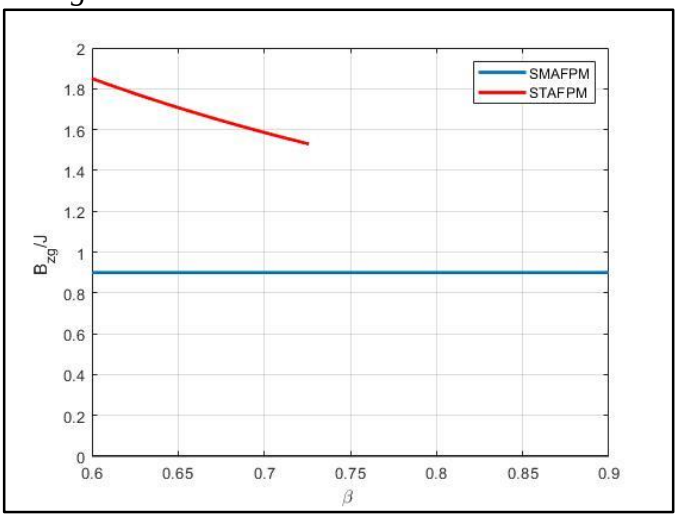

Figure 2-27: Comparison of the ratio $\tau_{BJ}(\beta)$

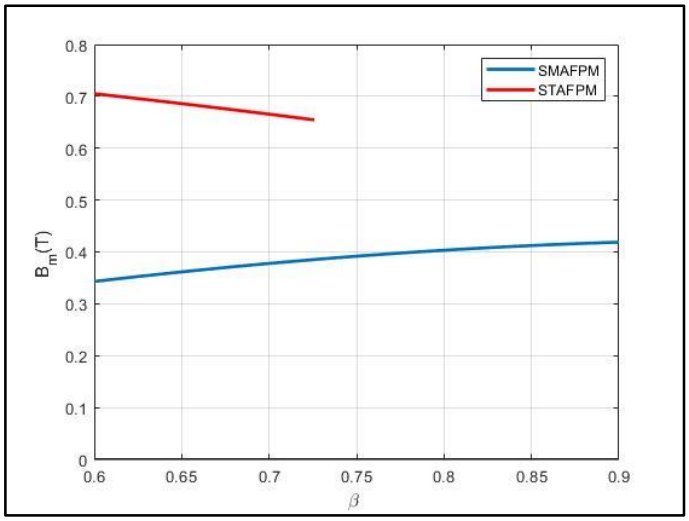

Figure 28: Comparison of the magnitude of the airgap flux density fundamental $B_m(\beta)$

These results show that the electromagnetic and the specific torques of STAFPM motor is higher than those of SMAFPM motor. The effort done to best use the magnetic circuit of the stator is attested by *Figure 2-29* which shows the magnetic flux density in yoke. The structure in 'spoke-type' uses all the magnetic possibility offers by the existing stator. The SMAFPM motor under use the magnetic circuit of the stator.

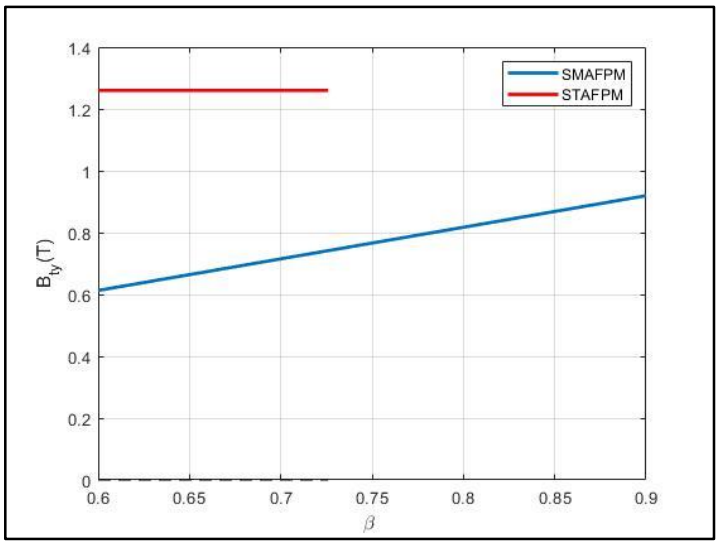

Figure 2-29: Comparison of magnetic flux density in the yoke $B_{ty}(\beta)$

The good performances of STAFPM motor are affected by the total axial thickness of the motor which is at least one and a half the SMAFPM one as shown on *Figure 2-30.*

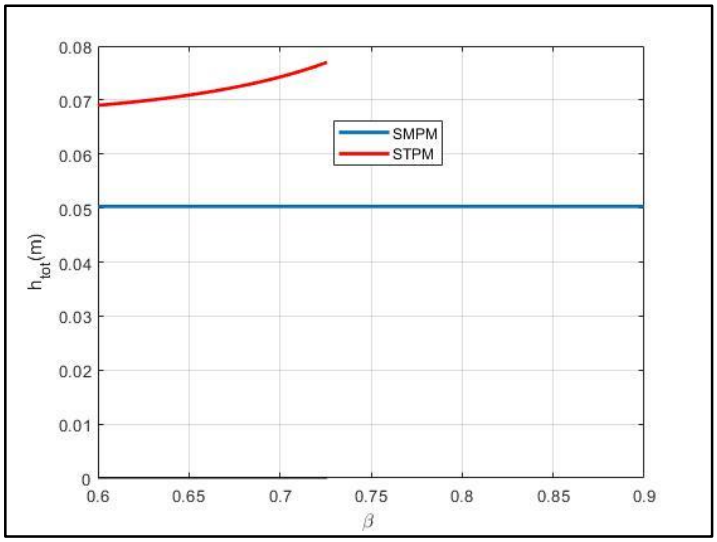

Figure 2-30: Comparison of the total axial thickness $h_{tot}(\beta)$

2.7.7 Conclusion of the comparative study

The comparative study between the SMAFPM and STAFPM motors with the same stator, has been performed by respecting the magnetic and thermal loads chosen in [16].

For a general conclusion on the comparison of SMAFPM and STAFPM motors, it can be deduced that, the STAFPM motor can concentrate the no-load magnetic flux density with very high rate for arc pole coefficient between 0.6 and 0.7. The electromagnetic torque of the STAFPM motor can be much higher, almost twice than the one of the SMAFPM motor. The specific torque of the STAFPM motor can be higher than the one of the SMAFPM motor. The good performances of the STAFPM motor is affected by its axial thickness which is at least one and a half higher than the one of SMAFPM motor.

For a specific conclusion on the new STAFPM motor, dedicated to the experimental study presented in chapter 3, an arc pole coefficient between 0.6 and 0.7 is chosen. In this interval, its specific torque is always higher than the one of SMAFPM motor. However, the no-load magnetic flux density in the yoke must be reduced in order to decrease its axial thickness at the same level as the one of the existing SMAFPM motor $(h_{ref} = 34.5mm)$. We know that the existing motor can be handled on the test bench of the LAPLACE laboratory. It is much difficult to handle a motor of much higher thickness.

2.8 Choice of the new STAFPM prototype

To reduce the total axial thickness of the new prototype, the no-load magnetic flux density in the yoke (B_{ty}) is reduced at a value less than $1.26\,T$. After several tries, the yoke flux density is taken $0.76\,T$. This value takes care that the STAFPM specific torque is higher than the maximal specific torque of SMAFPM motor shown on *Figure 2-26* ($1.05\,Nm.kg^{-1}$).

Figure 2-31 shows that the magnetic circuit of the stator is misused because the no-load magnetic flux density in the yoke of the new STAFPM motor is now lower than 1.26 T.

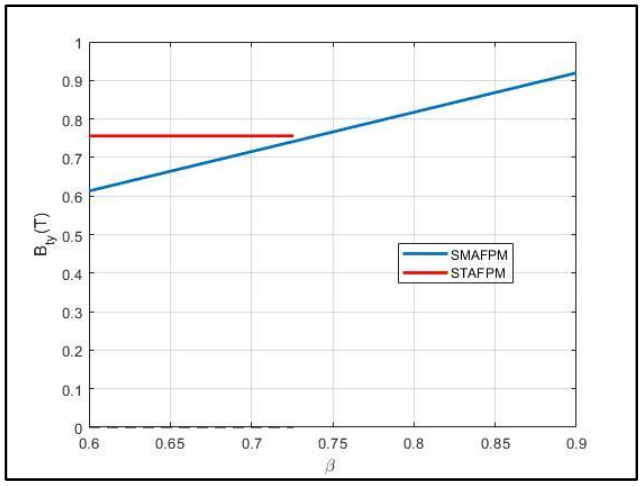

Figure 2-31: New comparison of magnetic flux density in the yoke $B_{ty}(\beta)$

Figure 2-32 shows the new total axial thickness. The total axial thickness of the STAFPM motor is now lower than the one of the SMAFPM motor while its specific torque is higher for arc pole coefficient between 0.6 and 0.68(*Figure 2-33*). The maximal specific torque 1.14 $Nm.kg^{-1}$ is reach for $\beta = 0.6$

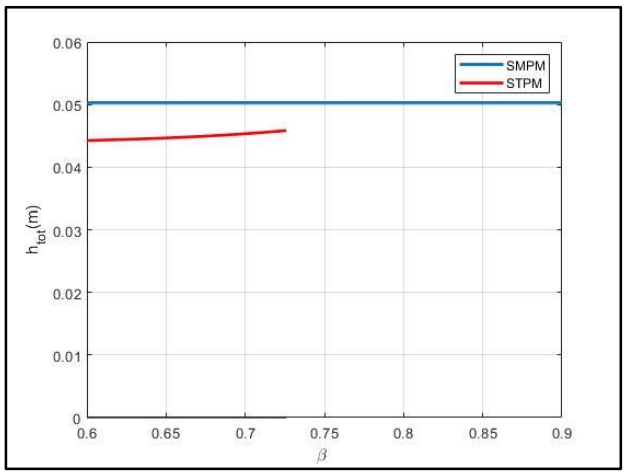

Figure 2-32: New comparison of the total axial thickness $h_{tot}(\beta)$

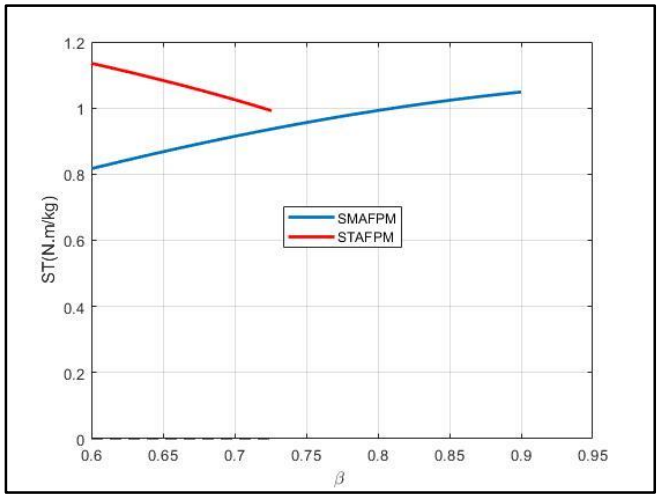

Figure 2-33: New comparison of the specific torque $ST(\beta)$

Figure 2-34 shows that for $\beta = 0.6$ the theoretical electromagnetic torque of STAFPM motor is higher than the one of SMAFPM motor for any valid β.
Figure 2-35 shows that the permanent magnet of the new prototype is better protected against strong demagnetizing armature reaction because the magnetic flux density in permanent magnet is now much higher than B_{opt}.

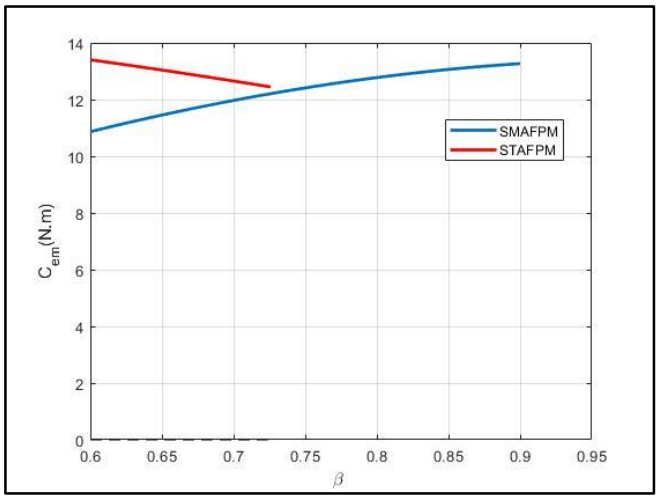

Figure 2-34: New comparison of electromagnetic torque $C_{em}(\beta)$

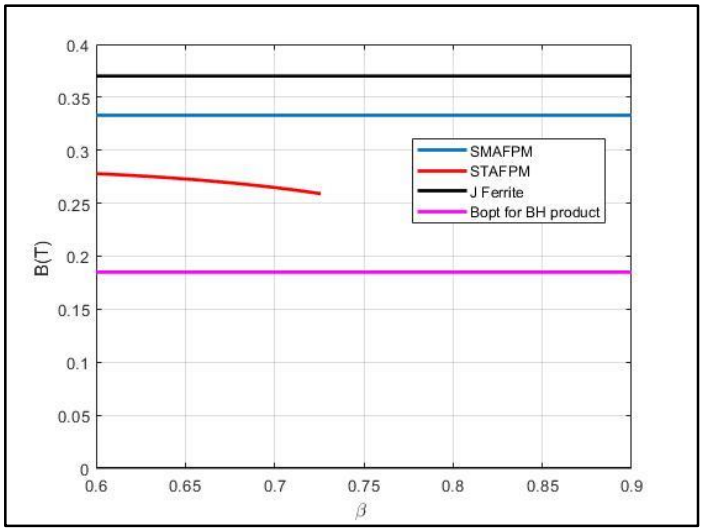

Figure 2-35: New comparison of magnetic flux density in permanent magnet

Figure 2-36 shows that there is still magnetic flux concentration but it has been considerably reduced.

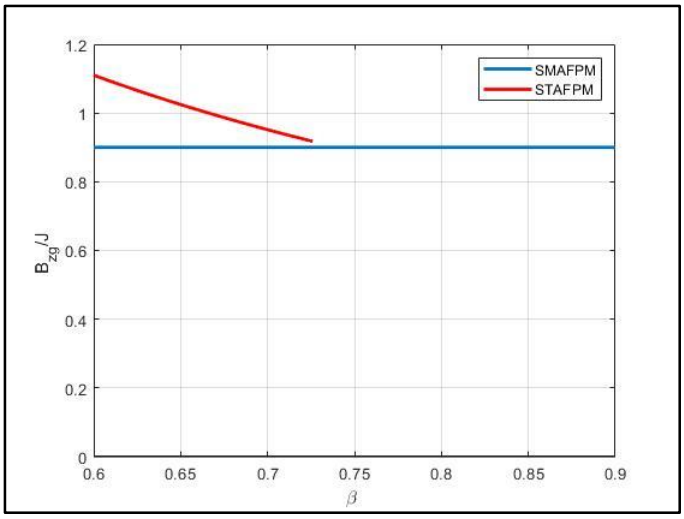

Figure 2-36: New comparison of the ratio $\tau_{BJ}(\beta)$

2.9 Conclusion

In this chapter, the loads of the existing motor have been theoretically evaluated. The results of this evaluation allow to specify the performances of the new prototype.

Before sizing the new prototype, the comparison of SMAFPM and STAFPM motors has been done on electromagnetic torque basis. The comparison shows that, even if the torque due to saliency is neglected, the STAFPM motor can achieved a high rate of no-load magnetic flux concentration in the airgap and a higher specific torque.

To have a STAFPM motor that can be handled on the test bench of the LAPLACE laboratory, the axial thickness of the STAFPM motor has to be reduced at a level near the one of the existing motor.

The reduction of the axial thickness has been obtained by reducing the no-load magnetic flux density in the yoke which means that the stator magnetic circuit is underused. Nevertheless, this reduction has been performed by keeping the overall performances of the STAFPM motor higher than those of SMAFPM motor.

To conclude *TABLE 2-XVI.a* and *TABLE 2-XVII.b* give all the data needed for the fabrication of the new STAFPM prototype. Indeed, *Figure 2-37* and *Figure 2-38* show the new realized stator and the sized rotor with its main geometrical parameters.

TABLE 2-XVI.a: Main STAFPM new prototype stator parameters

Number of phases, q	3
Number of pairs of poles, p	8
Number of slots per pole and per phase, n_{epp}	1
Number of conductors per slot, n_c	95
Number of slots, n_e	48
Number of turns, n_s	760
Copper filling factor, k_{fill}	0.3
Air gap thickness, $e_g(mm)$	2.0

TABLE 2-XVII.b :Main geometrical parameters of the STAFPM new rotor

PM internal radius, R_{int}	100.0 mm
PM external radius, R_{ext}	150.0 mm
PM axial thickness, h_m	23.8 mm
PM azimuthal width at the mean radius, L_m	19.6 mm
PM radial length, l_a	50.0 mm

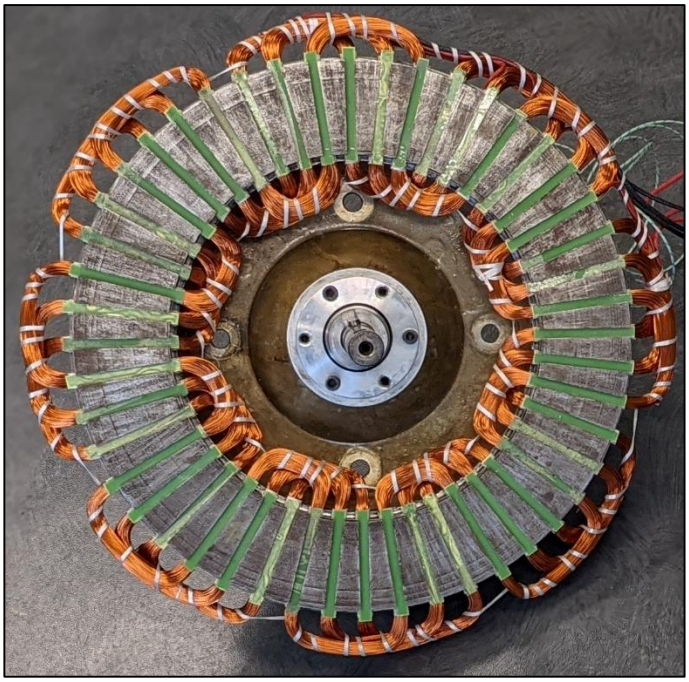

Figure 2-37: New stator realization

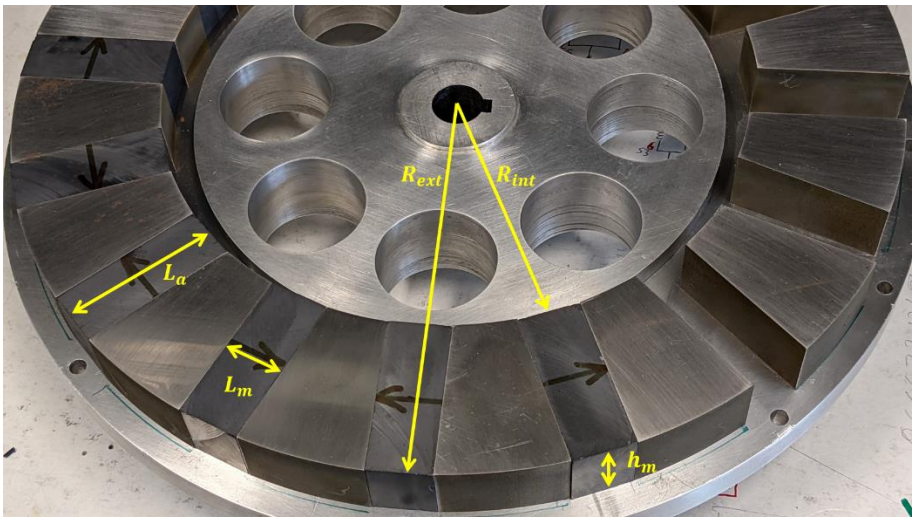

Figure 2-38: STAFPM realized rotor

Chapter 3

Experimental Studies of the STAFPM prototype

3.1 Introduction

In the preceding chapter, the Spoke-Type Axial Flux Permanent Magnet (STAFPM) motor is sized. The motor is fabricated. This chapter is devoted to the experimental studies of this motor to better know its electromechanical behavior.

First, the STAFPM prototype is presented. To guide the experimental studies, the principles of the general electromechanical lumped parameter model is recalled. Physical symmetries of the motor are exploited to deduce some properties of the electromechanical parameters such as the no-load magnetic flux, self and mutual inductances. These properties allow to set up the identification methods of all the parameters of the electromechanical model.

As most of the parameters can be deduced from static torques, an experimental test bench at disposal in the LAPLACE laboratory is presented. This test bench allows to measure static torque in function of the rotor position. In chapter two, the performances of the STAFPM motor has been voluntarily limited in order to facilitate the handling of the motor to be mounted on this test bench.

The measurement set up of this test bench has some imperfections. The measured signals are not perfect and must be treated numerically before their exploitation. The numerical treatments applied on the measured signals are presented.

The motor was received first without permanent magnets. It was an opportunity that has been sized. This opportunity allows to propose an original method to identify some of the parameters of the electromechanical model. Prior to the identification of these parameters a qualitative study based on 2D finite element analysis (FEA) is performed to precise the equilibrium positions of the rotor when the permanent magnets are removed and when the phases of the motor are supplied by DC currents. The numerical treatment to remove signal imperfections, the methods of identification and the identified parameters are validated by additional measurements on the test bench.

When all the parameters of the electromechanical model are identified and validated, a general model of STAFPM motor is at disposal. This model allows to reproduce with high fidelity some important phenomena as torque ripples. Eventually the three phase sinusoidal supplies of this motor are studied by the help of this model. To guide these studies, the parameters of the DQ model of the motor are calculated. Some properties of these parameters are put in light. The optimal torque of the motor may be assessed. Conclusions are made about the sizing model of this type of motor.

3.2 STAFPM prototype

The STAFPM prototype is a three phase axial flux motor and has a single stator and a single rotor. It has eight pole pairs and 48 slots. Each pole of the rotor is made of a Ferrite permanent magnet azimuthally polarized and a ferromagnetic polar piece that concentrate the no-load magnetic flux in the airgap. Chapter two shows that the rate of concentration is not so strong because the total axial thickness is voluntarily limited to facilitate the handling of the prototype. *Figure 3-1* shows a photography of the stator and the rotor.

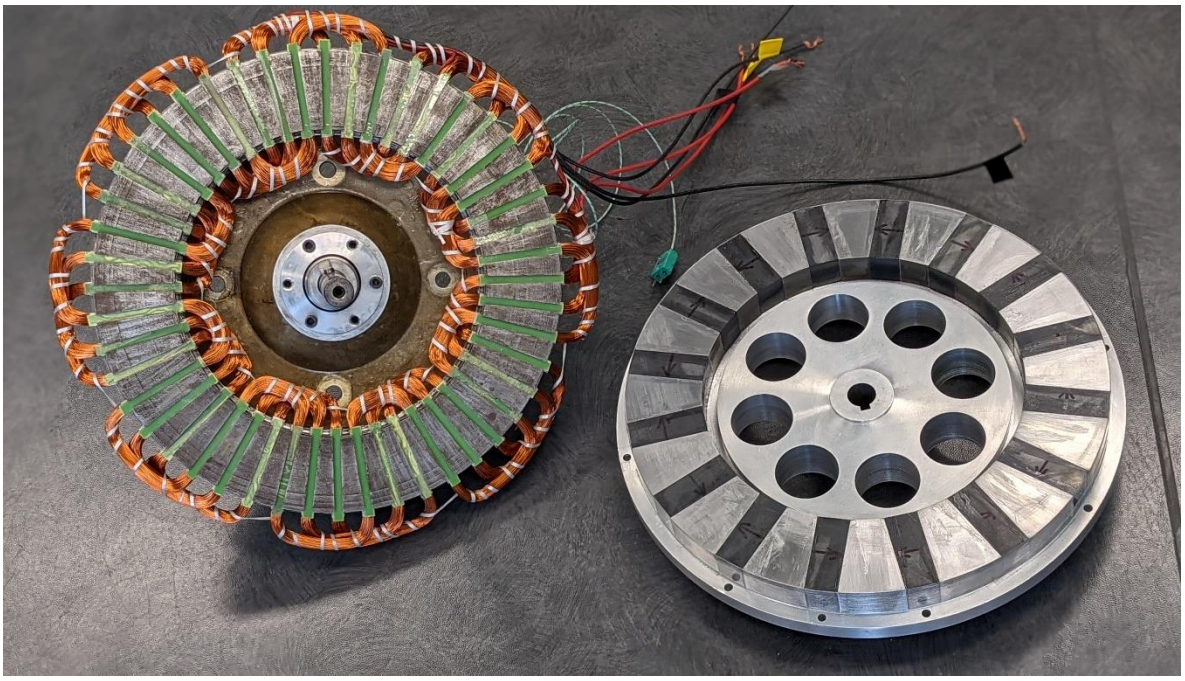

Figure 3-1: Photography of the stator and the rotor

The stator has an integer distributed winding (IDW) topology with one slot per pole and per phase and ninety-five conductors per slot. All the conductors of a phase are all in series, the number of turns is 760. *Figure 3-2* shows the winding diagram on two pole pairs.

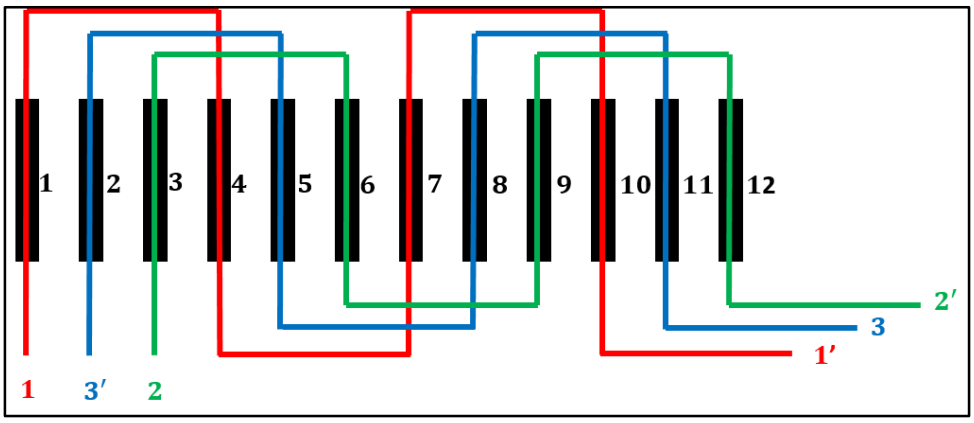

Figure 3-2: Three-phase integer winding developed on two pole pairs

A top view of the stator is shown in *Figure 3-3* (a). The distribution of the conductors by the phase numeration is presented in *Figure 3-3* (b).

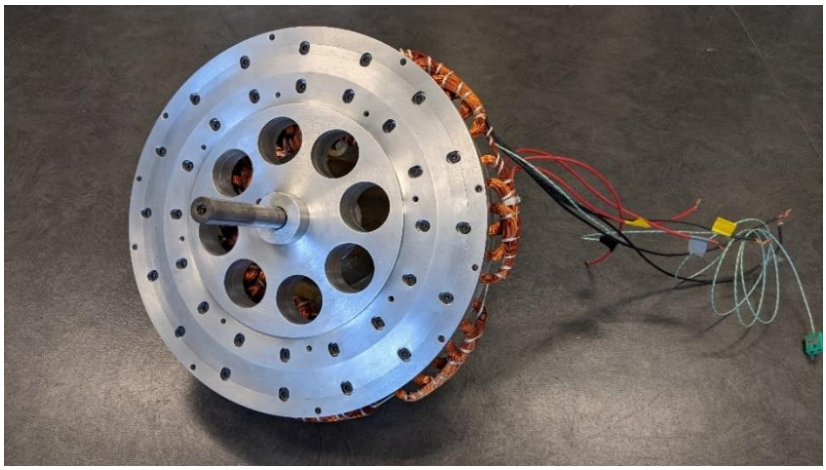

(a)

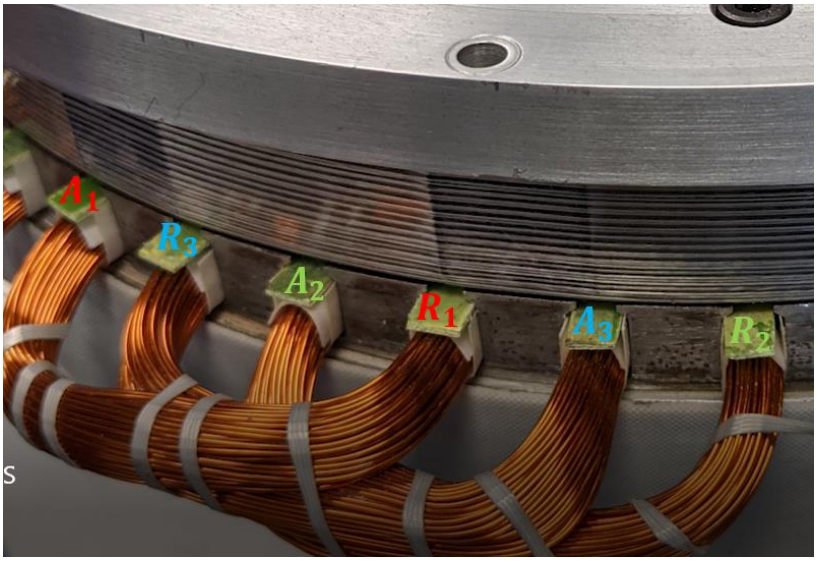

(b)

Figure 3-3: STPMAFM (a) prototype realization, (b) winding distributions

3.3 Electromechanical lumped parameter model

The goal of this chapter is to make experimental studies on the STAFPM to know better some of its properties. The DQ model is the most used model in the studies of electric motors [48]. But this model failed to take into account the phenomena related to the geometry of the magnetic circuit like torque ripples. To guide the experimental studies, a general electromechanical model of electric motors is used. The experimental studies are mainly static studies, so the effects of eddy currents can be neglected. The most general electromechanical model of electric motor is the lumped parameter model [31]. In this section, the principles of electromechanical lumped parameter model are recalled.

3.3.1 Electrical and mechanical quantities

The electromechanical behavior of a rotating electric motor involves electrical quantities X_k such as voltages, currents and fluxes. For a three-phase motor, these quantities are represented by a vector or column matrix whose transpose is expressed by *(3-1):*

$$\boldsymbol{X}^T = \{X\}^T = \{X_1,\ X_2,\ X_3\ \} \tag{3-1}$$

3.3.2 Electrical equations

A receiver convention is chosen. The instantaneous phase voltages $\boldsymbol{V}$, imposed by the electric supply of the motor, are linked to the feeding currents $\boldsymbol{I}$ and induced fluxes $\boldsymbol{\Phi}$ by the following general electrical equation *(3-2).*

$$\boldsymbol{V} = \boldsymbol{R}\boldsymbol{I} + \frac{d}{dt}\boldsymbol{\Phi} \tag{3-2}$$

The matrix of resistances $\boldsymbol{R}$ is a diagonal matrix *(3-4)*. The resistance of a phase is R_s.

$$\boldsymbol{R} = \begin{bmatrix} R_s & 0 & 0 \\ 0 & R_s & 0 \\ 0 & 0 & R_s \end{bmatrix} \tag{3-3}$$

3.3.3 Flux-current relation

Let θ_R^e be the electrical angular position of the rotor axis with respect to the stator *'phase 1'* axis (*Figure 3-4*). If the effects of the saturation of the motor magnetic circuit can be neglected [48], for a permanent magnet synchronous motor (PMSM), the currents and fluxes are linked by the relationship *(3-4).*

$$\boldsymbol{\Phi}(\theta_R^e) = \boldsymbol{\Phi_v}(\theta_R^e) + \boldsymbol{L}(\theta_R^e)\boldsymbol{I} \tag{3-4}$$

The term $\boldsymbol{\Phi_v}(\theta_R^e)$ represents the no-load fluxes in the phases due to the magnetic field produced by the permanent magnets. The inductance matrix $\boldsymbol{L}(\theta_R^e)$ is a symmetric matrix of the form *(3-5).*

$$[\boldsymbol{L}(\theta_R^e)] = \begin{bmatrix} L_1(\theta_R^e) & L_{12}(\theta_R^e) & L_{13}(\theta_R^e) \\ L_{12}(\theta_R^e) & L_2(\theta_R^e) & L_{23}(\theta_R^e) \\ L_{13}(\theta_R^e) & L_{23}(\theta_R^e) & L_3(\theta_R^e) \end{bmatrix} \tag{3-5}$$

3.3.4 Mechanical equations

Let p be the number of pairs of poles. The position of the rotor is described by its mechanical angular position θ_R^m which is related to its electrical angular position θ_R^e *(3-6)*:

$$\theta_R^e = p\theta_R^m \tag{3-6}$$

The rotor speed is given by *(3-7)*:

$$\Omega = \frac{d\theta_R^m}{dt} \tag{3-7}$$

The rotor movement is described by the mechanical equation *(3-8)* :

$$J\frac{d\Omega}{dt} = C_{mot} - C_{res}(\Omega) \tag{3-8}$$

The resistive torque $C_{res}(\Omega)$ takes into account the torque imposed by the mechanical load and the various frictional torques exerted on the rotor. This torque generally depends on the rotational speed Ω. The torque developed by the motor C_{mot} is the sum of the cogging torque $C_d(\theta_R^m)$, the saliency torque $C_{sail}\ (\theta_R^m)$and the electromagnetic torque $C_{em}\ (\theta_R^m)$ as shown in *(3-9).*

$$C_{mot}(\theta_R^m) = C_d(\theta_R^m) + \frac{1}{2}\boldsymbol{I}^T\frac{d\boldsymbol{L}(\theta_R^m)}{d\theta_R^m}\boldsymbol{I} + \boldsymbol{I}^T\frac{d\boldsymbol{\Phi_v}(\theta_R^m)}{d\theta_R^m} \tag{3-9}$$

3.3.5 System of electromechanical equations

The electromechanical behavior of the motor is represented by the following system of differential equations in *(3-10).*

$$\begin{cases} \boldsymbol{V} = \boldsymbol{R}\boldsymbol{I} + \dfrac{d}{dt}\boldsymbol{\Phi} \\ \boldsymbol{\Phi}(\theta_R^m) = \boldsymbol{\Phi_v}(\theta_R^m) + \boldsymbol{L}(\theta_R^m)\boldsymbol{I} \\ C_{mot}(\theta_R^m) = C_d(\theta_R^m) + \dfrac{1}{2}\boldsymbol{I}^T\dfrac{d\boldsymbol{L}(\theta_R^m)}{d\theta_R^m}\boldsymbol{I} + \boldsymbol{I}^T\dfrac{d\boldsymbol{\Phi_v}(\theta_R^m)}{d\theta_R^m} \\ J\dfrac{d^2\theta_R^m}{dt^2} = C_{mot} - C_{res}(\dfrac{d\theta_R^m}{dt}) \end{cases} \tag{3-10}$$

In this set of differential equations, the parameters, inputs and outputs are decomposed as:
- Motor parameters: $\boldsymbol{R}$, $\boldsymbol{\Phi_v}(\theta_R^m)$, $\boldsymbol{L}(\theta_R^m)$ and $C_d(\theta_R^m)$
- Mechanical parameters: moment of inertia $J(kg \cdot m^2)$
- Electrical input data: $\boldsymbol{V}$
- Input mechanical data: $C_{res}(\Omega)$
- Output data : $\boldsymbol{I}$, $\boldsymbol{\Phi}$ and θ_R^m

3.4 Symmetrical motor

The motor geometry and physical properties of a synchronous motor with p pole pairs present an angular periodicity equal to $\frac{2\pi}{p}$. This is why most of the parameters and the physical quantities are function of the electrical angular position θ_R^e. *Figure 3-4* shows the so called electrical domain and the definition of θ_R^e. The cross labeled by G_k mention the position the position of the 'go' conductors of phase k and the arrow labeled R_j the 'return' conductors' of phase j. The followings general symmetrical properties are deduced from the theory of salient pole machine when the effects of magnetic circuit saturation are neglected [48].

3.4.1 Symmetries of the no-load flux

As the number of slots per pole and per phase is an integer, the axis of 'phase 1', called also the horizontal axis (*Figure 3-4*), is an axis of symmetry for the no-load flux of 'phase 1'

$$\phi_{v1}(\theta_R^e) = \phi_{v1}(-\theta_R^e) \tag{3-11}$$

So the no-load flux of phase 1 can decomposed in harmonics of the form:

$$\phi_{v1}(\theta_R^e) = \sum_{n=1}^{\infty} f_n cos(n\theta_R^e)$$

It can be expressed also in function of the mechanical angular position:

$$\phi_{v1}(\theta_R^m) = \sum_{n=1}^{\infty} f_n cos(np\theta_R^m) \tag{3.12}$$

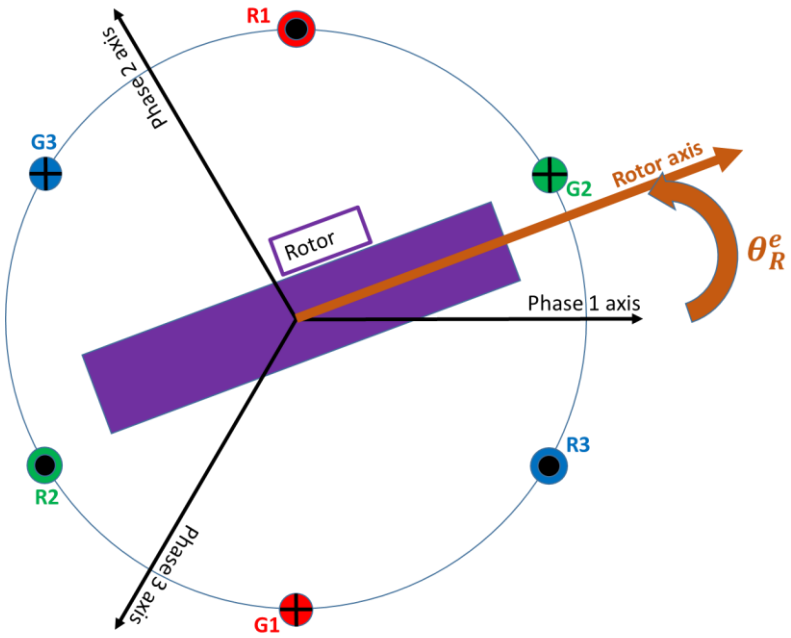

Figure 3-4: Definition of θ_R^e in the electrical domain

The no-load flux of 'phase k' is:

$$\phi_{vk}(\theta_R^m) = \phi_{v1}\left(p\theta_R^m - (k-1)\frac{2\pi}{3}\right) = \sum_{n=1}^{\infty} f_n cos\left(n\left(p\theta_R^m - (k-1)\frac{2\pi}{3}\right)\right) \tag{3.13}$$

3.4.2 Symmetries of the self-inductances

The self-inductance of phase 1 has a periodicity of $\frac{\pi}{p}$ and the horizontal axis constitutes for it an axis of symmetry:

$$L_1(\theta_R^e) = L_1(-\theta_R^e)$$

So it could be expressed by its harmonics in the form:

$$L_1(\theta_R^m) = L_s + \sum_{n=1}^{\infty} l_n cos(2np\theta_R^m)$$

The self-inductance of 'phase k' is:

$$L_k(\theta_R^m) = L_1\left(p\theta_R^m - (k-1)\frac{2\pi}{3}\right) = L_s + \sum_{n=1}^{\infty} l_n cos\left(2n\left(p\theta_R^m - (k-1)\frac{2\pi}{3}\right)\right) \quad (3.14)$$

3.4.3 Symmetries of the mutual inductances

The mutual inductance between phase 2 and phase 3 has the same symmetry and periodicity as the self-inductance of phase 1. So it can be expresses by its harmonics in the form:

$$L_{23}(\theta_R^m) = M_s + \sum_{n=1}^{\infty} m_n cos(2np\theta_R^m) \quad (3.15)$$

The other mutual inductances are:

$$\begin{cases} L_{31}(\theta_R^m) = M_s + \sum_{n=1}^{\infty} m_n cos\left(2n\left(p\theta_R^m - \frac{2\pi}{3}\right)\right) \\ L_{12}(\theta_R^m) = M_s + \sum_{n=1}^{\infty} m_n cos\left(2n\left(p\theta_R^m - \frac{4\pi}{3}\right)\right) \end{cases} \quad (3.16)$$

Let's note:

$$\begin{cases} M_1(\theta_R^m) = L_{23}(\theta_R^m) \\ M_2(\theta_R^m) = L_{31}(\theta_R^m) \\ M_3(\theta_R^m) = L_{12}(\theta_R^m) \end{cases} \quad (3.17)$$

It can be written:

$$M_k(\theta_R^m) = M_s + \sum_{n=1}^{\infty} m_n cos\left(2n\left(p\theta_R^m - (k-1)\frac{2\pi}{3}\right)\right) \quad (3.18)$$

3.5 Identification method of the torque model parameters

The electromechanical model contains a torque model that allows to calculate the torque if the position of the rotor θ_R^m and the phase currents $I_k(\theta_R^m)$ considered as functions of the rotor position are known. This model is:

$$C_{mot}(\theta_R^m) = C_d(\theta_R^m) + \frac{1}{2}\boldsymbol{I}^T \frac{d\boldsymbol{L}(\theta_R^m)}{d\theta_R^m}\boldsymbol{I} + \boldsymbol{I}^T \frac{d\boldsymbol{\Phi_v}(\theta_R^m)}{d\theta_R^m} \quad (3.19)$$

The parameters of this model are:

- $C_d(\theta_R^m)$: the cogging torque in function of rotor position;
- $\frac{d\boldsymbol{\Phi_v}(\theta_R^m)}{d\theta_R^m}$: the derivative of the no-load flux in function of the rotor position;
- $\frac{d\boldsymbol{L}(\theta_R^m)}{d\theta_R^m}$: the derivative of the matrix inductance in function of the rotor position.

This section is dedicated to the identification methods of the torque model parameters.

3.5.1 Identification of the derivative of the matrix inductance

The ferromagnetic polar pieces are mounted first on the rotor. *Figure 3-5* shows a photography of the rotor without permanent magnets. If the rotor is free of permanent magnets, the cogging torque $C_d(\theta_R^m)$ and the electromagnetic torque C_{em} (θ_R^m) are null. The torque of the motor is equal to the saliency torque *(3-20)*:

$$C_{mot}(\theta_R^m) = \frac{1}{2}\boldsymbol{I}^T \frac{d\boldsymbol{L}(\theta_R^m)}{d\theta_R^m}\boldsymbol{I} \qquad (3\text{-}20)$$

If it is possible to measure the torque $C_{mot}(\theta_R^m)$ in function of the position of the rotor θ_R^m, the derivative of the self-inductances $\frac{dL_k(\theta_R^m)}{d\theta_R^m}$ and the derivative of mutual inductances $\frac{dL_{ij}(\theta_R^m)}{d\theta_R^m}$ can be identified experimentally.

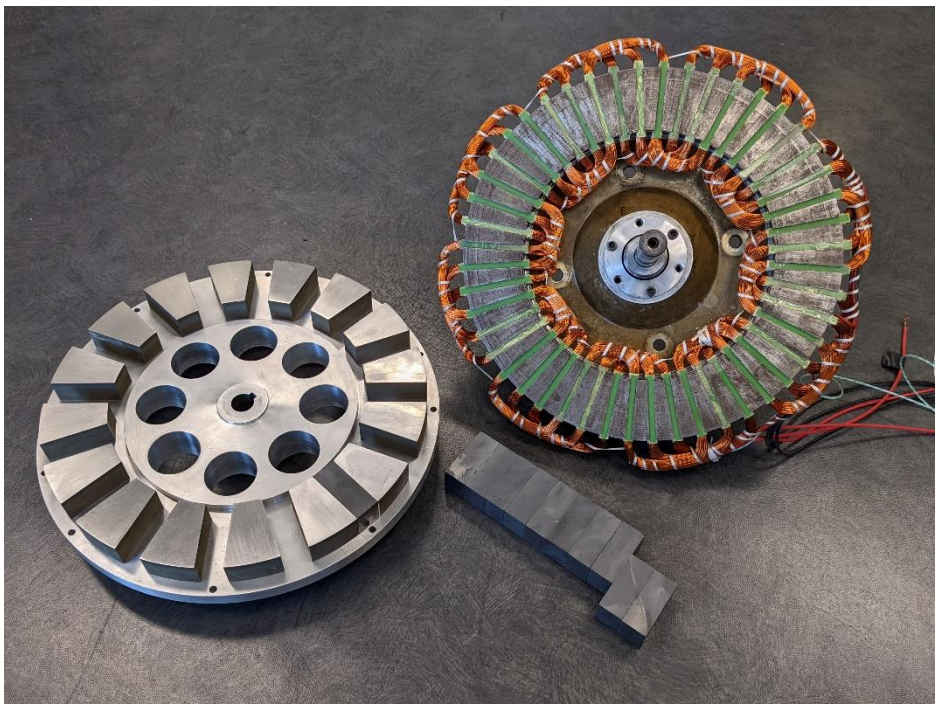

Figure 3-5: The rotor before permanent magnet mounting on the rotor

Assuming that only *'phase k'* is supplied by a DC current I_c while the rotor change position at a very low speed, its current is:

$$I_k(\theta_R^m) = I_c$$

The torque is then given by:

$$C_{Rk}(\theta_R^m) = \frac{1}{2}\frac{dL_k(\theta_R^m)}{d\theta_R^m} I_c^2 \qquad (3\text{-}21)$$

Thus the derivative of the self-inductance of each phase as a function of the rotor position θ_R^m is identified by:

$$\frac{dL_k(\theta_R^m)}{d\theta_R^m} = \frac{2C_{Rk}(\theta_R^m)}{I_c^2} \qquad (3\text{-}22)$$

Assuming that *'phase 2'* and *'phase 3'* are supplied in anti-series connection by a DC current I_c, their currents are:

$$\begin{cases} I_1(\theta_R^m) = 0 \\ I_2(\theta_R^m) = I_c \\ I_3(\theta_R^m) = -I_c \end{cases}$$

The torque is then given by *(3-23):*

$$C_{R23}(\theta_R^m) = \frac{1}{2}\left(\frac{dL_2(\theta_R^m)}{d\theta_R^m} + \frac{dL_3(\theta_R^m)}{d\theta_R^m} - 2\frac{dM_1(\theta_R^m)}{d\theta_R^m}\right) I_c^2 \qquad (3\text{-}23)$$

Thus the derivative of the mutual inductance $\frac{dL_{23}(\theta_R^m)}{d\theta_R^m}$ is:

$$\frac{dM_1(\theta_R^m)}{d\theta_R^m} = \frac{dL_{23}(\theta_R^m)}{d\theta_R^m} = \frac{1}{2}\left(\frac{dL_2(\theta_R^m)}{d\theta_R^m} + \frac{dL_3(\theta_R^m)}{d\theta_R^m} - 2\frac{C_{R23}(\theta_R^m)}{I_c^2}\right) \qquad (3\text{-}24)$$

3.5.2 Identification method of the cogging torque

When the permanent magnet are mounted between ferromagnetic polar pieces on the rotor like on *Figure 3-1* and if it is possible to measure the torque $C_{mot}(\theta_R^m)$ in function of the position of the rotor θ_R^m, the cogging torque is measured when all current are null :

$$C_{mot}(\theta_R^m) = C_d(\theta_R^m) \qquad (3.25)$$

3.5.3 Identification method of the derivative of no-load flux

The no-load e.m.f. of the phase k, e_{vk} can be measured when all current are with voltmeter and is linked to derivative of no-load flux:

$$e_{vk}(t) = \frac{d\phi_{vk}}{dt} = \frac{d\theta_R^m}{dt}\frac{d\phi_{vk}}{d\theta_R^m} = \Omega\frac{d\phi_{vk}}{d\theta_R^m} \qquad (3.26)$$

During measurement, the speed of the rotor Ω is constant so it is easy to change variables:

$$\frac{d\phi_{vk}}{d\theta_R^m}(\theta_R^m) = \frac{1}{\Omega}e_{vk}(\theta_R^m) \qquad (3.27)$$

3.6 Identification of the flux model parameters

The electromechanical model contains also a flux model that allows to calculate the flux $\phi_k(\theta_R^m)$ in each phase k if the position of the rotor θ_R^m and all the phase currents $I_j(\theta_R^m)$ considered as functions of the rotor position are known. This model is:

$$\phi_k(\theta_R^m) = \phi_{vk}(\theta_R^m) + \sum_{j=1}^{3} L_{kj}(\theta_R^m) I_j(\theta_R^m) \qquad (3.28)$$

The parameters of this model are:

- $\phi_{vk}(\theta_R^m)$: the no-load flux of phase k in function of rotor position;
- $L_k(\theta_R^m) = L_{kk}(\theta_R^m)$: the self-inductance of phase k in function of the rotor position;
- $L_{kj}(\theta_R^m)$: the mutual inductance of phase k with a different phase j in function of the rotor position.

This section is dedicated to the identification methods of the flux model parameters.

3.6.1 Identification method of the no-load flux

According to the expression of the no-load flux of phase k (3.13) in function of the position of the rotor θ_R^m, its derivative can be expressed with its harmonics as:

$$\frac{d\phi_{vk}}{d\theta_R^m}(\theta_R^m) = \sum_{n=1}^{nh} df_n \, sin\left(n\left(p\theta_R^m - (k-1)\frac{2\pi}{3}\right)\right) \tag{3.29}$$

The term df_n is the harmonic of rank n deduced from measurement and the harmonic of the no-load flux is given by:

$$f_n = -\frac{df_n}{np} \tag{3.30}$$

3.6.2 Identification method of the self-inductances

According to the expressions of the self-inductance $L_k(\theta_R^m)$ in (3.14) in function of the position of the rotor, its derivative can be expressed with its harmonics as:

$$\frac{dL_k}{d\theta_R^m}(\theta_R^m) = \sum_{n=1}^{nh} dl_n \, sin\left(2n\left(p\theta_R^m - (k-1)\frac{2\pi}{3}\right)\right) \tag{3.31}$$

The term dl_n is the harmonic of rank n deduced from measurement and the harmonic of the self-inductance is given by:

$$l_n = -\frac{dl_n}{2np} \tag{3.32}$$

The value of the self-inductance $L_1(\theta_R^L)$ is measured by classical electrical test for a particular rotor position θ_R^L then the mean value L_s of the self-inductance is given by:

$$L_s = L_1(\theta_R^L) - \sum_{n=1}^{\infty} l_n cos(2np\theta_R^L) \tag{3.33}$$

The particular rotor position θ_R^L is chosen latter.

3.6.3 Identification method of the mutual inductances

According to the expressions of the mutual inductance $M_k(\theta_R^m)$ in (3.18) in function of the position of the rotor, its derivative can be expressed with its harmonics as:

$$\frac{dM_k}{d\theta_R^m}(\theta_R^m) = \sum_{n=1}^{nh} dm_n \, sin\left(2n\left(p\theta_R^m - (k-1)\frac{2\pi}{3}\right)\right) \tag{3.34}$$

The term $dm_n$is the harmonic of rank n deduced from measurement and the harmonic of the self-inductance is given by:

$$m_n = -\frac{dm_n}{2np} \tag{3.35}$$

The value of the mutual inductance $M_k(\theta_R^m)$ is measured by classical electrical test for a particular rotor position θ_R^m. Then the mean value M_s of the mutual inductance is given by:

$$M_s = M_k(\theta_R^m) - \sum_{n=1}^{\infty} m_n cos\left(2n\left(p\theta_R^m - (k-1)\frac{2\pi}{3}\right)\right) \tag{3.36}$$

The particular rotor position θ_R^m is chosen latter.

3.7 Experimental test bench

To measure the torque of the motor in function of the rotor position, an experimental test bench has been set up. *Figure 3-6* shows a general view of the test bench.

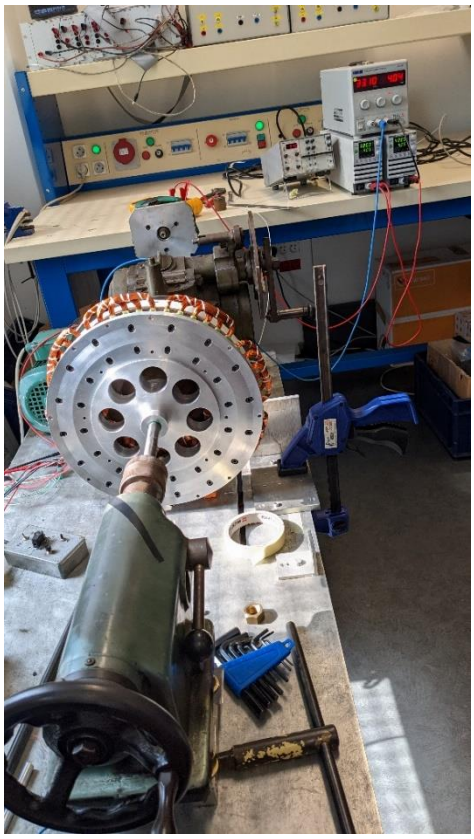

Figure 3-6: A general view of the experimental test bench

The rotor is driven at a constant speed by a motor. The speed is adjusted at the beginning of a test. The phases of the stator winding are supplied by a DC current source. Three types of supply can be performed easily by connecting adequately the phases as shown on *TABLE 3-I*. The stator is mounted on the bench free to rotate around its bearing. Then a force sensor is fixed on the stator to measure any tangential force F_T^S exerted on the stator. The point of

application of the force sensor is located near the external edge of the stator whose distance to the rotor axis is:

$$r_{FS} = 134.7\ mm \tag{3.37}$$

The force sensor delivers a voltage V_F proportional to the tangential force F_T^S with a coefficient:

$$F_T^S = c_{FV} V_F$$

The voltage V_F is measured by voltage meter and the torque applied on the stator is given by:

$$C_{Stat} = r_{FS} c_{FV} V_F$$

Due to action reaction principle, the torque applied on the rotor is:

$$C_{Rot} = -C_{Stat} = -r_{FS} c_{FV} V_F \tag{3.38}$$

Figure 3-7 shows more details around the motor. The white cable linking the force sensor to the voltage meter is noticeable.

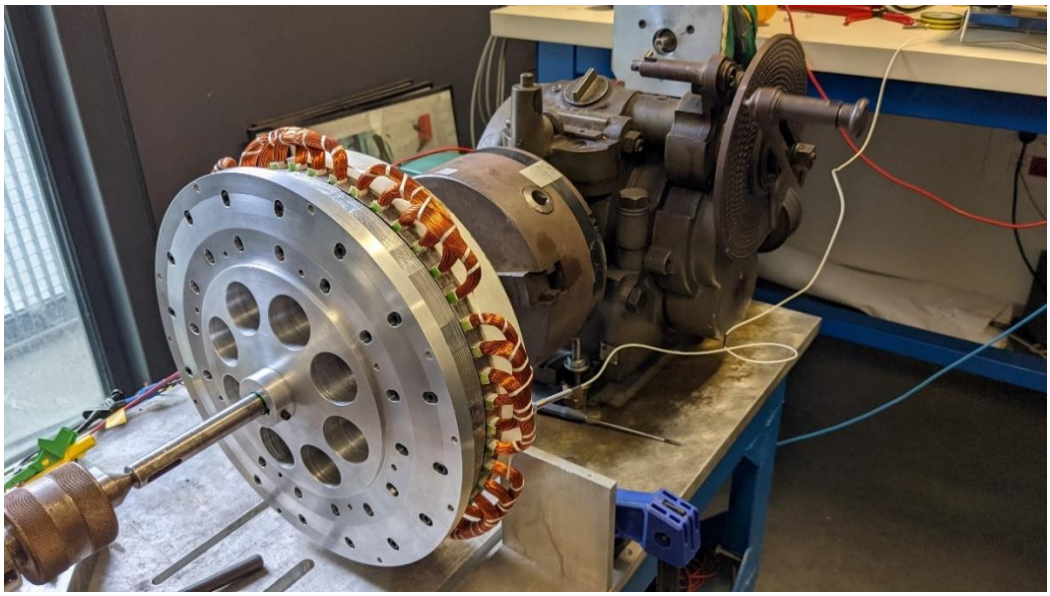

Figure 3-7: Detailed view around the motor

TABLE 3-I: Types of supply and phases connections

Single phase supply	Double phase supply	Three phase supply
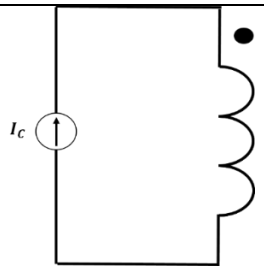	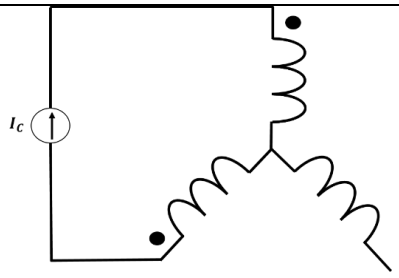	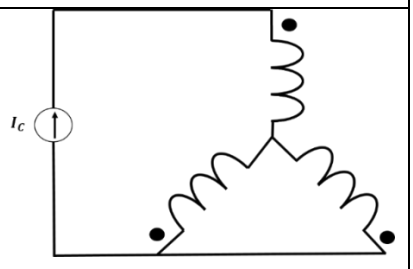
$I_1 = I_C$ $I_2 = 0$ $I_3 = 0$	$I_1 = 0$ $I_2 = I_c$ $I_3 = -I_c$	$I_1 = I_C$ $I_2 = -0.5\ I_c$ $I_3 = -0.5\ I_c$

3.8 Numerical treatments of the results of measurements

The output voltage of the force sensor is measured in function of time and displayed on a scope. Due to different reasons the delivered signal is not perfect and must be treated numerically. The numerical treatments performed for each measurement is presented by the help of an example.

Figure 3-8 gives an example of the output voltage in function of time which is the image of the torque applied on the stator.

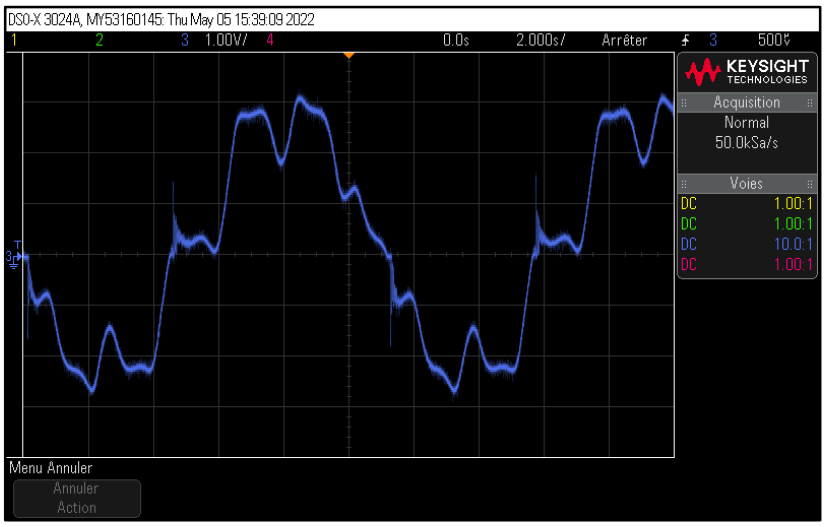

Figure 3-8: Example of the output voltage delivered by the force sensor

Figure 3-9 shows the torque applied on the rotor corresponding to the output voltage on *Figure 3-8* and according to equation (3.37).

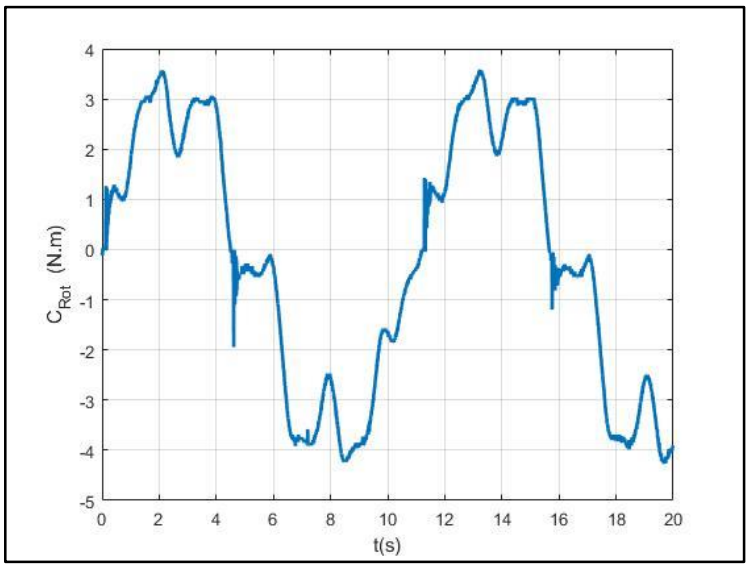

Figure 3-9: Example of the torque applied on the rotor corresponding to Figure 3-8

The first imperfection that is observed is that the measured torque has parasitic noise which should be filtered. As the sampling step δt is constant, a Moving-Average filter is used to

filter the measured signal. A window of length n_f is slided along the signal and the average of the signal within the window is calculated:

$$C_{Rot}^{f}(t_n) = \frac{1}{n_f}\sum_{i=1}^{n_f} C_{Rot}(t_n + (i-1)\delta t) \tag{3.39}$$

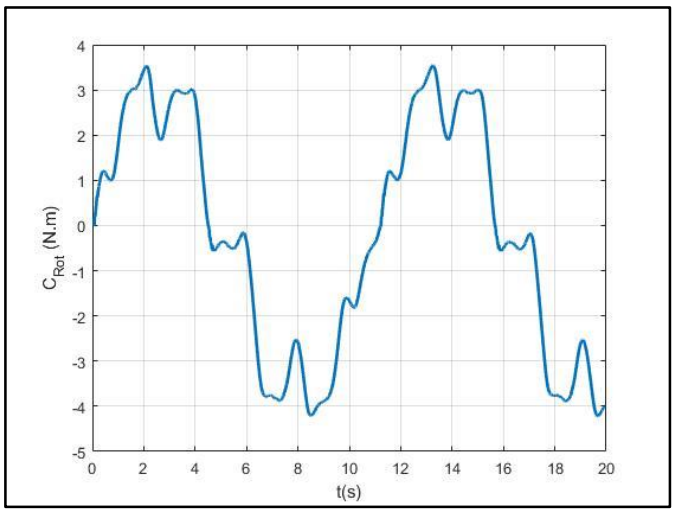

Figure 3-10: Filtered measured torque

Figure 3-10 shows the signal of the filtered measured torque. But there are imperfections left. The measured torque is not symmetric along the vertical axis: the maximal value of torque is not the opposite of the minimal value of torque. It is not also symmetric along horizontal axis: over a period, the duration of positive torque is not equal to the duration of negative torque.

Firstly, an offset is applied to put the horizontal axis at the zero torque level (*Figure 3-11*):

$$C_{Rot}^{Offset}(t_n) = C_{Rot}^{f}(t_n) - Offset \tag{3.40}$$

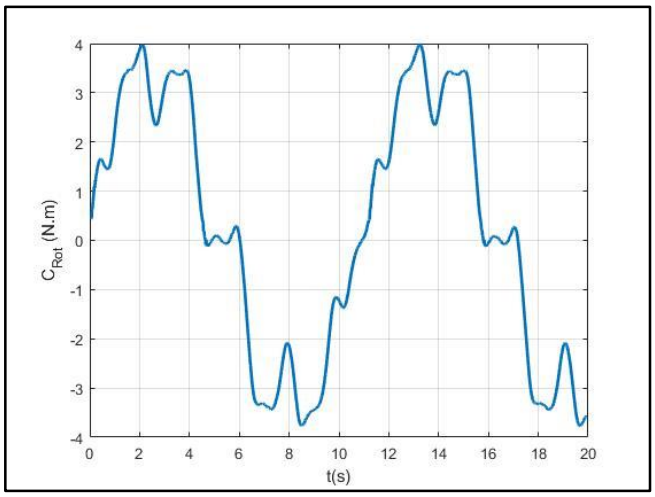

Figure 3-11: An offset is applied on the filtered measured torque

To equalize along the vertical and the horizontal axis, the symmetric of the signal versus at the point $\left(\frac{T}{2}, 0\right)$ located on the horizontal axis is calculated first:

$$C_{Rot}^{Sym}(t_n) = -C_{Rot}^{Offset}(T - t\ \ ) \tag{3.41}$$

The ultimate signal is the average of the two signals:

$$C_{Rot}^{OK}(t_n) = \frac{1}{2}\left(C_{Rot}^{Offset}(t_n) + C_{Rot}^{Sym}(t_n)\right) \tag{3.42}$$

Figure 3-12 shows the results of these last treatments.

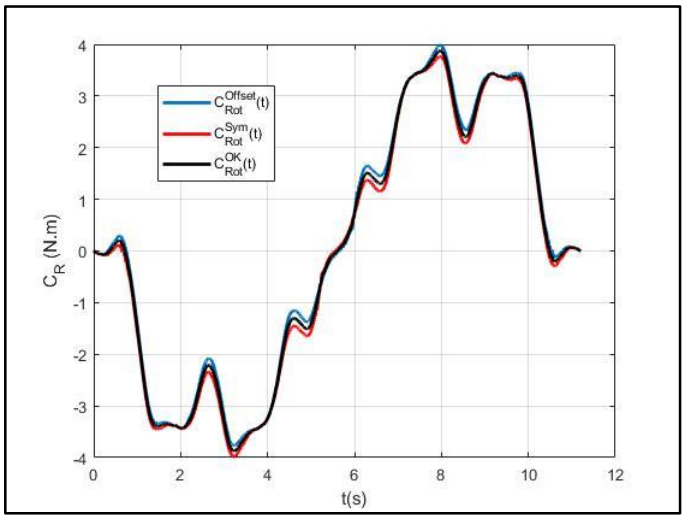

Figure 3-12: Results of the last treatment along horizontal and vertical axis

As the rotor speed is known the rotor position θ_R^m is given by:

$$\theta_R^m(t) = \Omega t$$

The torque can then be plotted in function of the rotor position (*Figure 3-13*). In the followings, all these treatments are no more presented only the ultimate result is presented.

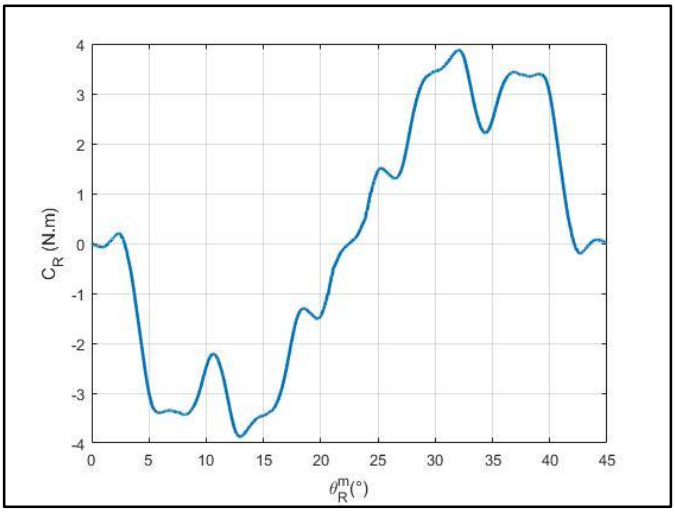

Figure 3-13: Torque over one period in function of rotor position

3.9 Static torque measurements without permanent magnets

In this section, the permanent magnets are not mounted on the rotor. It is worth to recall that on spoke-type structure, the yoke of the rotor is not ferromagnetic but is made of non-magnetic material where the ferromagnetic polar pieces are fixed. The prototype without permanent magnets on the test bench is shown in *Figure 3-14*.

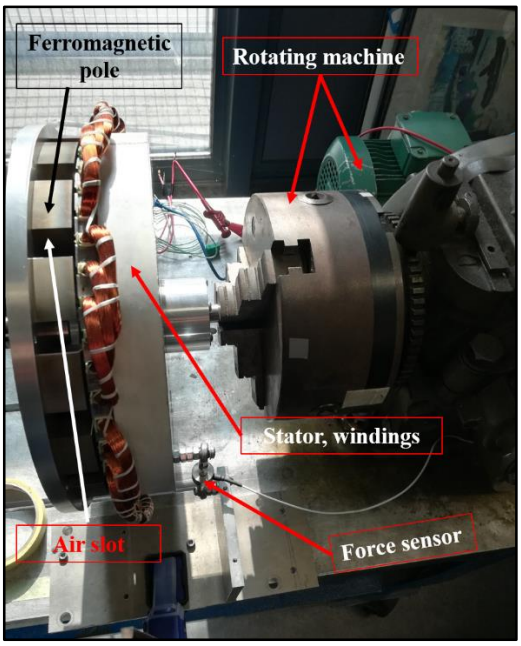

Figure 3-14: Prototype without permanent magnets on the test bench

3.9.1 First experimental observations

Without permanent magnets, when only one phase is supplied, the symmetry conditions show that the rotor has only two equilibrium positions:

- Case 1: The iron pole is facing the conductors of the supplied phase;
- Case 2: The iron pole is facing the axis of the supplied phase.

A priori one expects case (2) as the equilibrium position. The first experimental observations on the new prototype show that, when only one phase is fed, the rotor goes into a stable equilibrium position corresponding to case (1) where the iron pole is facing the conductors of the supplied phase and not as expected in the position where the iron pole is facing the phase axis. To understand these first experimental observations, a qualitative study of the torque is done by means of a 2D finite element analysis (FEA). In 2D FEA, the axial flux machine is assimilated as a linear motor. Without permanent magnets, only one phase, the phase 3 here, is supplied by a DC current I_C. The torque is calculated around the two equilibrium positions.

Study around the position: R_3 aligned with the iron pole

Figure 3-15 represents the first studied case. The study is made around the position where the iron pole is facing the R_3 'return' conductors of the supplied phase.

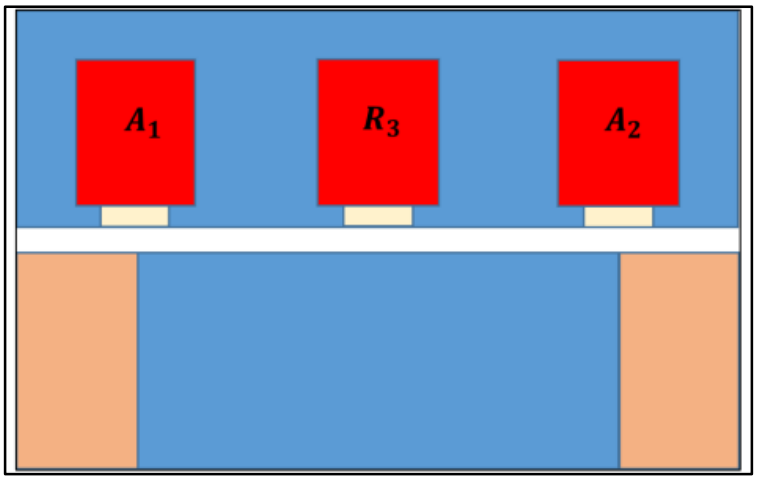

Figure 3-15: Iron pole facing the R_3 return conductors of the supplied phase (phase 3)

The electrical position of the rotor axis (D axis) is shown in *Figure 3-16*.

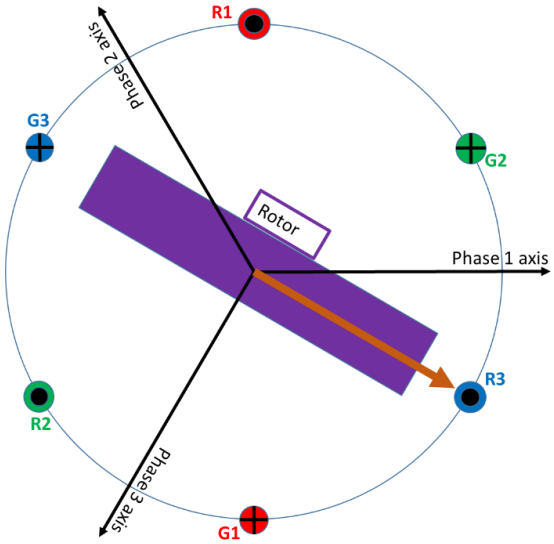

Figure 3-16: Case 1 electric domain: aligned rotor axis with the R_3 return conductors

The magnetic field lines are shown in *Figure 3-17*.

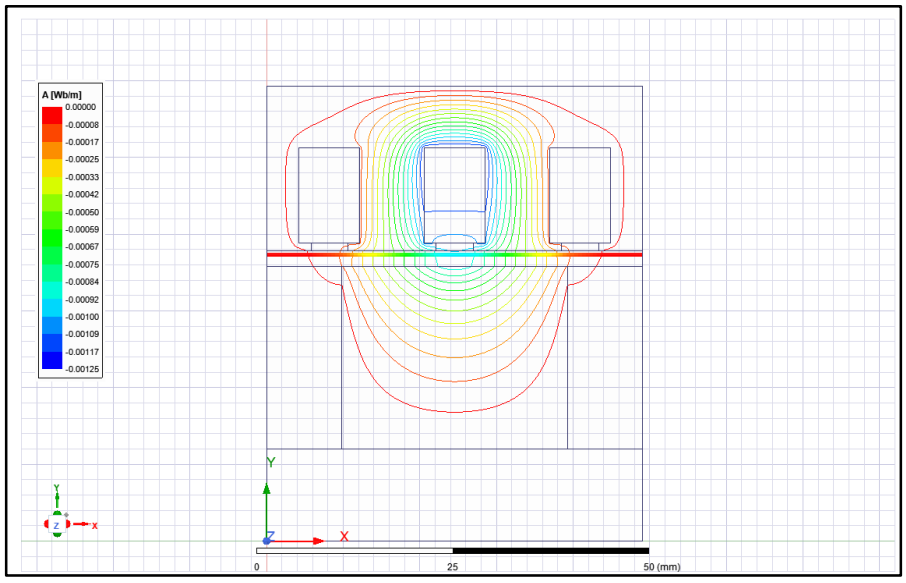

Figure 3-17: Magnetic field lines due to the DC supply of phase 3

In this case, the torque is given by:

$$C_{rot} = \frac{1}{2}\frac{\partial L_3}{\partial x} I_c^2 \qquad (3\text{-}43)$$

Figure 3-18 presents the torque variation around the studied position $(x = 0)$.

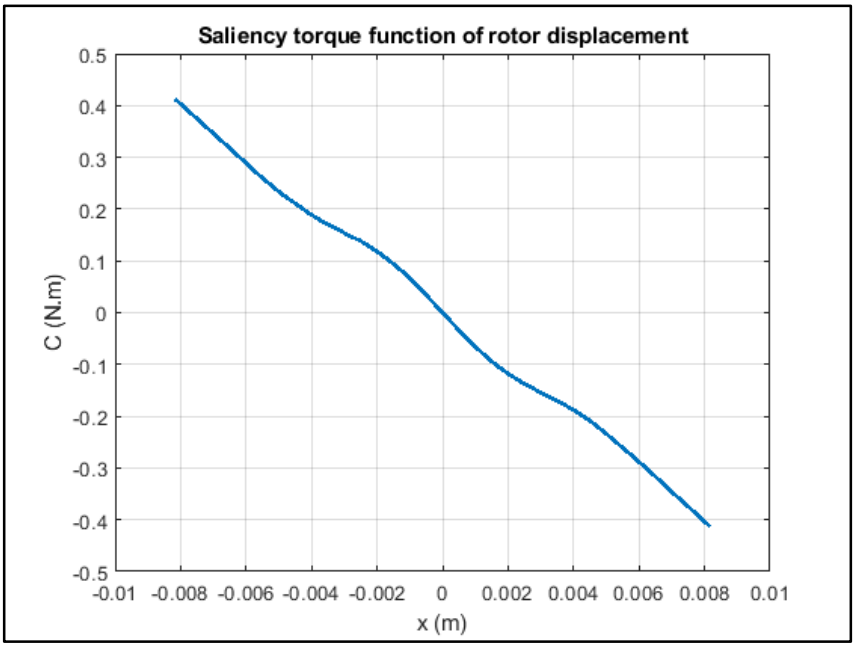

Figure 3-18: Static torque variation around the studied position for $I_c = 2.12\ A$

Figure 3-18 shows that this position is a stable equilibrium position because when the rotor is moved away from the position (x = 0) the sign of the torque shows that it brings the rotor back to this position.

Study around the position: R_3 facing the magnet

Figure 3-19 represents the second studied case. The study is made around the position where the permanent magnet is facing the return conductors R_3. Only *'phase-3'* is supplied with a direct current and permanent magnets are removed.

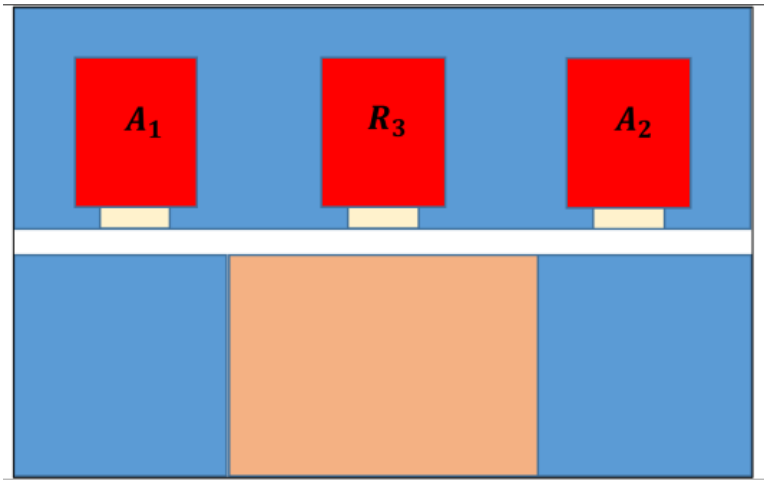

Figure 3-19: Location of permanent magnet facing the R_3 return conductors of phase 3

As the permanent magnet locations are facing the conductors of phase 3, thus the rotor axis is aligned with the phase 3 axis. Hence the electrical position of the rotor axis is shown in the electrical domain in *Figure 3-20*.

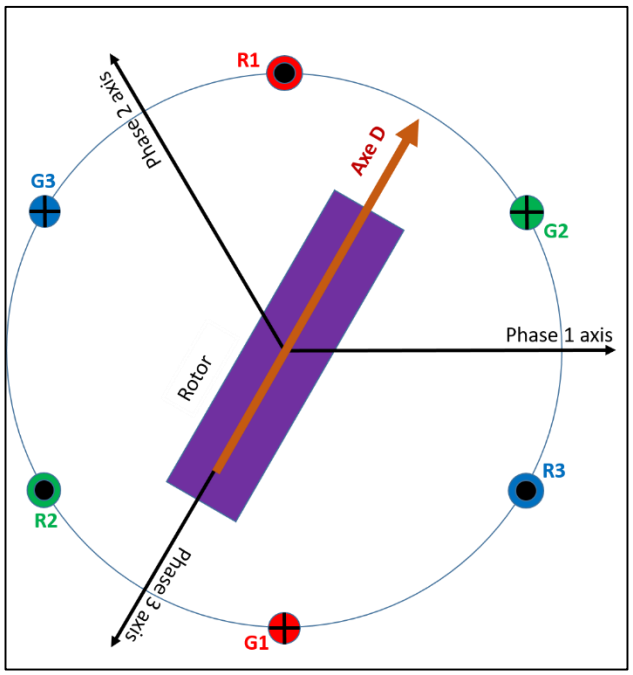

Figure 3-20: Case 2 electric domain: the rotor axis is aligned with the phase 3 axis

The magnetic field lines due to the supply of *'Phase-3'* are presented in *Figure 3-21*.

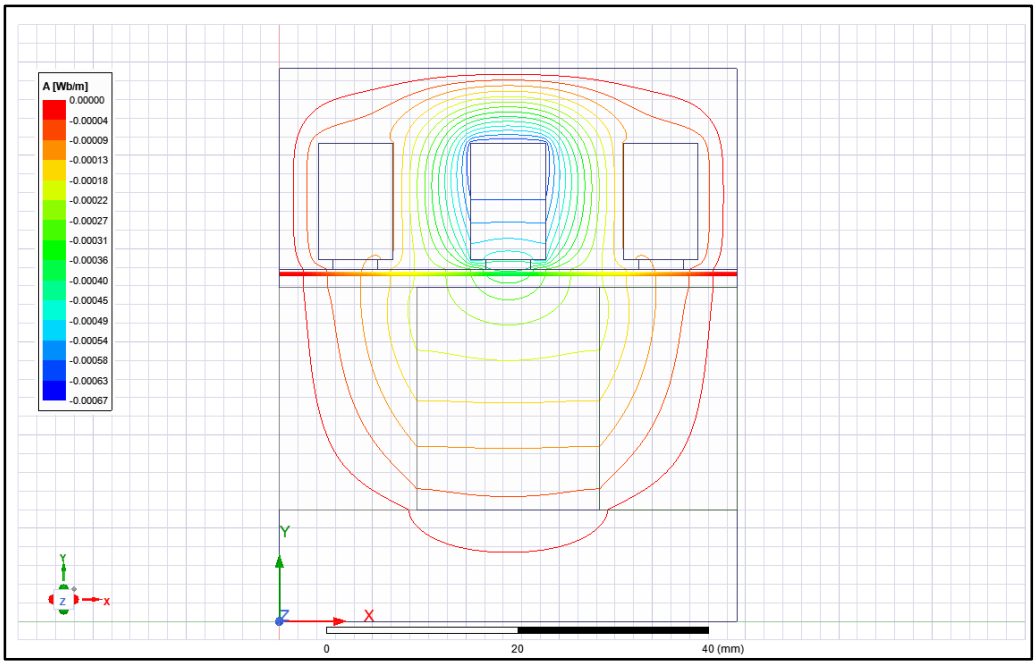

Figure 3-21: Case 2 magnetic field lines due to the DC supply of phase 3

In this case, the torque is given by:

$$C_{rot} = \frac{1}{2}\frac{\partial L_3}{\partial x} I_c^2 \qquad (3\text{-}44)$$

Figure 3-22 presents the torque variation around the studied position $(x = 0)$.

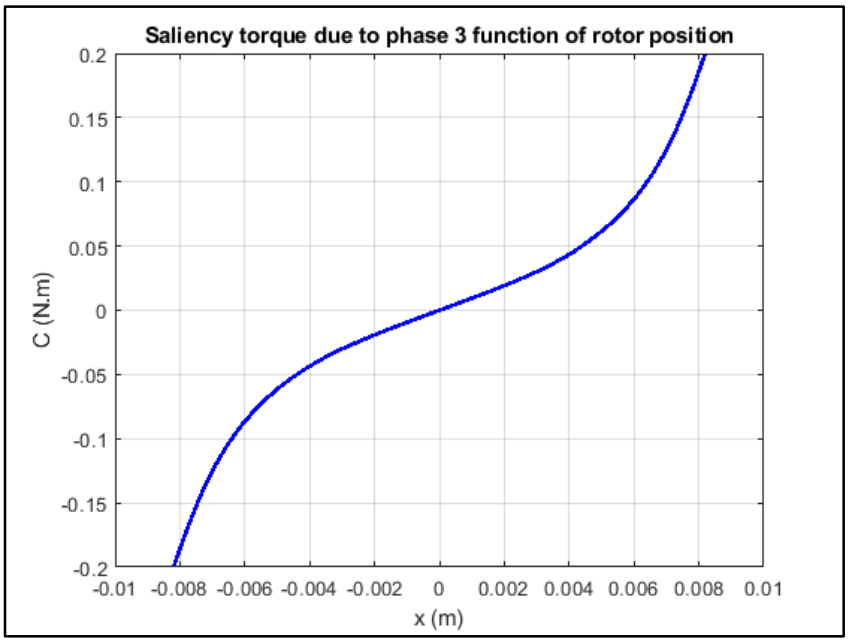

Figure 3-22: Static torque variation around the case 2 studied position for $I_c = 2.12\ A$

Figure 3-22 shows that this position is an unstable equilibrium position because when the rotor is moved away from the position $(x = 0.0\ m)$, the sign of the torque shows that it moves the rotor away from the equilibrium position.

As a conclusion, the preliminary studies shows that, when only one phase is supplied without permanent magnets, the two positions studied are equilibrium positions because the torque is null. The expected stable equilibrium position, is the position where the iron pole is facing the axis of the supplied phase. The preliminary studies demonstrate that this expected position is an unstable equilibrium position and the stable equilibrium position corresponds to the first case studied where the rotor axis is facing the conductors of the supplied phase. This fact can be explained by the fact that the rotor yoke is a non-magnetic material.

3.9.2 Single phase supply

The permanent magnets are removed. Only the first phase is fed. The phase connections and the supply currents are given on TABLE 3-I first column. The rotor is driven at a very low speed $(0.29\,rpm)$. After the numerical treatments described in section 3.8, the static torque in function of the mechanical angle θ_R^m is presented in *Figure 3-23*.

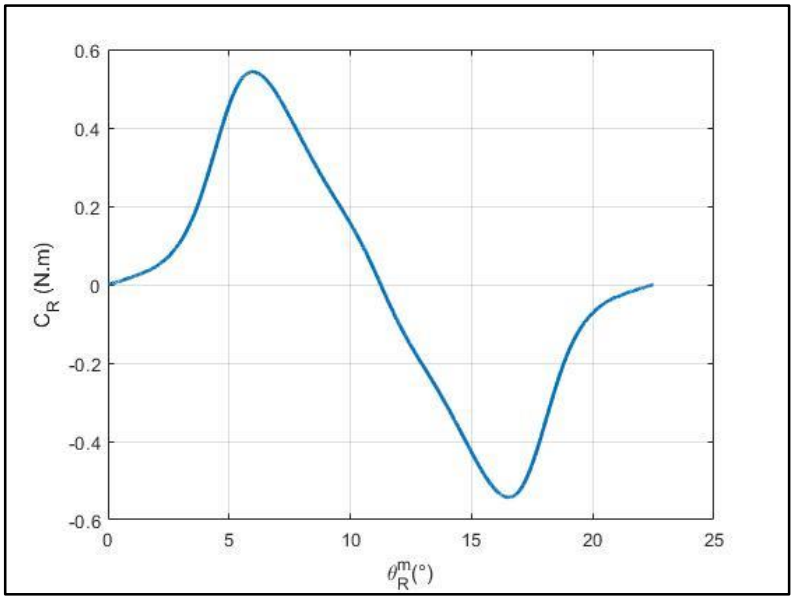

Figure 3-23: Torque in function of rotor angular position θ_R^m

At the origin $(\theta_R^m = 0°)$, in *Figure 3-23*, the axis of the rotor is facing the axis of phase 1which is the supplied phase. In reference to *Figure 3-22*, the origin is identified as the unstable equilibrium position. *Figure 3-24* shows the static torque curves without permanent magnets for different values of the current supply.

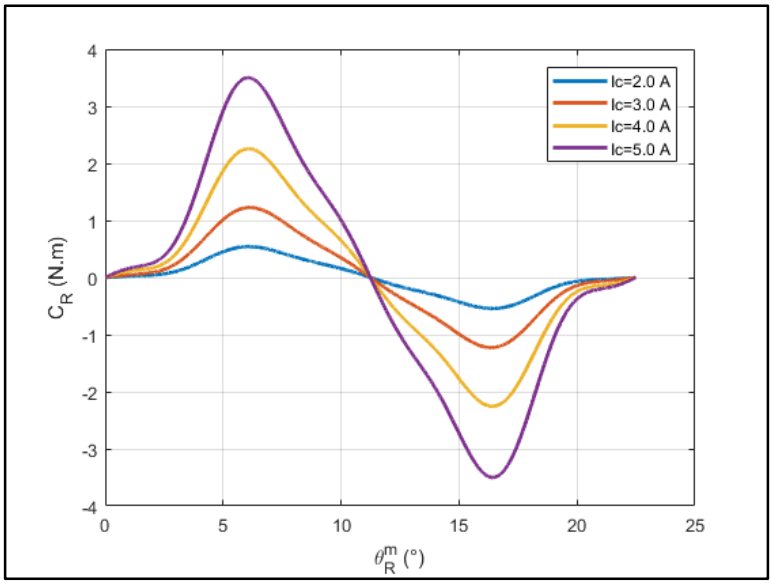

Figure 3-24: Saliency torque due to different current values

Using the electromechanical model, the derivatives of the inductance with respect to the mechanical angular position of the rotor is given by *(3.45).*

$$\frac{dL_1(\theta_R^m)}{d\theta_R^m} = \frac{2C_{R1}(\theta_R^m)}{I_c^2} \tag{3.45}$$

Figure 3-25 gives the derivatives of the self-inductance of the supplied phase for the different values of current.

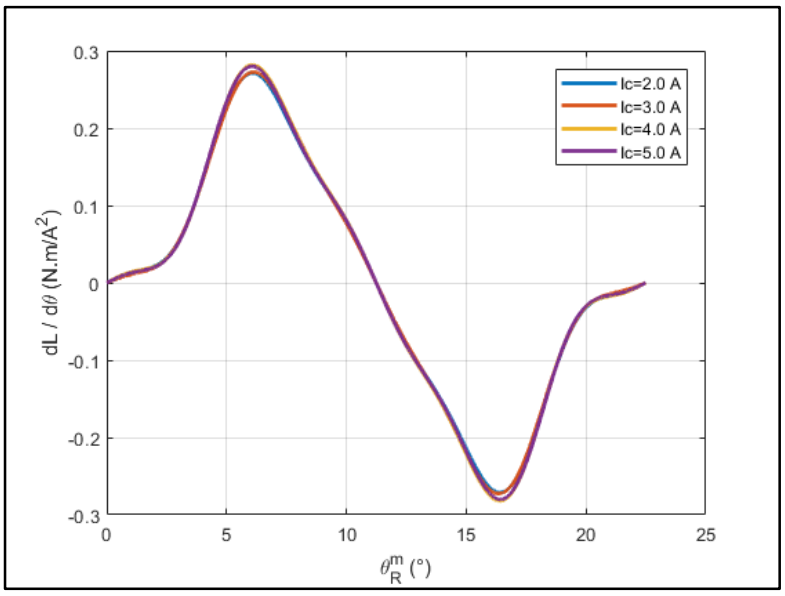

Figure 3-25: Self-inductances variations for different current values

Figure 3-25 shows that the derivative of the self-inductance as a function of the rotor position does not depend of the value of the current. This shows that, in the absence of permanent magnets, the magnetic circuit is not saturated. The torque as a function of the rotor position can be decomposed into harmonics. Taking into account the symmetry with respect to the origin and its periodicity, the torque expression can be written as in *(3.46).*

$$C_{R1}(\theta_R^m) = \sum_{n=1}^{nh} s_n \, sin(2np\theta_R^m) \qquad (3\text{-}46)$$

Table 3-II gives the values of the first five harmonics of the derivative of the inductance for different current values. The values of harmonics do not vary much with the current.

TABLE 3-II: The first five harmonics of the self-inductances derivatives

	$\frac{2}{I_c^2} s_1$	$\frac{2}{I_c^2} s_2$	$\frac{2}{I_c^2} s_3$	$\frac{2}{I_c^2} s_4$	$\frac{2}{I_c^2} s_5$
$I_c = 2A$	0.2027	-0.0564	-0.0441	0.0041	0.0160
$I_c = 3A$	0.2038	-0.0582	-0.0448	0.0054	0.0141
$I_c = 4A$	0.2084	-0.0596	-0.0494	0.0054	0.0179
$I_c = 5A$	0.2068	-0.0552	0.0501	0.0044	0.0179

The derivatives of the inductances with respect to the mechanical angular position of the rotor can be reconstructed from the harmonics *(3.47)*.

$$\frac{dL_1(\theta_R^m)}{d\theta_R^m} = \frac{2}{I_c^2} \sum_{n=1}^{nh} s_n \, sin(2np\theta_R^m) \qquad (3.47)$$

From (3.30), the harmonics of the derivative of the self-inductances are:

$$dl_n = \frac{2}{I_c^2} s_n \qquad (3.48)$$

Figure 3-26 shows the reconstruction of the derivative of the self-inductance of each phase from (3.30) and (3.48).

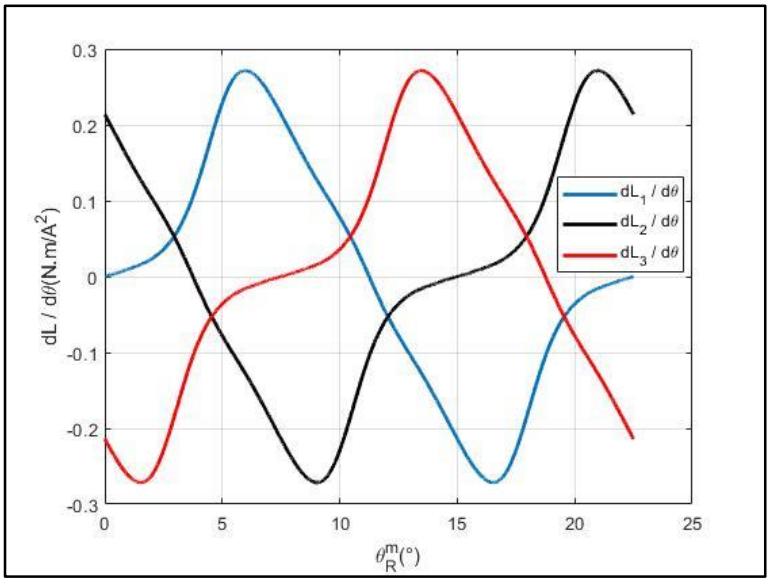

Figure 3-26: Derivatives of the self-inductances reconstituted from harmonics

3.9.3 Double phase supply

The permanent magnets are removed. Only phase 2 and phase 3 are fed. The phase connections and the supply currents are given on TABLE 3-I 2nd column. The rotor is driven at a very low speed $(0.29\ rpm)$. After the numerical treatments described in section 3.8, the static torque in function of the mechanical angle θ_R^m is presented in *Figure 3-27*.

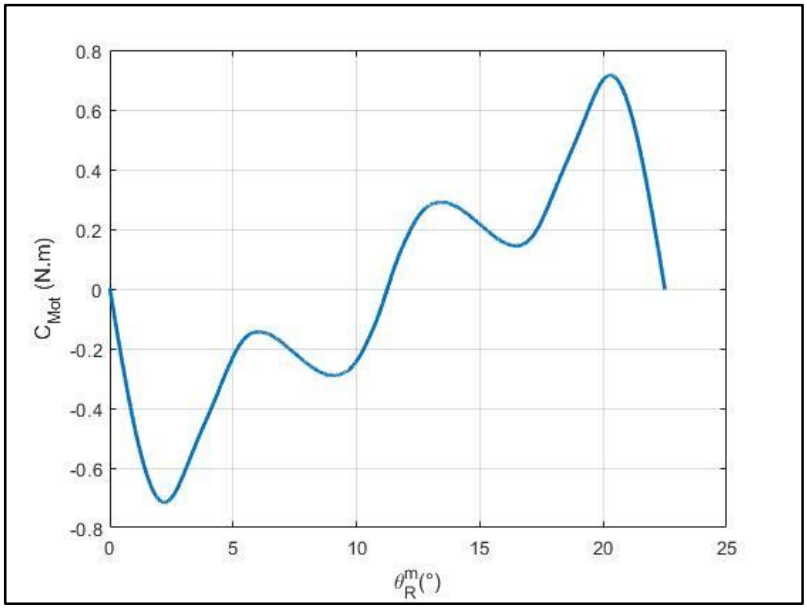

Figure 3-27: Static torque without permanent magnet and double phase supply

From *Figure 3-27* it can be noticed that, at the origin, the rotor is in the stable equilibrium position. This initial position corresponds to the rotor position in the electrical domain shown in *Figure 3-28* where it is aligned with *'phase-1'* axis.

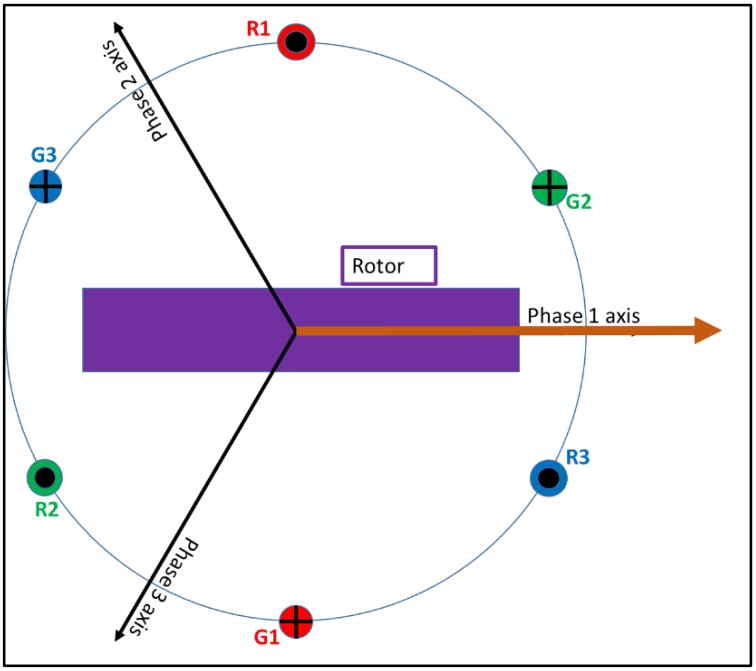

Figure 3-28: Electric domain the rotor axis is aligned with the phase 1 axis

This is a stable equilibrium position if phases 2 and 3 are supplied in anti-series.

$$\begin{cases} I_1 = 0 \\ I_2 = I_C \\ I_3 = -I_C \end{cases} \qquad (3\text{-}49)$$

Indeed, in this case, the ferromagnetic polar pieces are facing the conductors of the active phases. *Figure 3-29* presents the static torque curves without permanent magnets and with double phase supply for DC current of 2 *A* and 3 *A* respectively.

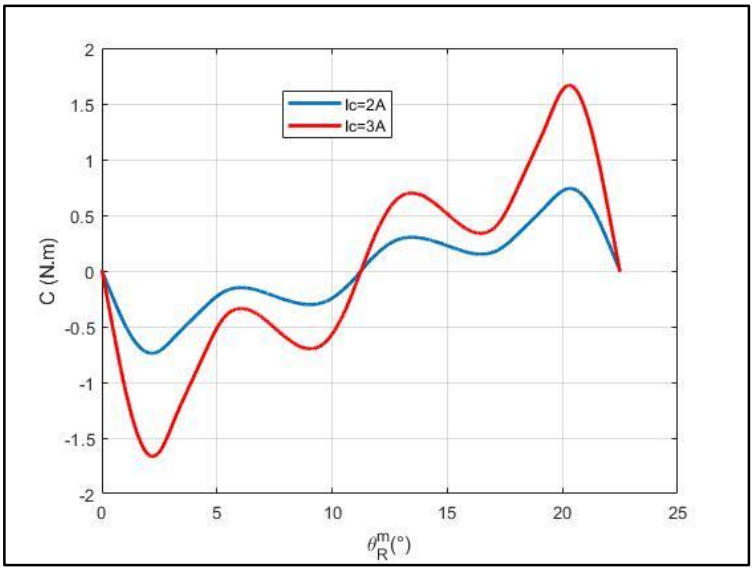

Figure 3-29: Static torques for double phase supply for two different values of the current

Using the electromechanical model, the torque is expressed by:

$$C_{R23}(\theta_R^m) = \frac{1}{2}\left(\frac{dL_2(\theta_R^m)}{d\theta_R^m} + \frac{dL_3(\theta_R^m)}{d\theta_R^m} - 2\frac{dM_1(\theta_R^m)}{d\theta_R^m}\right) I_c^2 \qquad (3\text{-}50)$$

Figure 3-30 presents $\frac{2C_{R23}(\theta_R^m)}{I_c^2}$ for two values of the supply currents. Indeed, it shows that the current has a very few effect on the obtained results. The torque as a function of the rotor position θ_R^m can be expressed in terms of its harmonics.

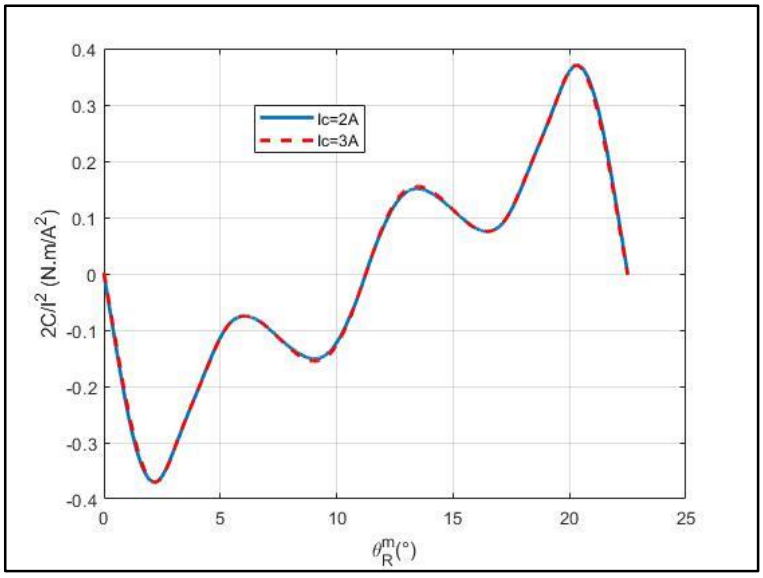

Figure 3-30: $\frac{2C_{R23}(\theta_R^m)}{I_c^2}$ *for two different values of current*

Given the symmetry with respect to the origin and its periodicity, the torque expression can be written by *(3.51)*.

$$C_{R23}(\theta_R^m) = \sum_{n=1}^{nh} sa_n \, sin(2np\theta_R^m) \qquad (3\text{-}51)$$

TABLE 3-III gives the values of the first five harmonics of $\frac{2C_{R23}(\theta_R^m)}{I_c^2}$ for the two values of current. The values of harmonics do not vary much with the supply current.

TABLE 3-III: The first five harmonics of $\frac{2C_{R23}(\theta_R^m)}{I_c^2}$ *for 2.0 and 3.0 A*

	$\frac{2}{I_c^2} sa_1$	$\frac{2}{I_c^2} sa_2$	$\frac{2}{I_c^2} sa_3$	$\frac{2}{I_c^2} sa_4$	$\frac{2}{I_c^2} sa_5$
$I_c = 2A$	-0.2123	-0.0958	-0.1400	-0.0232	-0.0116
$I_c = 3A$	-0.2128	-0.0933	-0.1401	-0.0205	-0.0104

The derivative of the mutual inductance between phase 2 and phase 3 is given by *(3.52)*.

$$\frac{dM_1(\theta_R^m)}{d\theta_R^m} = \frac{dL_{23}(\theta_R^m)}{d\theta_R^m} = \frac{1}{2}\left(\frac{dL_2(\theta_R^m)}{d\theta_R^m} + \frac{dL_3(\theta_R^m)}{d\theta_R^m} - 2\frac{C_{R23}(\theta_R^m)}{I_c^2}\right) \qquad (3\text{-}52)$$

The derivatives of the self-inductances can be expressed in terms of the harmonics s_n of the static torques due to one phase C_{Rk} as written in *(3.53)*.

$$\begin{cases} \frac{dL_2(\theta_R^m)}{d\theta_R^m} = 2\frac{C_{R2}(\theta_R^m)}{I_c^2} = \frac{2}{I_c^2}\sum_{n=1}^{nh} s_n \, sin\left(2n\left(p\theta_R^m - \frac{2\pi}{3}\right)\right) \\ \frac{dL_3(\theta_R^m)}{d\theta_R^m} = 2\frac{C_{R3}(\theta_R^m)}{I_c^2} = \frac{2}{I_c^2}\sum_{n=1}^{nh} s_n \, sin\left(2n\left(p\theta_R^m - \frac{4\pi}{3}\right)\right) \end{cases} \qquad (3\text{-}53)$$

Then,

$$\frac{dL_2(\theta_R^m)}{d\theta_R^m} + \frac{dL_3(\theta_R^m)}{d\theta_R^m} = \frac{2}{I_c^2}\sum_{n=1}^{nh} s_n \left(sin\left(2np\theta_R^m - n\frac{2\pi}{3}\right) + sin\left(2np\theta_R^m - n\frac{4\pi}{3}\right)\right) \quad (3.54)$$

It can be written as:

$$\frac{dL_2(\theta_R^m)}{d\theta_R^m} + \frac{dL_3(\theta_R^m)}{d\theta_R^m} = \frac{2}{I_c^2}\sum_{n=1}^{nh} s_n \left(sin\left(2np\theta_R^m - n\frac{2\pi}{3}\right) + sin\left(2np\theta_R^m + n\frac{2\pi}{3}\right)\right) \quad (3.55)$$

Hence:

$$\frac{dL_2(\theta_R^m)}{d\theta_R^m} + \frac{dL_3(\theta_R^m)}{d\theta_R^m} = \frac{4}{I_c^2}\sum_{n=1}^{nh} s_n \sin(2np\theta_R^m)\cos\left(n\frac{2\pi}{3}\right) \quad (3.56)$$

The derivative of the mutual inductance is then given by:

$$\frac{dM_1(\theta_R^m)}{d\theta_R^m} = \frac{1}{2}\left(\frac{4}{I_c^2}\sum_{n=1}^{nh} s_n\, sin(2np\theta_R^m)\, cos\left(n\frac{2\pi}{3}\right) - \frac{2}{I_c^2}\sum_{n=1}^{nh} sa_n\, sin(2np\theta_R^m)\right) \quad (3.57)$$

The final expressions can be written in the following form and extended to all mutual:

$$\frac{dM_k(\theta_R^m)}{d\theta_R^m} = \frac{1}{I_c^2}\sum_{n=1}^{nh}\left(2s_n\, cos\left(n\frac{2\pi}{3}\right) - sa_n\right) sin\left(2n\left(p\theta_R^m - (k-1)\frac{2\pi}{3}\right)\right) \quad (3.58a)$$

From (3.58a), the harmonics of the derivative of the mutual inductances are:

$$dm_n = \frac{2}{I_c^2}\left(2s_n\, cos\left(n\frac{2\pi}{3}\right) - sa_n\right) \quad (3.58b)$$

Now, as the derivatives regarding the self and mutual inductances variations are written in function of the harmonics of the single phase static torque *(3.45)* and the harmonics of the double phase static torque (3.52), the derivative of the matrix inductance is identified:

$$\frac{d\boldsymbol{L}(\theta_R^m)}{d\theta_R^m} = \begin{bmatrix} \frac{dL_1(\theta_R^m)}{d\theta_R^m} & \frac{dM_3(\theta_R^m)}{d\theta_R^m} & \frac{dM_2(\theta_R^m)}{d\theta_R^m} \\ \frac{dM_3(\theta_R^m)}{d\theta_R^m} & \frac{dL_2(\theta_R^m)}{d\theta_R^m} & \frac{dM_1(\theta_R^m)}{d\theta_R^m} \\ \frac{dM_2(\theta_R^m)}{d\theta_R^m} & \frac{dM_1(\theta_R^m)}{d\theta_R^m} & \frac{dL_3(\theta_R^m)}{d\theta_R^m} \end{bmatrix} \quad \textit{(3-59)}$$

3.9.4 Conclusion of the tests without permanent magnets

The tests without permanent magnets allow to measure the static torque of single phase or double phase supply in function of the position of the rotor. These two static torques allow to identify the harmonics of the derivatives of self and mutual inductances. These are the parameters of the torque model that allow to calculate the saliency torque in function of the rotor position and the current in each phase. These parameters are validated in section 3.11.

3.10 Measurements with permanent magnets

3.10.1 Cogging torque

When the permanent magnets are mounted on the rotor and the currents are null, the measured torque is the so known cogging torque. After the numerical treatments, the obtained cogging torque is presented in *Figure 3-31*.

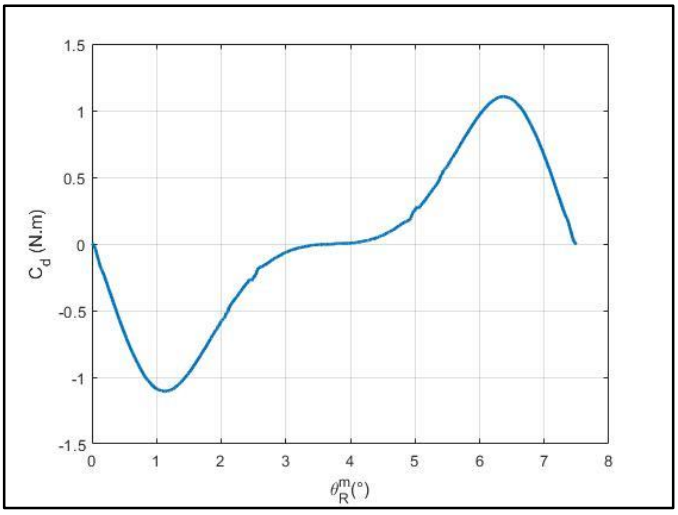

Figure 3-31: The measured cogging torque

The period of the cogging torque is equal to one tooth pitch, thus the expression of the cogging torque as a function of the angular position of the rotor is given by *(3-60).*

$$C_d(\theta_R^m) = \sum_{n=1}^{nh} sd_n \, sin(nn_e\theta_R^m) \qquad (3\text{-}60)$$

Where sd_n is the cogging torque harmonics of rank n, n_e is the number of slots. Indeed, at the horizontal axis origin, due the definition of θ_R^m, the rotor axis is facing a tooth. The origin is a stable equilibrium position. *Figure 3-32* presents the reconstruction of the cogging torque with the first 5 harmonics.

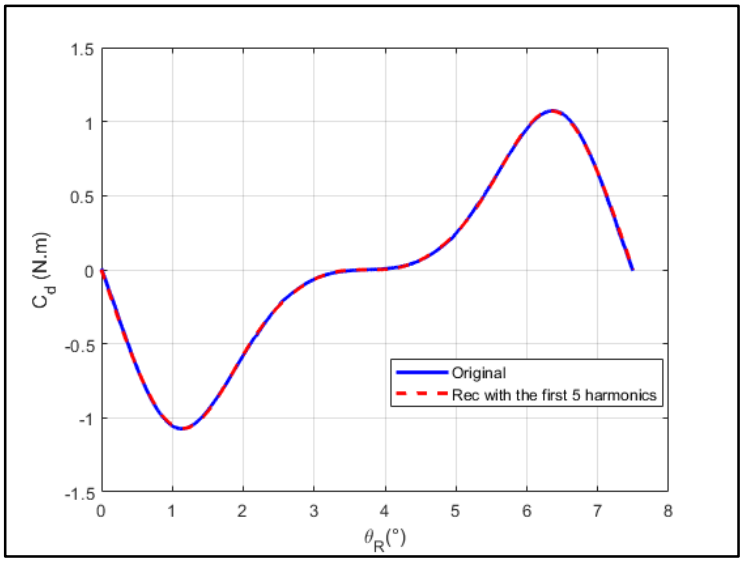

Figure 3-32: Original and reconstituted cogging torques

Table 3-IV gives the values of the first five harmonics sd_n of $C_d(\theta_R^m)$.

TABLE 3-IV: The first five harmonics of $C_d(\theta_R^m)$

sd_1	sd_2	sd_3	sd_4	sd_5
-0.7418	-0.4526	-0.0527	0.0176	0.0135

3.10.2 Derivative of the no-load flux

The permanent magnets are mounted on the rotor and the currents are null. The rotor is driven by another motor at a speed of 400 rpm. The measured voltages at the terminals of each phase are the no-load back electromotive force (e.m.f). The three measured no-load e.m.f. are presented in *Figure 3-33*. The peak value of each is $V_{peak} = 152\ V$.

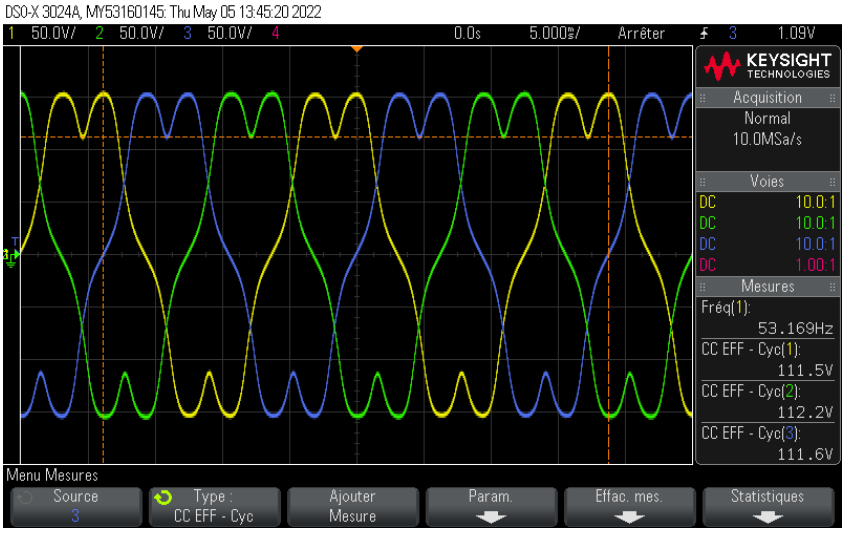

Figure 3-33: Measured e.m.f at rotational speed 400 rpm

The derivatives of the no-load fluxes with respect to the rotor position θ_R^m can be obtained from (3.26) shown in *Figure 3-34* in function of the rotor position.

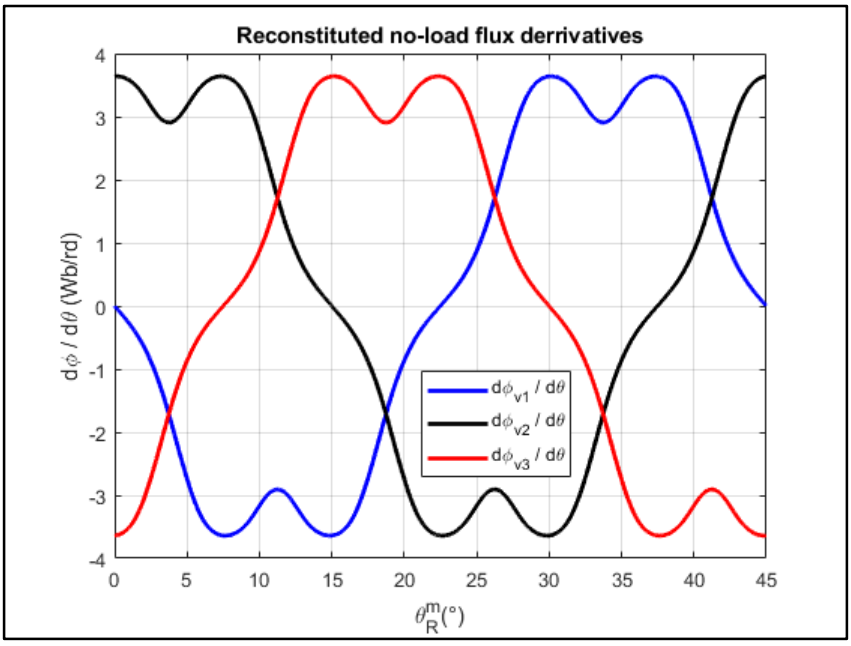

Figure 3-34: No-load fluxes derivatives function of rotor position

The period of the flux derivative is equal to one pair of poles. The expression for the no-load flux derivatives in terms of its harmonics as a function of rotor position is given in *(3-28). Figure 3-35* presents the reconstruction of the derivative of the 'phase-1' flux from the first 11 harmonics.

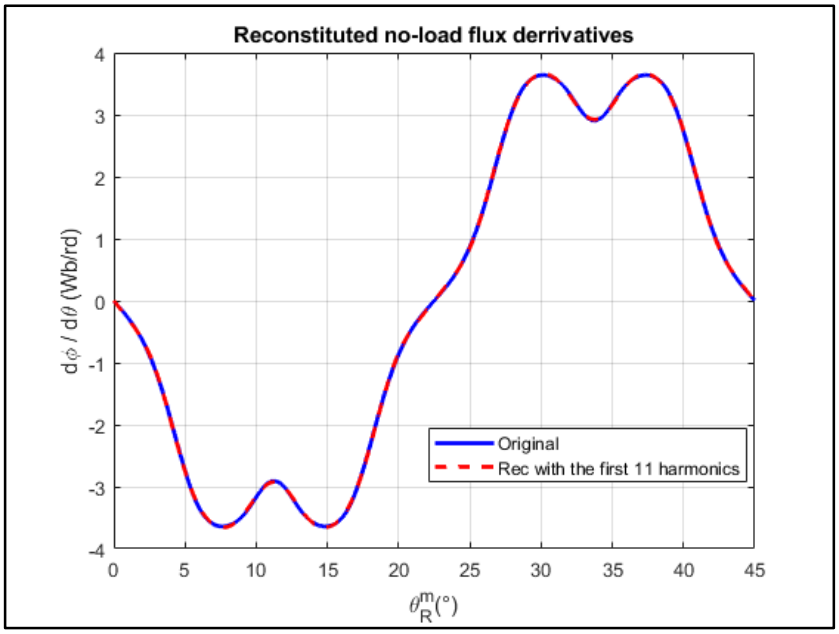

Figure 3-35: No-load fluxes derivatives reconstitution from its harmonics

Table 3-V gives the values of the first eleven harmonics df_n of $\frac{d\phi_{vk}}{d\theta_R^m}(\theta_R)$.

TABLE 3-V: The first eleven harmonics of $\frac{d\phi_{vk}}{d\theta_R^m}(\theta_R^m)$

df_1	df_2	df_3	df_4	df_5	df_6	df_7	df_8	df_9	df_{10}	df_{11}
-3.7012	-0.0031	-0.1698	-0.0023	-0.5455	0.0	-0.0155	0.0	0.0025	0.0	-0.0452

3.10.3 Conclusion

With the permanent magnets mounted on the rotor and null currents, the tests allow to determine the harmonics of the cogging torque and the no-load fluxes. These harmonics constitutes the parameters of the torque model that allows to calculate the electromagnetic torque and the cogging torque in function of the rotor position and the current in each phase. Now all the parameters of the torque model are identified. These identified parameters are validated in section 3.11.

3.11 Validation of the identified torque model parameters

3.11.1 Without permanent magnets and three phase supply

The permanent magnets are removed. The three phases are fed by DC currents. The phase connections and the supply currents are given on TABLE 3-I 3rd column. To validate the identified parameters that allow to calculate the saliency torque, the torque is measured on the test bench and calculated from the saliency torque model for two different values of the DC current. The saliency model applied to the test is given by (3.61):

$$C_R(\theta_R^m) = \frac{1}{2}\left\{I_C \quad -\frac{I_C}{2} \quad -\frac{I_C}{2}\right\}\begin{bmatrix} \frac{dL_1(\theta_R^m)}{d\theta_R^m} & \frac{dM_3(\theta_R^m)}{d\theta_R^m} & \frac{dM_2(\theta_R^m)}{d\theta_R^m} \\ \frac{dM_3(\theta_R^m)}{d\theta_R^m} & \frac{dL_2(\theta_R^m)}{d\theta_R^m} & \frac{dM_1(\theta_R^m)}{d\theta_R^m} \\ \frac{dM_2(\theta_R^m)}{d\theta_R^m} & \frac{dM_1(\theta_R^m)}{d\theta_R^m} & \frac{dL_3(\theta_R^m)}{d\theta_R^m} \end{bmatrix}\begin{Bmatrix} I_C \\ -\frac{1}{2}I_C \\ -\frac{1}{2}I_C \end{Bmatrix} \tag{3.61}$$

The derivatives of the self and mutual inductances are calculated by their harmonics using (3.31), (3.47) and (3.58). These harmonics are identified using single phase and double phase supplies with a current value of 2A.

For $I_C = 2A$, the measured and calculated torques for a three phase supply are presented on *Figure 3.36*.

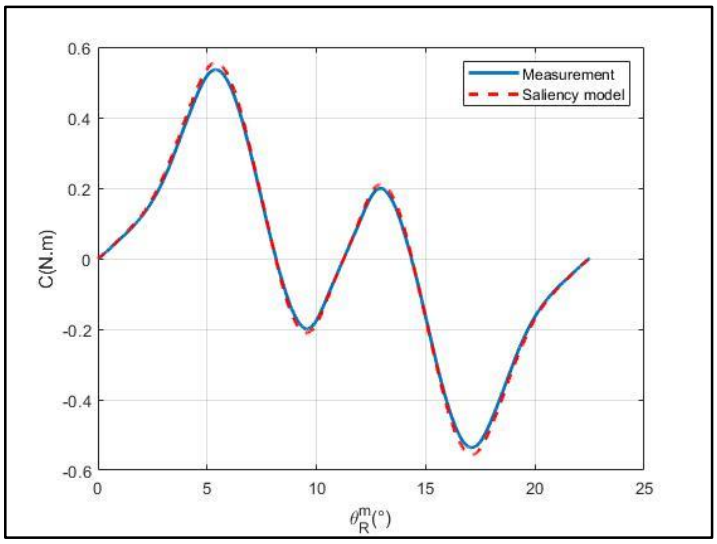

Figure 3-36: Measured and calculated saliency torque for $I_C = 2A$

Figure 3.36 shows that the calculated torque form the saliency model are in a very good accordance with the measured torque. This validates the identified parameters but also the numerical treatments applied on the measured torques.

For $I_C = 4A$, the measured torque and the calculated torque are presented on *Figure 3.37*.

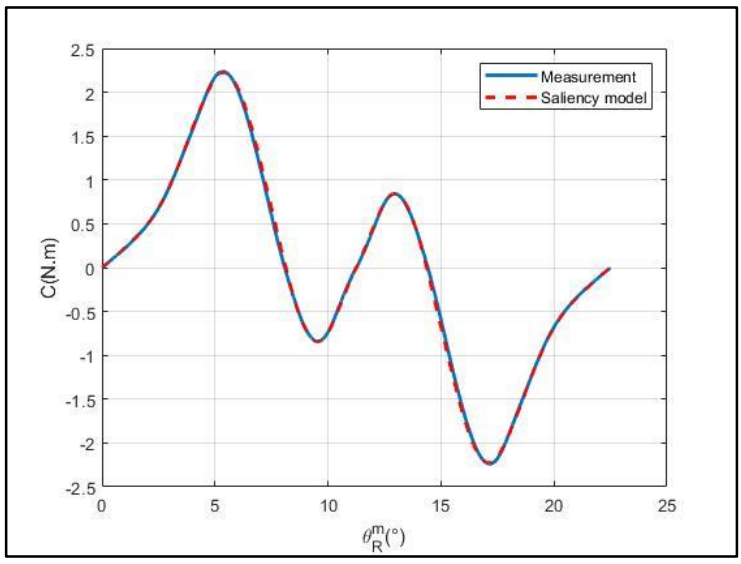

Figure 3-37: Measured and calculated saliency torque for $I_C = 4A$

When the current is doubled the saliency model still gives very good results even if the parameters where identified during tests with a supply current of 2A.

3.11.2 With permanent magnets and single phase supply

The permanent magnets are mounted on the rotor. Only the first phase is fed. The phase connections and the supply currents are given on TABLE 3-I first column. To validate the identified parameters that allow to calculate the saliency torque, the electromagnetic torque and the detent torque, the torque is measured on the test bench and calculated from the torque model for a single phase supply. The torque model applied to the test is given by (3.62)

$$C_R(\theta_R^m) = C_d(\theta_R^m) + \{I_C \quad 0 \quad 0\}\begin{Bmatrix} \frac{d\phi_{v1}}{d\theta_R^m}(\theta_R^m) \\ \frac{d\phi_{v2}}{d\theta_R^m}(\theta_R^m) \\ \frac{d\phi_{v3}}{d\theta_R^m}(\theta_R^m) \end{Bmatrix} + \frac{1}{2}\{I_C \quad 0 \quad 0\}\frac{d\boldsymbol{L}(\theta_R^m)}{d\theta_R^m}\begin{Bmatrix} I_C \\ 0 \\ -0 \end{Bmatrix} \tag{3.62}$$

By developing the matrix products, the torque for a single phase supply is given by:

$$C_R(\theta_R^m) = C_d(\theta_R^m) + I_C\frac{d\phi_{v1}}{d\theta_R^m}(\theta_R^m) + \frac{1}{2}\frac{dL_1(\theta_R^m)}{d\theta_R^m}I_c^2 \tag{3.63}$$

For $I_C = 0.6A$, the measured and calculated torques are presented on *Figure 3.38* and for $I_C = 1.0A$, on *Figure 3.39.*

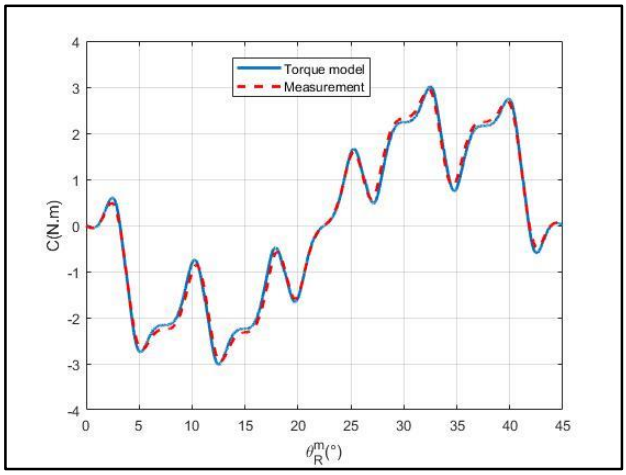

Figure 3-38: Single phase supply: measured and calculated torques for $I_C = 0.6A$

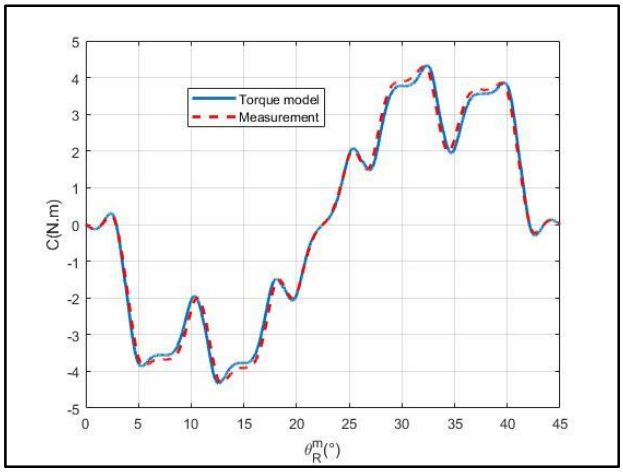

Figure 3-39: Single phase supply: measured and calculated torques for $I_C = 1.0A$

Figure 3.38 and *Figure 3.39* show that the static torque, for low current, has relatively large ripples but the torque model succeeds in reproducing them with a very good fidelity.
For $I_C = 3.6A$, the measured and calculated torques are presented on *Figure 3.40.*

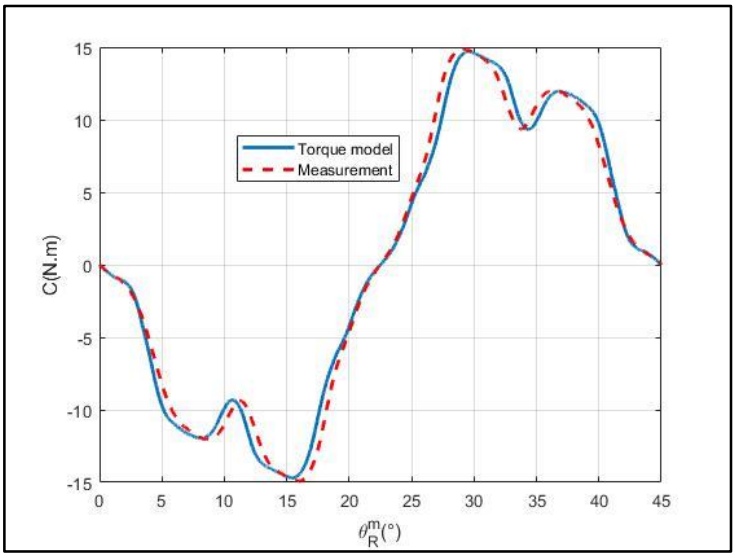

Figure 3-40: Single phase supply: measured and calculated torques for $I_C = 3.6\ A$

Figure 3.40 shows that the static torque, for higher current, has relatively less ripples. The torque model result presents relatively more differences with the measurement result but the calculated torque is still acceptable.

3.11.3 With permanent magnets and double phase supply

The permanent magnets are mounted on the rotor. Only the second and third phases are fed. The phase connections and the supply currents are given on TABLE 3-I second column. To validate the identified parameters, the torque is measured on the test bench and calculated from the torque model for a double phase supply. The torque for a double phase supply is given by (3.62):

$$C_R(\theta_R^m) = C_d(\theta_R^m) + I_C\left(\frac{d\phi_{v2}}{d\theta_R^m}(\theta_R^m) - \frac{d\phi_{v3}}{d\theta_R^m}(\theta_R^m)\right) + \frac{1}{2}\left(\frac{dL_2(\theta_R^m)}{d\theta_R^m} + \frac{dL_3(\theta_R^m)}{d\theta_R^m} - 2\frac{dM_1(\theta_R^m)}{d\theta_R^m}\right)I_c^2 \quad (3.62)$$

For $I_C = 1.0A$, the measured torque and the calculated torque are presented on *Figure 3.41* and for $I_C = 2.0A$, on *Figure 3.42*.

Figure 3.41 and *Figure 3.42* show that the torque model produce results that are still acceptable compared to the measured torque.

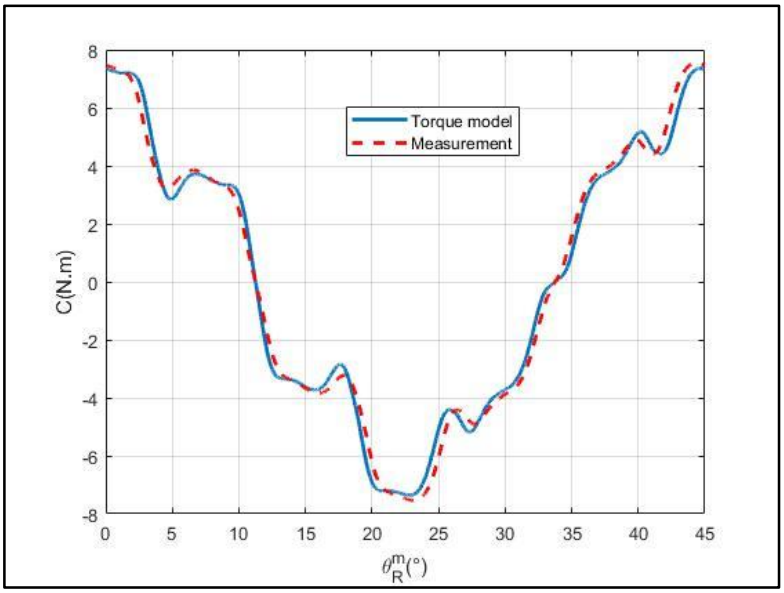

Figure 3-41: Double phase supply: measured and calculated torques for $I_C = 1.0\ A$

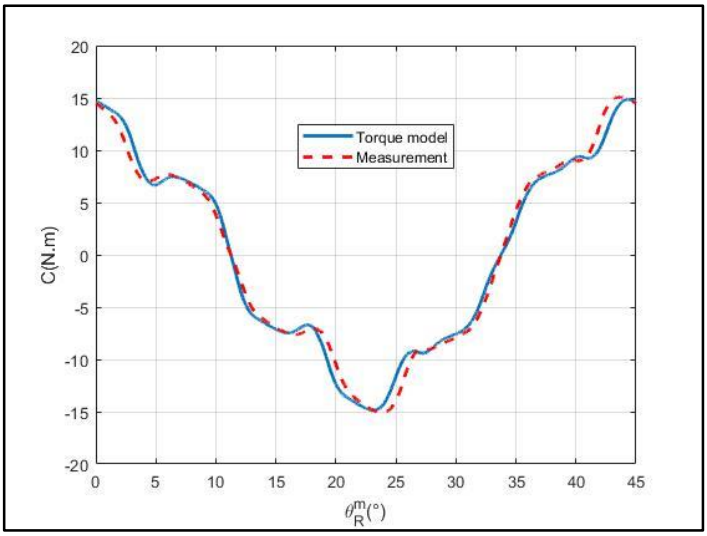

Figure 3-42: Double phase supply: measured and calculated torques for $I_C = 2.0\ A$

3.11.4 With permanent magnets and three phase supply

The permanent magnets are mounted on the rotor. The three phases are fed. The phase connections and the supply currents are given on TABLE 3-I third column. To validate the identified parameters, the torque is measured on the test bench and calculated from the torque

model for a three phase supply. The expression is left in matrix form because for a three phase supply the development may be very long (3.63):

$$C_R(\theta_R^m) = C_d(\theta_R^m) + \left\{I_C \quad -\frac{I_C}{2} \quad -\frac{I_C}{2}\right\}\begin{Bmatrix}\frac{d\phi_{v1}}{d\theta_R^m}(\theta_R^m)\\ \frac{d\phi_{v2}}{d\theta_R^m}(\theta_R^m)\\ \frac{d\phi_{v3}}{d\theta_R^m}(\theta_R^m)\end{Bmatrix} + \frac{1}{2}\left\{I_C \quad -\frac{I_C}{2} \quad -\frac{I_C}{2}\right\}\frac{d\boldsymbol{L}(\theta_R^m)}{d\theta_R^m}\begin{Bmatrix}I_C\\ -\frac{I_C}{2}\\ -\frac{I_C}{2}\end{Bmatrix} \quad (3.63)$$

For $I_C = 0.6A$, the measured calculated torques are presented on *Figure 3.43* and for $I_C = 2.6A$, on *Figure 3.44*.

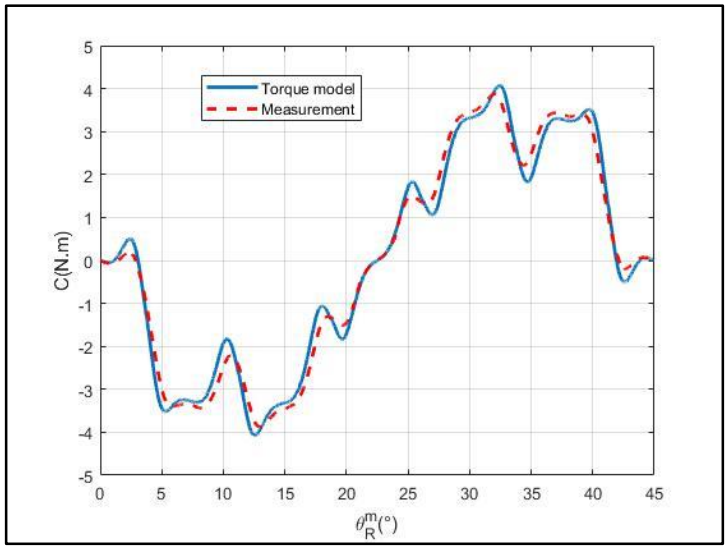

Figure 3-43: Three phase supply: measured and calculated torques for $I_C = 0.6A$

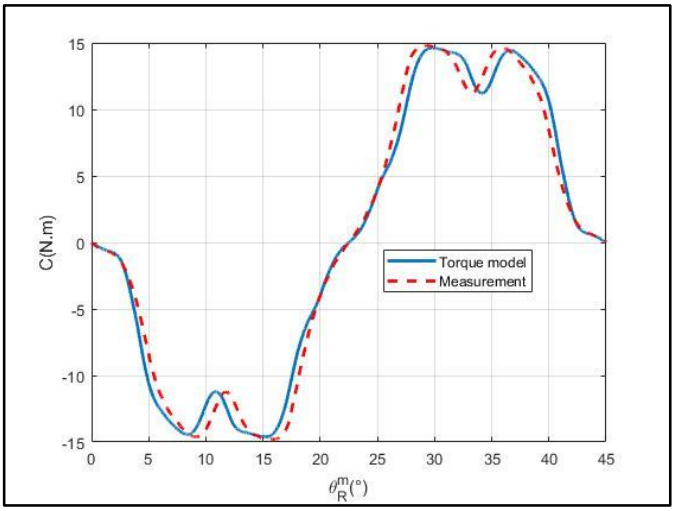

Figure 3-44: Three phase supply: measured and calculated torque for $I_C = 2.6A$

Figure 3.43 and *Figure 3.44* are the last measurements that validate the torque model and the proposed numerical treatment of experimental results. The three phase supply for $I_C = 2.6A$ can be assimilated to a point of a three phase sinusoidal supply with a r.m.s value of current equal to $I_{rms} = 1.84A$ which is higher than the rated value of current given in chapter two of $I_{rms} = 1.5A$.

3.12 Electrical measurements

The parameters of the torque model are identified by static torque measurements and the back e.m.f measurements. The identified parameters are validated in the previous section. In this section the flux model parameters, defined in section 3.6, are identified.

3.12.1 No-load flux

The harmonics df_n of the no-load flux derivatives (3.28) has been identified by e.m.f measurements in section 3.10.2. The harmonics f_n of the no-load flux (3.13) are given by (3.29). *Figure 3-45* shows the no-load flux obtained from its harmonics.

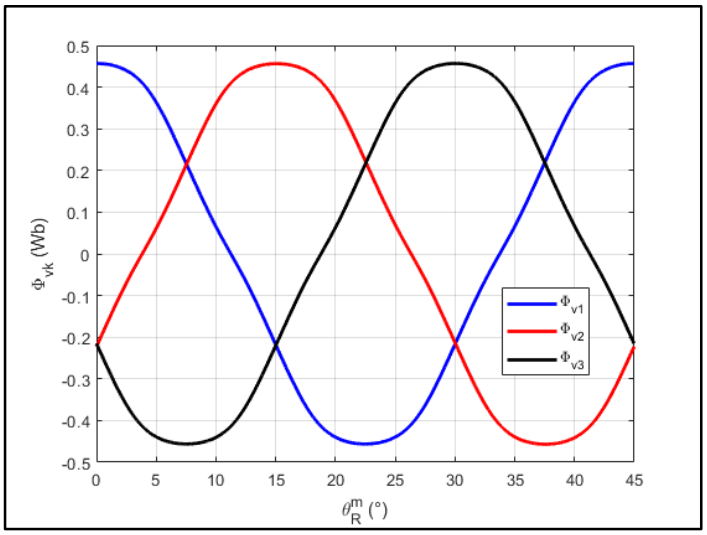

Figure 3-45: No-load flux calculated from their harmonics

Table 3-VI gives the values of the first five harmonics f_n of $\phi_{vk}(\theta_R^m)$.

TABLE 3-VI: The first five harmonics of $\phi_{vk}(\theta_R^m)$

f_1	f_2	f_3	f_4	f_5
0.4625	0.0	0.0071	0.0	-0.0136

3.12.2 Self and mutual inductances

The harmonics dl_n and dm_n of the self and mutual inductance derivatives have been identified in section 3.9 by (3.47) and (3.56b) respectively. The expressions of the self and mutual inductances (3.14) and (3.18) show that their mean values L_s and M_s have to be identified. According to expressions (3.32) and (3.35) additional measurements have to be done. These measurements are electrical measurements performed at particular rotor positions θ_R^L and θ_R^M. Knowing $L_1(\theta_R^L)$ at θ_R^L and the mutual inductance $M_k(\theta_R^M)$ at θ_R^M, the values of mean self and mutual inductances are given by (3.32) and (3.35).

These electrical measurements are not performed on the torque test bench but at blocked positions of the rotor when the permanent magnets are removed. It is natural to choose θ_R^L and θ_R^M among the equilibrium positions of the rotor. Several equilibrium positions have been

tested to perform electrical measurements and eventually the origin position $\theta_R^m = 0$ has been chosen to make the measurements:

$$\theta_R^L = \theta_R^M = 0 \tag{3.64}$$

When phase 1 is supplied, the origin position is an equilibrium position but it is unstable. So during the measurement the rotor is blocked. The phase 1 is supplied by a sinusoidal current at 50 Hz with rms value equal to 1A. The other phases are not supplied. The voltage on all phases are measured. The active and reactive powers are measured as well. These measurements are repeated for phase 2 and phase 3. From these measurements, the identified parameters are summarized in the *TABLE 3-VII.*

TABLE 3-VII: Main electrical parameters for different current values at the unstable equilibrium position

	Phase 1 supplied	Phase 2 supplied	Phase 3 supplied
Resistance, $R_s(\Omega)$	13.10	13.30	12.90
Self-inductance, $L_s(mH)$	38.20	37.90	37.90
Mutual inductance, $M_x(mH)$	-6.20	-6.00	-9.60
Mutual inductance, $M_y(mH)$	-9.90	-10.00	-10.00

Measurements with the phase 1 supplied with sinusoidal current of different rms values are summarized in the *TABLE 3-VIII.*

TABLE 3-VIII: Main electrical parameters for different rms current values

	1.00 A	2.00 A	3.00 A
Resistance, $R_s(\Omega)$	15.80	13.75	14.00
Self-inductance, $L_s(mH)$	42.60	37.10	37.10
Mutual inductance, $M_x(mH)$	-6.70	-6.30	-6.30
Mutual inductance, $M_y(mH)$	-10.4	-9.70	-9.50

From the electrical measurements, the value of self and mutual inductance for the unstable equilibrium position are deduced.

$$\begin{cases} L_1(0) = L_1(\theta_R^L) = 38.0\ mH \\ L_{12}(0) = M_3(0) = -6.1 mH \end{cases} \tag{3.65}$$

Eventually the mean values of the self and mutual inductance are given by:

$$\begin{cases} L_s = L_1(\theta_R^L) - \sum_{n=1}^{\infty} l_n cos(2np\theta_R^L) = L_1(0) - \sum_{n=1}^{\infty} l_n \\ M_s = M_3(\theta_R^M) - \sum_{n=1}^{\infty} m_n cos\left(2n\left(p\theta_R^M - \frac{4\pi}{3}\right)\right) = M_3(0) - \sum_{n=1}^{\infty} m_n cos\left(2n\frac{4\pi}{3}\right) \end{cases} \tag{3.66}$$

Figure 3-46 shows self and mutual inductances obtained from expressions (3.14) and (3.18).

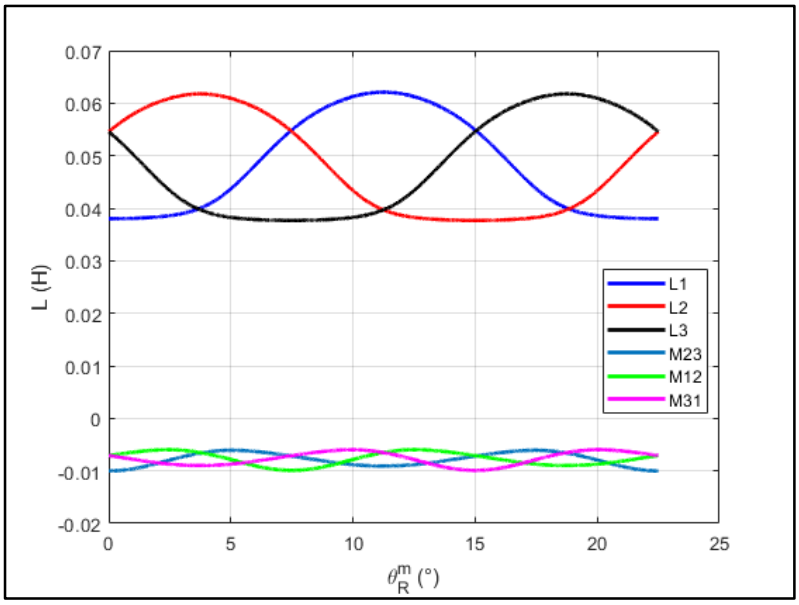

Figure 3-46: Self and mutual inductances calculated from harmonics and mean values

3.12.3 Conclusion

The identification of the flux model parameters closes the identification of all the parameters of torque and flux models of lumped parameter model of the spoke type axial flux permanent magnet motor. By the way the stator resistance too has been identified in *TABLE 3-VI*. The validity has been demonstrated even for higher current than the rated current determined in Chapter 2.

3.13 Study of three phase sinusoidal supplies

The torque and flux models are used to study the behavior of the spoke type axial flux permanent magnet (STAFPM) motor. To guide the study, the DQ0 model is used.

3.13.1 DQ0 Model

To calculate the parameter of the DQ0 model the Park's transformation is used. The matrix of the Park's transformation depends on the electric angular position of the rotor θ_R^e:

$$\boldsymbol{P}(\theta_R^e) = \sqrt{\frac{2}{3}}\begin{bmatrix} \cos(\theta_R^e) & \cos(\theta_R^e - \frac{2\pi}{3}) & \cos\left(\theta_R^e + \frac{2\pi}{3}\right) \\ -\sin(\theta_R^e) & -\sin(\theta_R^e - \frac{2\pi}{3}) & -\sin(\theta_R^e + \frac{2\pi}{3}) \\ \frac{1}{\sqrt{2}} & \frac{1}{\sqrt{2}} & \frac{1}{\sqrt{2}} \end{bmatrix} \tag{3.67}$$

The Park's component of an electric quantities is given by the transpose of the one column matrix $\boldsymbol{x}$:

$$\boldsymbol{x^T} = \{x\}^T = \{x_D, x_Q, x_0\} \tag{3.68}$$

This matrix is related to the one column matrix of an electric quantity $\boldsymbol{X}$ by:

$$\boldsymbol{x} = \boldsymbol{P}(\theta_R^e)\boldsymbol{X} \tag{3.69}$$

For instance, the DQ0 component of the no-load flux matrix is given by:

$$\left\{\phi_{vD}, \phi_{vQ}, \phi_{v0}\right\}^T = \boldsymbol{P}(\theta_R^e)\left\{\phi_{v1}, \phi_{v2}, \phi_{v3}\right\}^T \tag{3.70}$$

Figure 3-47 shows the DQ0 components of no-load flux in function of rotor position obtained by Park's transformation.

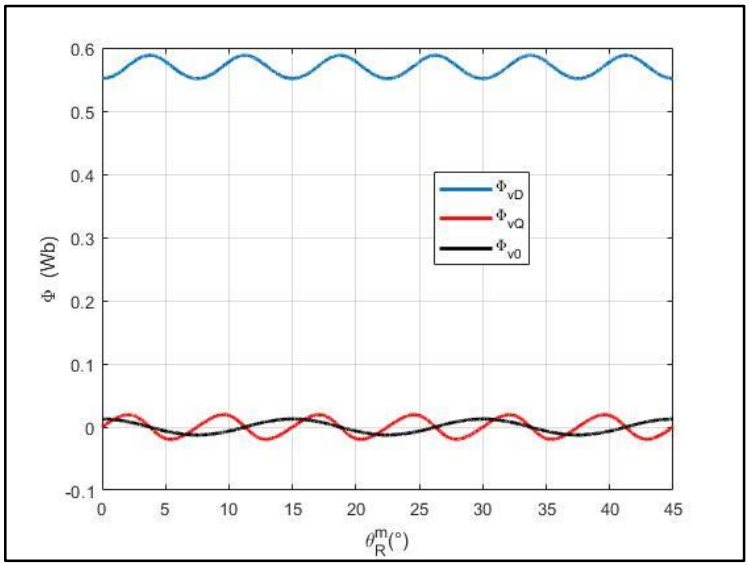

Figure 3-47: DQ0 components of no-load flux calculated

As expected the mean values of the quadrature and homopolar components of the no-load flux are null. The mean value of the direct component of the no-load flux is:

$$\left(\phi_{vD}\right)_{mean} = 0.57\ Wb \tag{3.71}$$

For a self-driven synchronous motor, the currents can be defined as sinusoidal functions of the rotor position knowing its magnitude I_m and its phase shift α from the rotor position:

$$\boldsymbol{I}(\theta_R^m) = \begin{Bmatrix} I_1(\theta_R^m) \\ I_2(\theta_R^m) \\ I_3(\theta_R^m) \end{Bmatrix} = \begin{Bmatrix} I_m cos(p\theta_R^m + \alpha) \\ I_m cos\left(p\theta_R^m + \alpha - \frac{2\pi}{3}\right) \\ I_m cos\left(p\theta_R^m + \alpha - \frac{4\pi}{3}\right) \end{Bmatrix} \tag{3.72}$$

Figure 3.48 shows the definition of the phase shift α in the electric domain.

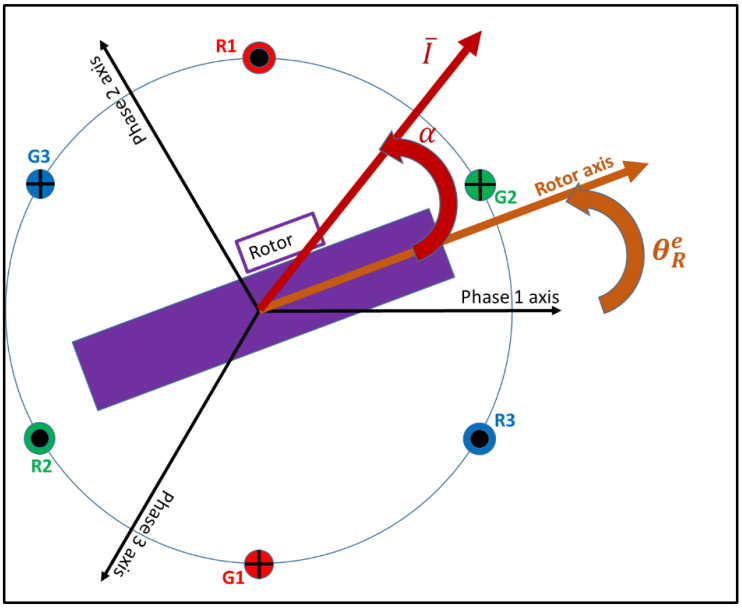

Figure 3-48: Definition of the phase shift α in the electric domain

If the permanent magnets are removed, the flux are given by:

$$\boldsymbol{\Phi}(\theta_R^m) = \boldsymbol{L}(\theta_R^m)\boldsymbol{I} \tag{3.73}$$

The current magnitude I_m is the rated current defined in Chapter 2 whose rms value is:

$$I_{rms} = \frac{I_m}{\sqrt{2}} = 1.5\ A$$

For different values of the phase shift α, the flux without permanent magnets are calculated in function of the rotor position. The corresponding DQ0 components of the flux and current are calculated from Park's transformation. For each phase the direct inductance $L_D(\theta_R^m)$ and the quadrature inductance $L_Q(\theta_R^m)$ is calculated in function of the rotor position by the relations:

$$\begin{cases} L_D(\theta_R^m) = \dfrac{\phi_D(\theta_R^m)}{I_D(\theta_R^m)} \\ L_Q(\theta_R^m) = \dfrac{\phi_Q(\theta_R^m)}{I_Q(\theta_R^m)} \end{cases}$$

For $\alpha = 30°$, the direct inductance $L_D(\theta_R^m)$ and the quadrature inductance $L_Q(\theta_R^m)$ are presented on *Figure 3.49* and for $\alpha = 120°$, on *Figure 3.50*.

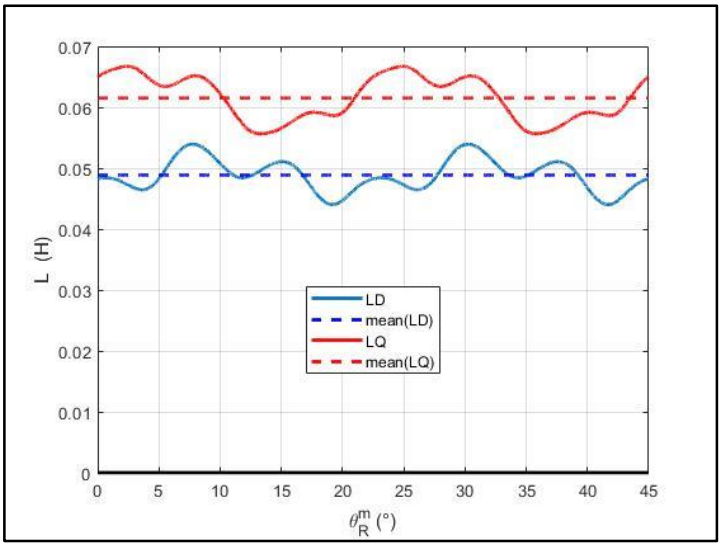

Figure 3-49: Direct inductance $L_D(\theta_R^m)$ and the quadrature inductance $L_Q(\theta_R^m)$ for $\alpha = 30°$

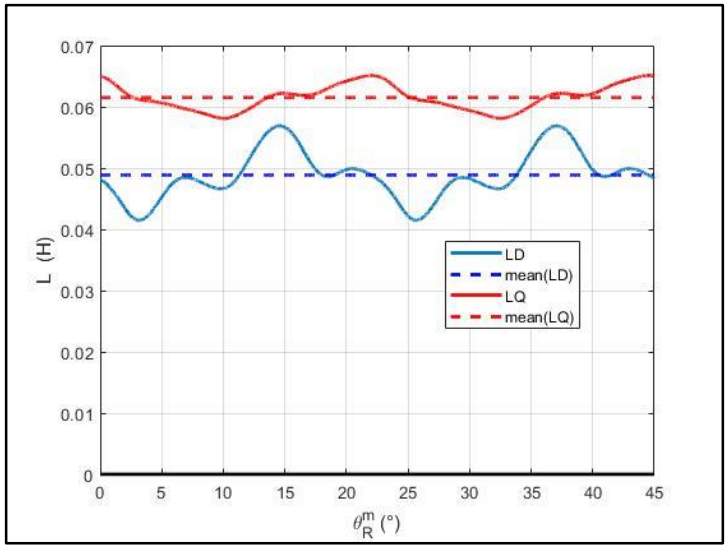

Figure 3-50: Direct inductance $L_D(\theta_R^m)$ and quadrature inductance $L_Q(\theta_R^m)$ for $\alpha = 120°$

Figure 3.49 and *Figure 3.50* show that the direct inductance $L_D(\theta_R^m)$ and the quadrature inductance $L_Q(\theta_R^m)$ have ripples that depends on the phase shift α but the mean values of these inductances do not depend on the phase shift. The mean values are equal to:

$$\begin{cases} (L_D)_{mean} = 48.9mH \\ (L_Q)_{mean} = 61.5mH \end{cases} \tag{3.74}$$

3.13.2 Optimal torque per Ampere by the DQ0 model

In this section, the direct no-load flux ripples and those of the direct and quadrature inductances are neglected. Thus the DQ0 model has the following parameters:

$$\begin{cases} \phi_{vD} = 0.57\ Wb \\ L_D = 48.9mH \\ L_Q = 61.5mH \end{cases} \tag{3.75}$$

The torque given by the DQ0 model is:

$$C_{mot} = p\Phi_{vD} i_Q + p\left(L_D - L_Q\right) i_D i_Q \tag{3.76}$$

From this model it is possible to calculate the optimal torque given the magnitude I_m of the sinusoidal currents (3.72). The current I_b is defined as:

$$I_b = \frac{\phi_{vD}}{L_Q - L_D} = 45.24\ A \tag{3.77}$$

The norm I_{norm} of the rated current in the DQ0 model is:

$$I_{norm} = \sqrt{3} I_{rms} = 2.6A \tag{3.78}$$

The DQ components of the optimal current are:

$$\begin{cases} I_D^{Opt} = \frac{1}{4}\left(I_b - \sqrt{I_b^2 + 8I_{norm}^2}\right) \\ I_Q^{Opt} = \sqrt{I_{norm}^2 - \left(I_D^{Opt}\right)^2} \end{cases} \tag{3.79}$$

The optimal phase shift α_{Opt} is given by:

$$\alpha_{Opt} = atan2\left(I_Q^{Opt}, I_D^{Opt}\right) = 93.3° \tag{3.80}$$

The optimal torque per Ampere for the rated current is:

$$C_{Opt} = p\Phi_{vD} I_Q^{Opt} + p\left(L_D - L_Q\right) I_D^{Opt} I_Q^{Opt} = 11.87\ N.m \tag{3.81}$$

For the rated current, the torque, given by (3.76), in function of the phase shift α is plotted in *Figure 3.51*. It is compared to the electromagnetic torque given by (3.82):

$$C_{em} = p\Phi_{vD} i_Q \tag{3.82}$$

As expected the optimal electromagnetic torque is obtained for $\alpha = 90°$ and the optimal torque is obtained for $\alpha = \alpha_{Opt} = 93.3°$.

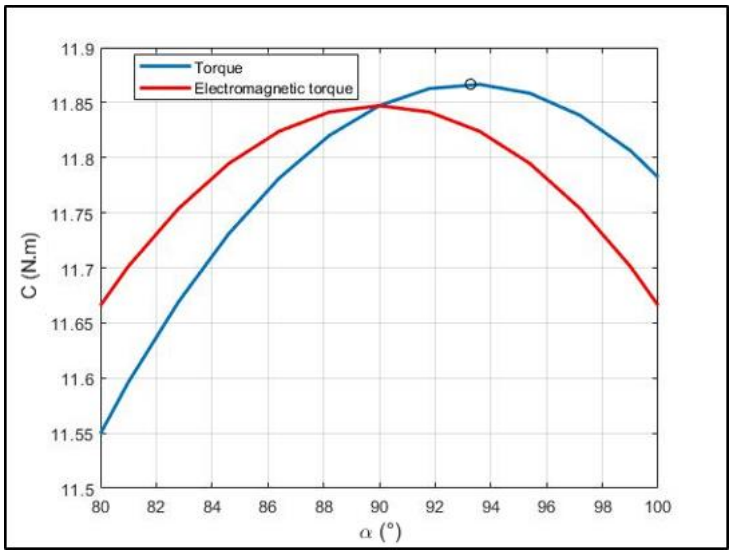

Figure 3-51: Torque and electromagnetic torque versus α

3.13.3 Optimal torque per Ampere by the lumped parameter model

In this section, for the rated current, the torque calculated by the lumped parameter model is calculated in function of the phase shift α. The currents are given by (3.72) in function of the rotor position and the torque is calculated by:

$$C_R(\theta_R^m) = \begin{cases} C_d(\theta_R^m) + \{I_1(\theta_R^m) \quad I_2(\theta_R^m) \quad I_3(\theta_R^m)\} \begin{Bmatrix} \frac{d\phi_{v1}}{d\theta_R^m}(\theta_R^m) \\ \frac{d\phi_{v2}}{d\theta_R^m}(\theta_R^m) \\ \frac{d\phi_{v3}}{d\theta_R^m}(\theta_R^m) \end{Bmatrix} \\ +\frac{1}{2}\{I_1(\theta_R^m) \quad I_2(\theta_R^m) \quad I_3(\theta_R^m)\} \frac{d\boldsymbol{L}(\theta_R^m)}{d\theta_R^m} \begin{Bmatrix} I_1(\theta_R^m) \\ I_2(\theta_R^m) \\ I_3(\theta_R^m) \end{Bmatrix} \end{cases} \tag{3.83}$$

Figure 3.52 to *Figure 3.54* plotted the torque in function of the rotor position for three values of the phase shift around the optimal phase shift.

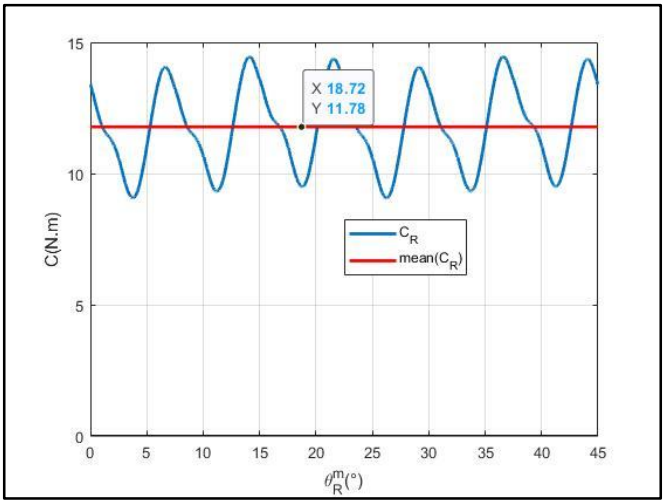

Figure 3-52: $C_R(\theta_R^m)$ for $\alpha = 87°$

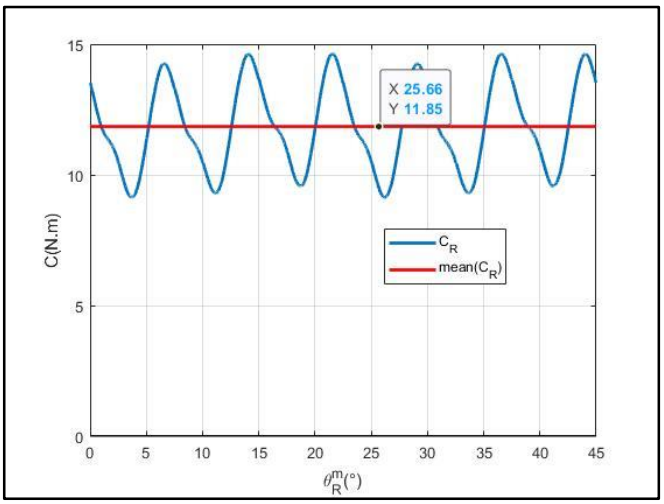

Figure 3-53: $C_R(\theta_R^m)$ for $\alpha = \alpha_{Opt} = 93.3°$

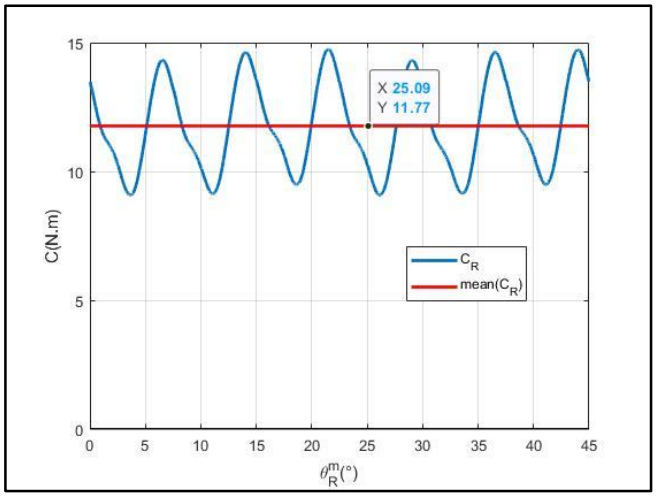

Figure 3-54: $C_R(\theta_R^m)$ for $\alpha = 100.0°$

Figure 3.52 to *Figure 3.54* shows that the torque has ripples. *TABLE 3-IX* compares the mean torque obtained by the lumped parameter model (3.63) to the torque obtained by the DQ model (3.76)

TABLE 3-IX: Comparison of the mean torque from the lumped parameter model and DQ model

$\alpha = 87$	$\left(C_R(\theta_R^m)\right)_{mean} = 11.78\ N.m$	$C_{mot} = 11.79\ N.m$
$\alpha = \alpha_{Opt}$	$\left(C_R(\theta_R^m)\right)_{mean} = 11.85\ N.m$	$C_{mot} = 11.87\ N.m$
$\alpha = 100.0°$	$\left(C_R(\theta_R^m)\right)_{mean} = 11.77\ N.m$	$C_{mot} = 11.78\ N.m$

TABLE 3-VIII shows that the DQ model gives very good results compared to those from the lumped parameter model. It means that to size the STAFPM motor it is sufficient to have a model that calculates accurately the DQ model parameters: ϕ_{vD}, L_D and L_Q. A 3D numerical sizing model based on finite difference method is proposed in Chapter 4.

To evaluate the torque ripples two solutions are proposed. If the motor has not been fabricated, one may use 3D finite element analysis but this method has very high computing time. If the motor is fabricated, the proposed experimental studies show how to identify all the parameters of the general electromechanical lumped model. This method may be very fast, but need a test bench that allows to measure static torques.

3.14 Conclusion

In this chapter, an experimental test bench allows to measure the static torque of an electric motor in function of the rotor position. An original method to identify, from static torque measurements, most of the parameters of the electromechanical lumped parameter model of an electric motor is proposed.

Additional static torque measurements are performed for DC single, double or three phase supplies. The measurements allow to validate the proposed numerical treatment to remove imperfections on signals, the proposed identification methods and the identified parameters.

When all the parameters are identified, the general electromechanical model allows to perform very fine and quick studies of the motor. The torque ripples for instance are quickly reproduced with a high fidelity.

The results obtained show the drawbacks and the advantages of the most used model of electric motor, the DQ model, which cannot reproduce torque ripples but can accurately calculate the mean torque. The proposed general model validates the capacity of the DQ model to calculate the optimal torque per Ampere of STAFPM motors. So to size STAFPM motors, one need a sizing model that can accurately and quickly calculates the DQ model parameters. Chapter 4 proposes a numerical sizing model based on 3D finite difference method.

Chapter 4
3D NUMERICAL SIZING MODEL of STAFPM MOTOR

4.1 Introduction

This chapter is dedicated to the sizing model of STAFPM motor. The common analytical sizing model based on magnetic field calculation cannot be applied to STAFPM motor due to the ferromagnetic polar pieces on the rotor. Chapter 3 shows that the classical DQ model allows to calculate the mean optimal torque per Ampere. This chapter proposes a sizing model that allows to quickly calculate the parameters of the DQ model: no-load flux, the direct and quadrature inductances. This sizing model is based on static model of the magnetic field in STAFPM motor. As analytical models of the magnetic field cannot be applied to STAFPM motor, a numerical model is proposed. This numerical model is based on the 3D finite difference method.

To reduce the time computation strong assumptions are done. As the main target is the mean torque, the model does not have to calculate the ripples due to slots. So the STAFPM motor considered are with slotless stator. The ferromagnetic part of the stator is considered to have infinite permeability. The stator is considered only by the wave of surface current density on stator bore as in [13].

To reduce more the study domain, all the symmetries of the geometry and the physical properties of the rotor are taken into account. To be able to take into account all the symmetries, the magnetic field calculation is done in three steps: first the open-circuit magnetic field is calculated, then the direct armature reaction magnetic field and at the end the quadrature magnetic field. For each of these three magnetic field problems, the study domain can be reduced to only the half pole. But for each problem, the magnetic field sources and the boundary conditions are specific.

First the general magnetostatic field problem is recalled. In the framework of cylindrical coordinates, the general problem is developed inside the appropriate study domain for STAFPM motor. Eventually the formulation in scalar magnetic potential is developed for each problem.

The finite difference method is applied to solve the three magnetic field problems. The finite difference scheme is developed inside volume, at the interfaces and on boundary conditions.

An original flux calculation in the framework of magnetic scalar potential is developed. This method of flux calculation allows to calculate the no-load magnetic flux from the open

circuit magnetic field problem, the direct inductance from the direct armature reaction magnetic field and the quadrature inductance from the quadrature armature reaction magnetic field. The final results are compared to the one obtained from the experimental studies.

4.2 Nomenclature

In the following, the variable names in *TABLE 4.I* are used.

TABLE 4-I: NOMENCLATURE

Magnetic flux density	B
Magnetic field intensity	H
Permanent magnet magnetization	M
Magnetic scalar potential	ψ
Free space permeability	μ_0
Permanent magnet permeability	μ_{PM}
Iron permeability	μ_{Fe}
Number of poles pairs	p
Internal radius of motor	R_{int}
External radius of motor	R_{ext}
Radial thickness of internal non-magnetic region	L_{int}
Radial thickness of external non-magnetic region	L_{ext}
Length of the magnet region	L_m
Angular width of half magnet pole	t_a
Angular width of half iron pole	t_{ip}
Axial thickness of non-magnetic region	h_{nm}
Axial thickness of permanent magnet region	h_m
Axial thickness of air gap	g

4.3 Magnetostatic field problem

The STAFPM motor is presented in *Figure 4.1* which shows the rotor and stator geometry.

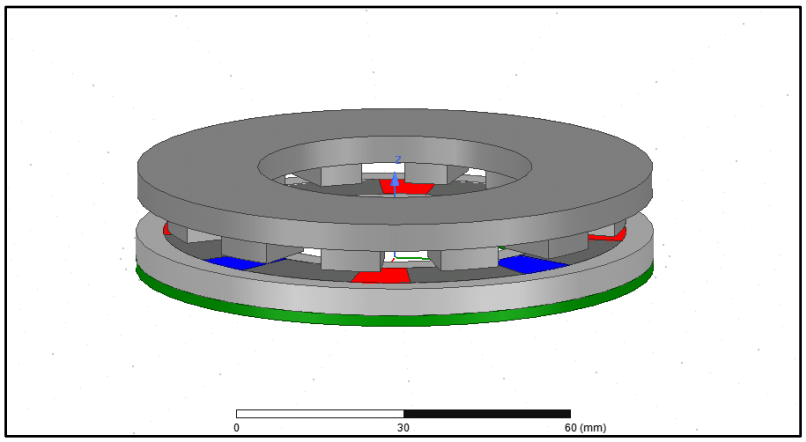

Figure 4-1: Full 3D view for the STAFPM geometry

The study domain is made of m magnetic media:

$$\Omega = \bigcup_{n=1}^{m} \Omega_n \tag{4.1}$$

The different magnetic media are shown on the one pole view on *Figure 4.2*. The slot effects are neglected and the permeability of stator is assumed to be infinite. So the stator is not part of the study domain.

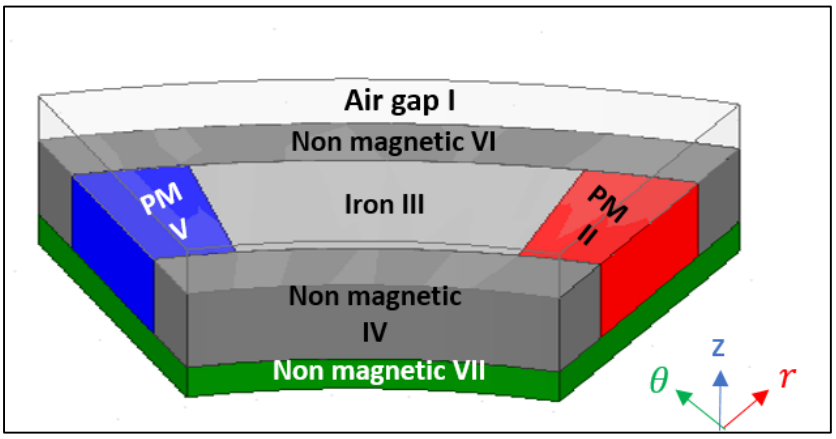

Figure 4-2: Different magnetic media of the STAFPM motor on one pole

In *Figure 4.2* each medium is numbered with the index k from 1 to 7 and noted mathematically as Ω_k. A magnetic medium has two magnetic properties which are:

- The relative magnetic permeability μ_{rk} or magnetic permeability $\mu_k = \mu_{rk}\mu_0$;
- The vector polarization $\overrightarrow{J_k}$.

Inside medium Ω_k, the magnetic flux density vector $\overrightarrow{B_k}$ and the magnetic field intensity vector $\overrightarrow{H_k}$ are linked by the constitutive law:

$$\overrightarrow{B_k} = \mu_k \overrightarrow{H_k} + \overrightarrow{J_k} = \mu_{rk}\mu_0 \overrightarrow{H_k} + \overrightarrow{J_k} \tag{4.2}$$

As armature reactions are taken into account by appropriate boundary conditions on stator bore, there are no volume current density inside the considered media. Ampere's theorem and magnetic conservative law are expressed by:

$$\begin{cases} \overrightarrow{rot}\left(\overrightarrow{H_k}\right) = \vec{0} \\ div\left(\overrightarrow{B_k}\right) = 0 \end{cases} \tag{4.3}$$

The interface Σ_{kl} between two media Ω_k and Ω_l is defined by:

$$\Sigma_{kl} = \Omega_k \cap \Omega_l \tag{4.4}$$

The unit vector $\vec{n}$ on the interface is directed from Ω_k to Ω_l. There are no surface current density and surface charge density on interfaces. The Ampere's theorem and conservation law applied on Σ_{kl} lead to:

$$\begin{cases} \left(\overrightarrow{B_l} - \overrightarrow{B_k}\right).\vec{n} = 0 \\ \left(\overrightarrow{H_l} - \overrightarrow{H_k}\right) \wedge \vec{n} = 0 \end{cases} \tag{4.5}$$

At boundary limiting the study domain Ω, as the magnetic field exterior to Ω is neglected and assumed to be null, the normal flux density is null:

$$\vec{B}\,.\vec{n} = B_n = 0 \tag{4.6a}$$

At surfaces of symmetry, two cases may happen:

- if the magnetic flux density is tangential, the boundary condition (4.6a) is applied;
- if the magnetic field intensity is normal, the boundary condition (4.6b) is applied:

$$\vec{H} \wedge \vec{n} = 0 \tag{4.6b}$$

The stator is taken into account by boundary conditions on stator bore. For the open circuit magnetic field problem, there are no magnetic source on stator bore and boundary condition (4.5) is applied. In the armature reaction magnetic field problems, the armature reaction is replaced by a surface current density wave on the stator bore and boundary condition (4.6c) is applied:

$$\vec{H} \wedge \vec{n} = \vec{K} \tag{4.6c}$$

Considering all the geometrical and physical property symmetries, to reduce the computation for each magnetic field problem, the study domain is reduced to a half pole as shown in *Figure 4-3*.

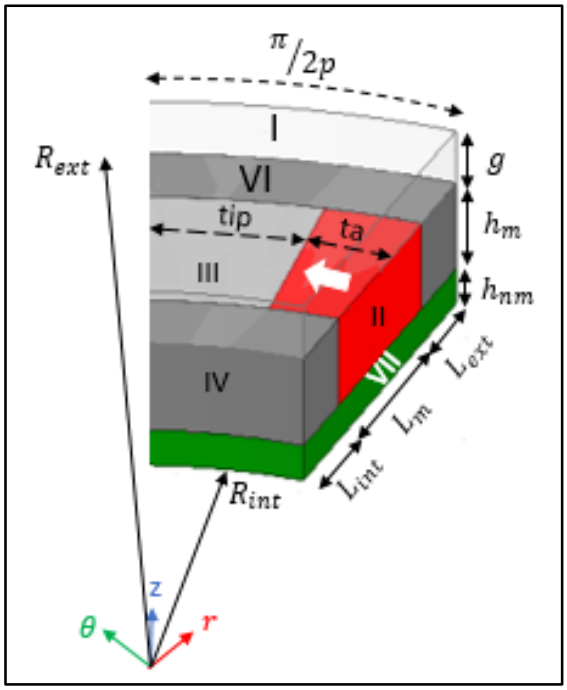

Figure 4-3: Reduced study domain and the parametrization of the geometry

4.4 Modeling the stator

The stator is not modeled as a volume made of different media like iron and winding. In [13], a sizing model of radial flux surface mounted permanent magnet synchronous motor based on 2D analytical field model has been developed. The stator is taken into account by the conductor distribution function along the stator bore. This approach has been extended to axial flux surface mounted permanent magnet synchronous motor in [18]. This approach is applied to STAFPM motor.

4.4.1 Linear conductor distribution function

The stator has n_c conductors per slot. In axial flux motor, the slot opening angular width $\theta_{so}(r)$ depends on the radial position r. The linear width $w_{so}(r)$ of the slot opening in the azimuthal direction is:

$$w_{so}(r) = r\theta_{so}(r) \tag{4.7}$$

The number of conductors per meter $C_M(r)$ along each slot opening depends on the radial position and is expressed by:

$$C_M(r) = \frac{n_c}{w_{so}(r)} \tag{4.8}$$

Elsewhere on the stator bore surface, the number of conductors per meter is null. For example for a stator with three slots per pole and per phase, the linear distribution function of conductor $C_1(r,\theta)$ of phase 1 at radial position r looks like the one shown on *Figure 4.4*. A positive value reveals a slot with 'go' conductors and negative value, a slot with 'return' conductors.

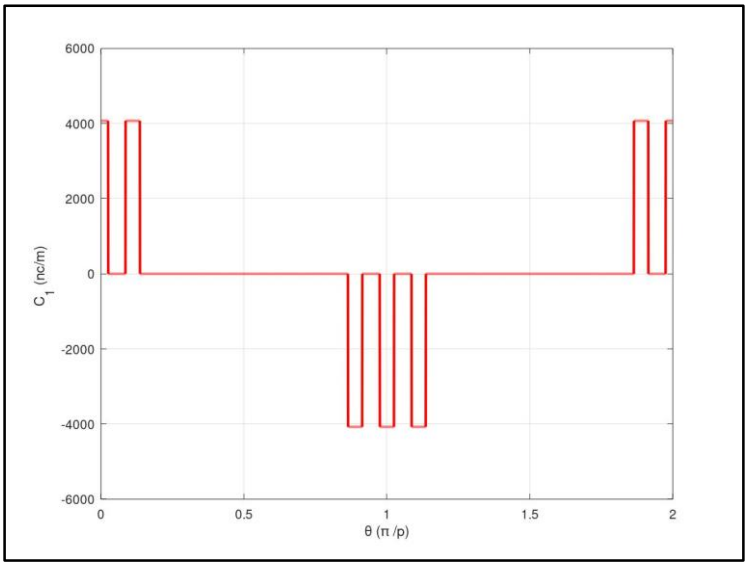

Figure 4-4: Example of the linear distribution function of conductor $C_1(r,\theta)$ at radial position r

For the sake of simplicity, only integer distributed windings are considered: the number of slots per pole and per phase n_{epp} is an integer. For a motor with p pole pairs and q phases the number of slots is:

$$n_e = 2pqn_{epp} \tag{4.9}$$

The angular width of tooth pitch is:

$$\theta_d = \frac{2\pi}{n_e} \tag{4.10}$$

Thus, the linear conductor distribution function $C_1(r,\theta)$ of phase 1 is expressed as:

$$C_1(r,\theta) = \sum_{n=1}^{\infty} \frac{4C_M(r)}{\pi} \frac{sin\left((2n-1)p\frac{\theta_{so}(r)}{2}\right)}{(2n-1)} \frac{sin\left(n_{epp}\frac{(2n-1)p\,\theta_d}{2}\right)}{sin\left(\frac{(2n-1)p\,\theta_d}{2}\right)} cos\big((2n-1)p\theta\big) \tag{4.11}$$

For with only one slot per pole and per phase, the linear conductor distribution function is:

$$C_1(r,\theta) = \sum_{n=1}^{\infty} \frac{4C_M(r)}{\pi} \frac{sin\left((2n-1)p\frac{\theta_{so}(r)}{2}\right)}{(2n-1)} cos\big((2n-1)p\theta\big) \tag{4.12}$$

Figure 4.5 shows the linear conductor distribution function of phase 1 for the existing surface mounted permanent magnet axial flux (SMPMAF) initial prototype at three different radial positions. This prototype has two slots per pole and per phase and 95 conductors per slots. For this motor, the slot opening linear width w_{so} does not depend on the radial position, so the angular width is given by:

$$\theta_{so}(r) = \frac{w_{so}}{r} \tag{4.13}$$

$C_1(r,\theta)$ is reconstructed from its harmonics given by (4.11).

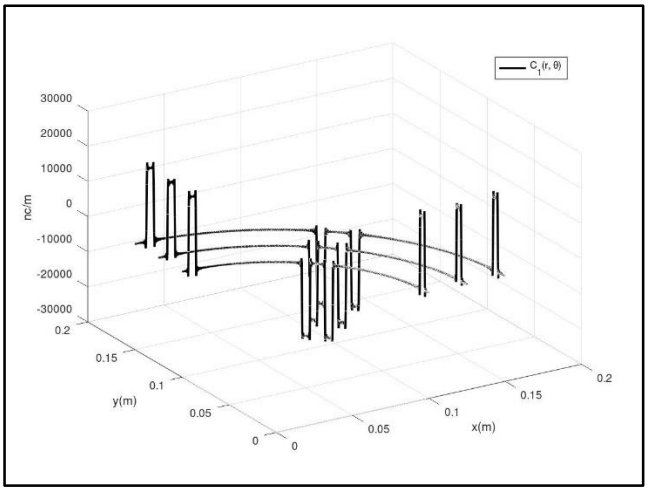

Figure 4-5: $C_1(r,\theta)$ at three different radius for the SMPMAF for the initial prototype

Figure 4.6 shows the linear conductor distribution function of the STAFPM prototype studied in Chapter 3. $C_1(r,\theta)$ is reconstructed from its harmonics given by (4.12) and viewed as a surface.

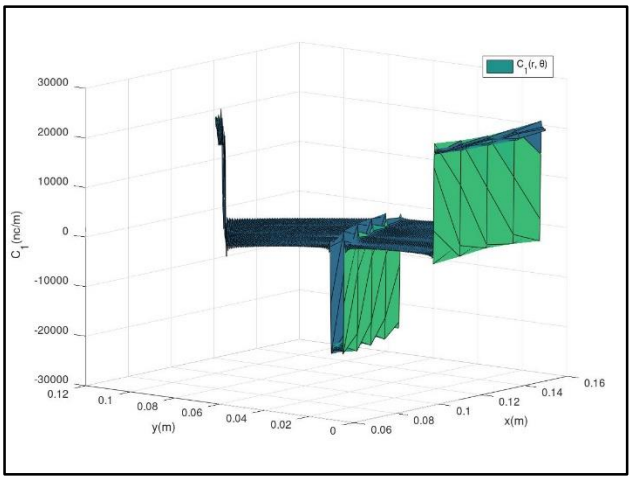

Figure 4-6: $C_1(r,\theta)$ viewed as a surface for the STAFPM prototype studied in chapter 3

The linear conductor distribution function for a phase k is given by:

$$C_k(r,\theta) = C_k(r,p\theta) = C_1\left(r,\theta-(k-1)\frac{2\pi}{p3}\right) = C_1\left(r,p\theta-(k-1)\frac{2\pi}{3}\right) \quad (4.14)$$

It can be expressed in the form:

$$C_k(r,p\theta) = \sum_{n=1}^{\infty} a_n(r)\cos\left((2n-1)\left(p\theta-(k-1)\frac{2\pi}{3}\right)\right) \quad (4.15)$$

4.4.2 Surface current density wave

Each phase is supplied by a sinusoidal current. If $p\theta_R^m$ is the electric angular position of the rotor according to (3.72) the current in phase k is in the form:

$$I_k(\theta_R^m) = I_C\cos\left(p\theta_R^m-(k-1)\frac{2\pi}{3}\right) + I_S\sin\left(p\theta_R^m-(k-1)\frac{2\pi}{3}\right) \quad (4.16)$$

If α is the phase shift of the current from the rotor position and I_m, the magnitude of the currents, the cosine and sine components of the currents may be written:

$$\begin{cases} I_C = I_m cos(\alpha) \\ I_S = -I_m sin(\alpha) \end{cases} \quad (4.17)$$

The surface current density wave is given by:

$$K_S(r, p\theta, \theta_R^m) = \sum_{k=1}^{3} C_k(r, p\theta) \quad _k(\theta_R^m) \quad (4.18)$$

After development, from (4.18) and (4.15), it can be put in the form:

$$K_S(r, \theta, \theta_R^m) = \frac{3}{2} a_1(r)\left(I_C cos(p\theta_R^m - p\theta) + I_S sin(p\theta_R^m - p\theta)\right) + \frac{3}{2}\left(\sum_{m=1}^{\infty} a_{3m}(r)\left(I_C cos(p\theta_R^m + (6m-1)p\theta) + I_S sin(p\theta_R^m + (6m-1)p\theta)\right) + a_{3m+1}(r)\left(I_C cos(p\theta_R^m - (6m+1)p\theta) + I_S sin(p\theta_R^m - (6m+1)p\theta)\right)\right) \quad (4.19)$$

4.4.3 Surface current density distribution for armature reaction field problems

For the STAFPM motor, the chosen distribution of conductors of the reference phase, phase 1, is given on *Figure 4.5* and the chosen rotor position is given by *Figure 4.2* or *Figure 4.3*. The angular position of the rotor is then:

$$\theta_R^m = 0 \quad (4.20)$$

At the origin of time $(t = 0)$, the armature reaction field is in the direct axis and the phase shift α is null and the current in phase k is:

$$I_k(0) = I_m cos\left((k-1)\frac{2\pi}{3}\right) \quad (4.21)$$

From (4.17) and (4.19), the distribution of surface current density along the stator for the direct armature reaction field problem is then given by:

$$K_D(r, \theta) = K_S(r, \theta, 0) = \frac{3}{2} a_1(r) I_m cos(p\theta) + \frac{3}{2}\left(\sum_{m=1}^{\infty} a_{3m}(r) I_m cos\left((6m-1)p\theta\right) + a_{3m+1}(r) I_m cos(6m+1)p\theta\right) \quad (4.22)$$

In the same manner, the quadrature armature reaction field in the quadrature axis and the phase shift α is equal to $\frac{\pi}{2}$ and the current in phase k is:

$$I_k(0) = -I_m sin\left((k-1)\frac{2\pi}{3}\right) \quad (4.23)$$

From (4.19) and (4.22), the distribution of surface current density along the stator for the quadrature armature reaction field problem is then given by:

$$K_Q(r, \theta) = K_S(r, \theta, 0) = \frac{3}{2} a_1(r) I_m sin(p\theta) + \frac{3}{2}\left(\sum_{m=1}^{\infty} -a_{3m}(r) I_m sin\left((6m-1)p\theta\right) + a_{3m+1}(r) I_m sin\left((6m+1)p\theta\right)\right) \quad (4.24)$$

Figure 4.7 and *Figure 4.8* show the distribution of the surface current density along the stator respectively for the direct and quadrature armature reaction field problems.

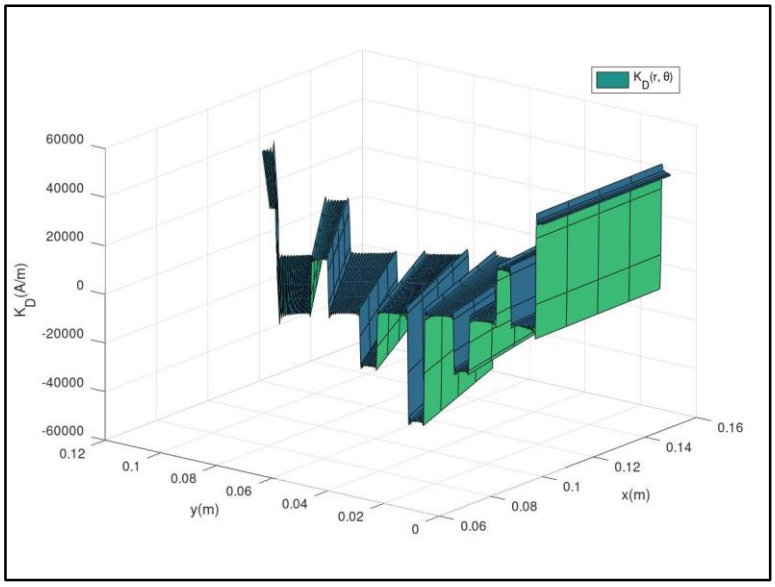

Figure 4-7: Distribution of $K_D(r,\theta)$ on the stator bore for the direct reaction field problem

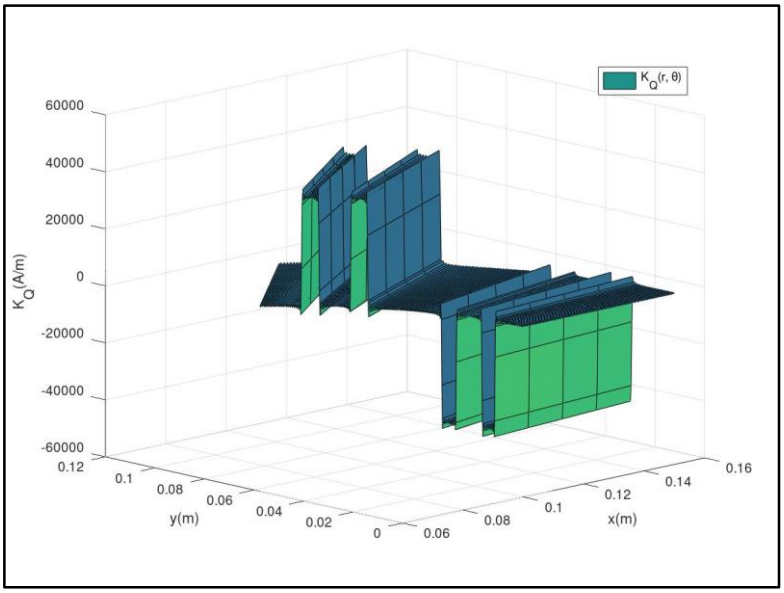

Figure 4-8: Distribution of $K_Q(r,\theta)$ on the stator bore for the quadrature reaction field problem

4.5 Magnetic scalar potential formulation

As there are no volume current inside the study domain Ω, due to the first equation of (4.3), magnetic scalar potential ψ can be introduced:

$$\overrightarrow{H_k} = -\vec{\nabla}(\psi_k) \tag{4.25}$$

The magnetic scalar potential formulation is developed in cylindrical coordinates:

$$\overrightarrow{H_k} = -\frac{\partial \psi_k}{\partial r}\overrightarrow{e_r} - \frac{1}{r}\frac{\partial \psi_k}{\partial \theta}\overrightarrow{e_\theta} - \frac{\partial \psi_k}{\partial z}\overrightarrow{e_z} \tag{4.26}$$

To simplify equation expressions, the magnetization vector is introduced:

$$\overrightarrow{M_k} = \frac{\overrightarrow{J_k}}{\mu_k} \tag{4.27}$$

In each medium Ω_k, the second equation of (4.3) and (4.2) lead to:

$$\vec{\nabla}.\vec{\nabla}(\psi_k) = \vec{\nabla}.\overrightarrow{M_k} \tag{4.28}$$

For STAFPM motor the vector magnetization is azimuthal and its magnitude is uniform inside each medium:

$$\overrightarrow{M_k} = M_k\overrightarrow{e_\theta} \tag{4.29}$$

So the magnetization in each medium is divergence free and the magnetic scalar potential equation is Laplacian equation:

$$\Delta(\psi_k) = \frac{\partial^2\psi_k}{\partial r^2} + \frac{1}{r}\frac{\partial\psi_k}{\partial r} + \frac{1}{r^2}\frac{\partial^2\psi_k}{\partial\theta^2} + \frac{\partial^2\psi_k}{\partial z^2} = 0 \tag{4.30}$$

For the three magnetic field problems, there are no surface current density between the different media defined on *Figure 4.2* or *Figure 4.3*. According to (4.5), on each interface the tangential components of the magnetic field intensity are continuous. As the tangential components of the magnetic field intensity are the tangential derivatives of magnetic scalar potential, the simplest way to guarantee their continuity is that, at each interface, the scalar potential is continuous. This means that only one magnetic scalar potential is considered over all the study domain:

$$\psi_k(r,\theta,z) = \psi(r,\theta,z) \tag{4.31}$$

In the study domain, the equation is:

$$\frac{\partial^2\psi}{\partial r^2} + \frac{1}{r}\frac{\partial\psi}{\partial r} + \frac{1}{r^2}\frac{\partial^2\psi}{\partial\theta^2} + \frac{\partial^2\psi}{\partial z^2} = 0 \tag{4.32}$$

In each media, the magnetic field intensity is given by:

$$\vec{H}(r,\theta,z) = -\frac{\partial\psi}{\partial r}\overrightarrow{e_r} - \frac{1}{r}\frac{\partial\psi}{\partial\theta}\overrightarrow{e_\theta} - \frac{\partial\psi}{\partial z}\overrightarrow{e_z} \tag{4.33}$$

According to Figure 4.3, the media limits are defined *TABLE 4.II*

TABLE 4-II: Study domain media limits

Radial limits of media	Azimuthal limits	Axial limits
$\begin{cases} R_{L1} = R_{int} \\ R_{L2} = R_{int} + L_{int} \\ R_{L3} = R_{L2} + L_m \\ R_{L4} = R_{L3} + L_{ext} \end{cases}$	$\begin{cases} \theta_{L1} = 0 \\ \theta_{L2} = t_a \\ \theta_{L3} = t_a + t_{ip} = \dfrac{\pi}{2p} \end{cases}$	$\begin{cases} Z_{L1} = -h_{nm} \\ Z_{L2} = Z_{L1} + h_{nm} = 0 \\ Z_{L3} = Z_{L2} + h_m = h_m \\ Z_{L4} = Z_{L3} + g \end{cases}$

Using Arabic instead of Roman numeration, the magnetic scalar formulation in each medium is developed in the following sections.

4.5.1 Airgap

The airgap is the medium Ω_1 defined by the limits:

$$\begin{cases} R_{L1} < r < R_{L4} \\ \theta_{L1} < \theta < \theta_{L3} \\ Z_{L3} < z < Z_{L4} \end{cases} \tag{4.34}$$

The medium constitutive law is:

$$\overrightarrow{B_1}(r,\theta,z) = \mu_0 \overrightarrow{H_1}(r,\theta,z) \tag{4.35}$$

4.5.2 Permanent magnet

The permanent magnet is the medium Ω_2 defined by the limits:

$$\begin{cases} R_{L2} < r < R_{L3} \\ \theta_{L1} < \theta < \theta_{L2} \\ Z_{L2} < z < Z_{L3} \end{cases} \tag{4.36}$$

The medium constitutive law is:

$$\overrightarrow{B_2}(r,\theta,z) = \mu_{PM}\left(\overrightarrow{H_2}(r,\theta,z) + \overrightarrow{M_2}\right) \tag{4.37}$$

4.5.3 Ferromagnetic pole

The ferromagnetic pole is the medium Ω_3 defined by the limits:

$$\begin{cases} R_{L2} < r < R_{L3} \\ \theta_{L2} < \theta < \theta_{L3} \\ Z_{L2} < z < Z_{L3} \end{cases} \tag{4.38}$$

The medium constitutive law is:

$$\overrightarrow{B_3}(r,\theta,z) = \mu_{Fe} \overrightarrow{H_3}(r,\theta,z) \tag{4.39}$$

4.5.4 Nonmagnetic media

The other media are the interior media Ω_4:

$$\begin{cases} R_{L1} < r < R_{L2} \\ \theta_{L1} < \theta < \theta_{L3} \\ Z_{L2} \leq z < Z_{L3} \end{cases} \tag{4.40}$$

the exterior region Ω_6:

$$\begin{cases} R_{L3} < r < R_{L4} \\ \theta_{L1} < \theta < \theta_{L3} \\ Z_{L2} \leq z < Z_{L3} \end{cases} \tag{4.41}$$

and the bottom medium Ω_7 :

$$\begin{cases} R_{L1} < r < R_{L4} \\ \theta_{L1} < \theta < \theta_{L3} \\ Z_{L1} < z < Z_{L2} \end{cases} \tag{4.42}$$

They are nonmagnetic as the airgap.

4.6 Continuity conditions with the ferromagnetic pole

The continuity of the tangential components of the magnetic field intensity at interfaces are fulfilled by the continuity of the magnetic scalar potential. Only the continuity of the normal component of the magnetic flux density is considered in this section and the following one. The interface of the ferromagnetic pole and the airgap, $\Sigma_{31} = \Omega_3 \cap \Omega_1$, is defined by:

$$\begin{cases} R_{L2} < r < R_{L3} \\ \theta_{L2} < \theta < \theta_{L3} \\ z = Z_{L3} \end{cases} \tag{4.43}$$

The continuity of the normal component, $B_z(r, \theta, Z_{L3})$, is:

$$\mu_{Fe} \frac{\partial \psi}{\partial z}(r, \theta, Z_{L3}^-) - \mu_0 \frac{\partial \psi}{\partial z}(r, \theta, Z_{L3}^+) = 0 \tag{4.44}$$

The interface of the ferromagnetic pole and the nonmagnetic bottom region, $\Sigma_{37} = \Omega_3 \cap \Omega_7$, is defined by:

$$\begin{cases} R_{L2} < r < R_{L3} \\ \theta_{L2} < \theta < \theta_{L3} \\ z = Z_{L2} \end{cases} \tag{4.45}$$

The continuity of the normal component, $B_z(r, \theta, Z_{L2})$, is:

$$\mu_{Fe} \frac{\partial \psi}{\partial z}(r, \theta, Z_{L2}^+) - \mu_0 \frac{\partial \psi}{\partial z}(r, \theta, Z_{L2}^-) = 0 \tag{4.46}$$

The interface of the ferromagnetic pole and the nonmagnetic interior medium, $\Sigma_{34} = \Omega_3 \cap \Omega_4$, is defined by:

$$\begin{cases} r = R_{L2} \\ \theta_{L2} < \theta < \theta_{L3} \\ Z_{L2} < z < Z_{L3} \end{cases} \tag{4.47}$$

The continuity of the normal component, $B_r(R_{L2}, \theta, z)$, is:

$$\mu_{Fe} \frac{\partial \psi}{\partial r}(R_{L2}^+, \theta, z) - \mu_0 \frac{\partial \psi}{\partial r}(R_{L2}^-, \theta, z) = 0 \tag{4.48}$$

The interface of the ferromagnetic pole and the nonmagnetic exterior medium, $\Sigma_{36} = \Omega_3 \cap \Omega_6$, is defined by:

$$\begin{cases} r = R_{L3} \\ \theta_{L2} < \theta < \theta_{L3} \\ Z_{L2} < z < Z_{L3} \end{cases} \tag{4.49}$$

The continuity of the normal component, $B_r(R_{L3}, \theta, z)$, is:

$$\mu_{Fe} \frac{\partial \psi}{\partial r}(R_{L3}^-, \theta, z) - \mu_0 \frac{\partial \psi}{\partial r}(R_{L3}^+, \theta, z) = 0 \tag{4.50}$$

4.7 Continuity conditions with the permanent magnet

The interface of the permanent magnet and the ferromagnetic pole, $\Sigma_{23} = \Omega_2 \cap \Omega_3$, is defined by:

$$\begin{cases} R_{L2} < r < R_{L3} \\ \theta = \theta_{L2} \\ Z_{L2} < z < Z_{L3} \end{cases} \tag{4.51}$$

The continuity of the normal component, $B_\theta(r, \theta_{L2}, z)$, is:

$$\mu_{Fe} \frac{\partial \psi}{\partial \theta}(r, \theta_{L2}^+, z) - \mu_{PM} \frac{\partial \psi}{\partial \theta}(r, \theta_{L2}^-, z) + \mu_{PM} r M = 0 \tag{4.52}$$

The interface of the permanent magnet and the airgap, $\Sigma_{21} = \Omega_2 \cap \Omega_1$, is defined by:

$$\begin{cases} R_{L2} < r < R_{L3} \\ \theta_{L1} < \theta < \theta_{L2} \\ z = Z_{L3} \end{cases} \tag{4.53}$$

The continuity of the normal component, $B_z(r,\theta,Z_{L3})$, is:

$$\mu_{PM}\frac{\partial\psi}{\partial z}(r,\theta,Z_{L3}^-)-\mu_0\frac{\partial\psi}{\partial z}(r,\theta,Z_{L3}^+)=0 \tag{4.54}$$

The interface of the permanent magnet and the nonmagnetic bottom medium, $\Sigma_{27}=\Omega_2\cap\Omega_7$, is defined by:

$$\begin{cases}R_{L2}<r<R_{L3}\\ \theta_{L1}<\theta<\theta_{L2}\\ z=Z_{L2}\end{cases} \tag{4.55}$$

The continuity of the normal component, $B_z(r,\theta,Z_{L2})$, is:

$$\mu_{PM}\frac{\partial\psi}{\partial z}(r,\theta,Z_{L2}^+)-\mu_0\frac{\partial\psi}{\partial z}(r,\theta,Z_{L2}^-)=0 \tag{4.56}$$

The interface of the permanent magnet and the nonmagnetic interior medium, $\Sigma_{24}=\Omega_2\cap\Omega_4$, is defined by:

$$\begin{cases}r=R_{L2}\\ \theta_{L1}<\theta<\theta_{L2}\\ Z_{L2}<z<Z_{L3}\end{cases} \tag{4.57}$$

The continuity of the normal component, $B_r(R_{L2},\theta,z)$, is:

$$\mu_{PM}\frac{\partial\psi}{\partial r}(R_{L2}^+,\theta,z)-\mu_0\frac{\partial\psi}{\partial r}(R_{L2}^-,\theta,z)=0 \tag{4.58}$$

The interface of the permanent magnet and the nonmagnetic exterior medium, $\Sigma_{26}=\Omega_2\cap\Omega_6$, is defined by:

$$\begin{cases}r=R_{L3}\\ \theta_{L1}<\theta<\theta_{L2}\\ Z_{L2}<z<Z_{L3}\end{cases} \tag{4.59}$$

The continuity of the normal component, $B_r(R_{L3},\theta,z)$, is:

$$\mu_{PM}\frac{\partial\psi}{\partial r}(R_{L3}^-,\theta,z)-\mu_0\frac{\partial\psi}{\partial r}(R_{L3}^+,\theta,z)=0 \tag{4.60}$$

4.8 Boundary without magnetic sources

There are three boundary surfaces without sources. The medium around them is nonmagnetic. The boundary conditions on them do no depend on the magnetic field problem.

The internal surface boundary is defined by equation:

$$r=R_{L1} \tag{4.61}$$

On this boundary, the magnetic field is tangential to the boundary:

$$B_r(R_{L1},\theta,z)=0$$

As the medium is nonmagnetic:

$$\frac{\partial\psi}{\partial r}(R_{L1},\theta,z)=0 \tag{4.62}$$

The external surface boundary is defined by equation:

$$r=R_{L4} \tag{4.63}$$

On this boundary, the magnetic field is tangential to the boundary:

$$B_r(R_{L4},\theta,z)=0$$

As the medium is nonmagnetic:

$$\frac{\partial\psi}{\partial r}(R_{L4},\theta,z)=0 \tag{4.64}$$

The bottom surface boundary is defined by equation:

$$z = Z_{L1} \tag{4.65}$$

On this boundary, the magnetic field is tangential to the boundary:

$$B_z(r, \theta, Z_{L1}) = 0$$

As the medium is nonmagnetic:

$$\frac{\partial \psi}{\partial z}(r, \theta, Z_{L1}) = 0 \tag{4.66}$$

4.9 Finite Difference Grid

A 3D grid is applied on the study domain Ω (*Figure 4.3*). This grid is constituted by lines that are parallel to the lines of coordinates. Some of the lines of grid must pass over the lines of boundaries and on the edges of the interfaces of media. The coarsest grid of the study domain is shown on *Figure 4.9*. It contains lines of boundary defined on TABLE 4.II.

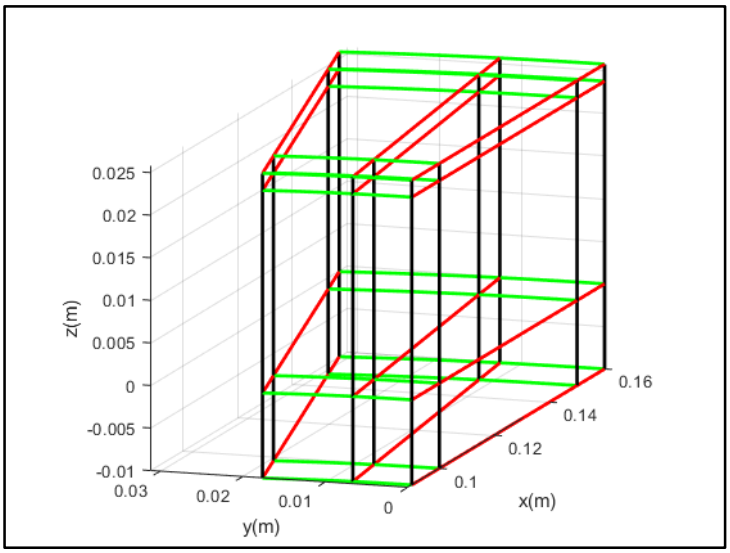

Figure 4-9: Lines of the coarsest grid passing over lines of boundaries and interfaces

By increasing the number of grid lines, the grid like the one shown on *Figure 4.10* is obtained.

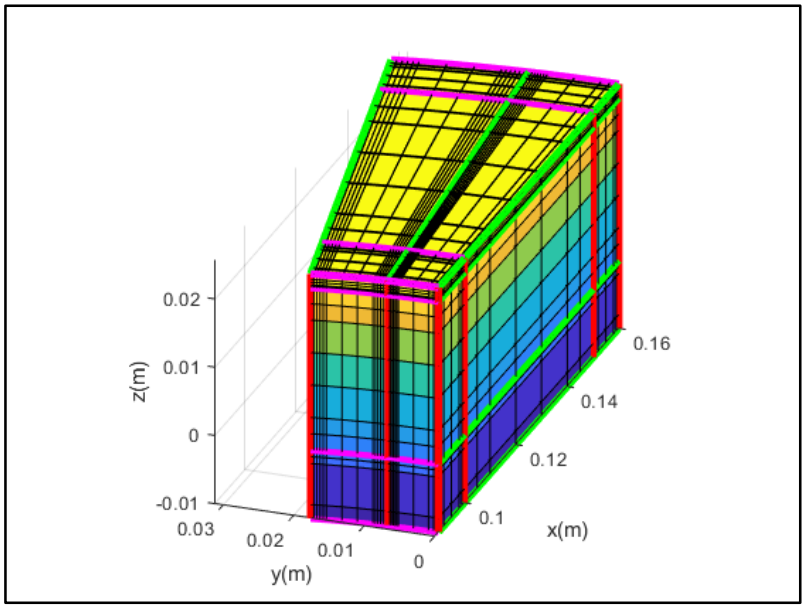

Figure 4-10: Example of grid obtained by increasing the line of the coarsest grid

The lines of the grid of the example on *Figure 4.10* pass through surfaces that are orthogonal to the lines of coordinates. The grid has i_m surfaces orthogonal to the radial lines of coordinates, j_m surfaces orthogonal to the lines of azimuthal coordinates and k_m surfaces orthogonal to the lines of axial coordinates. These surface have the following equation:

$$\begin{cases} r = r_i \quad for\ i = 1, \dots, i_m \\ \theta = \theta_j \quad for\ j = 1, \dots, j_m \\ z = z_k \quad for\ k = 1, \dots, k_m \end{cases} \tag{4.67}$$

For the coarsest grid the surface equations are (see TABLE 4.II):

$$\begin{cases} r = R_{Li} \quad for\ i = 1\ to\ 4 \\ \theta = \theta_{Lj} \quad for\ j = 1\ to\ 3 \\ z = Z_{Lk} \quad for\ k = 1\ to\ 4 \end{cases} \tag{4.68}$$

The grid is also characterized by the distance between two neighboring surfaces:

$$\begin{cases} h_{ri} = r_{i+1} - r_i \quad for\ i = 1, \dots, n_r; \quad where\ n_r = i_m - 1 \\ h_{\theta j} = \theta_{j+1} - \theta_j \quad for\ j = 1, \dots, n_\theta; \quad where\ n_\theta = j_m - 1 \\ h_{zk} = z_{k+1} - z_k \quad for\ k = 1, \dots, n_k; \quad where\ n_z = k_m - 1 \end{cases} \tag{4.69}$$

In indicial numbering, a node is referenced by its indices. The node $P_{i,j,k}$ is the intersection of three orthogonal surfaces defined by its indices and its Cartesian coordinates are:

$$\overrightarrow{OP_{\iota,Jk}} = r_i cos(\theta_j)\overrightarrow{e_x} + r_i sin(\theta_j)\overrightarrow{e_y} + z_k\overrightarrow{e_z} \tag{4.70}$$

The neighboring of node $P_{i,j,k}$ is illustrated on *Figure 4.11*. To simplify the figure legends, the following notation is adopted:

$$\begin{cases} h_i = h_{ri} \\ h_j = h_{\theta j} \\ h_k = h_{zk} \end{cases} \tag{4.71}$$

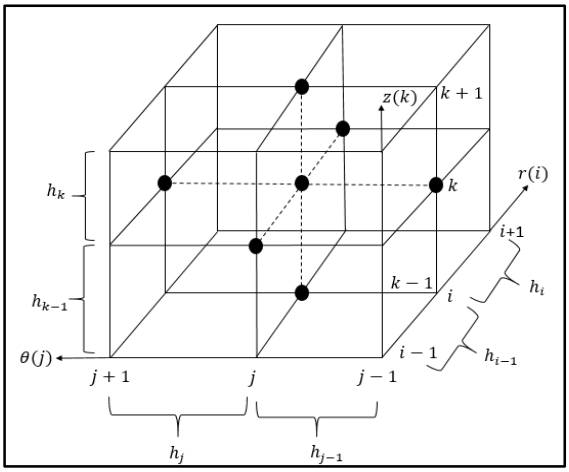

Figure 4-11: Indicial numbering: neighboring of node $P_{i,j,k}$

To develop the finite difference scheme, for the discretization of the Laplacian equation (4.32), a local numbering around the node $P_{i,j,k}$ is defined [49]. *TABLE 4-III* gives the correspondence between the local numbering illustrated on *Figure 4.12* and the global or indicial numbering on *Figure 4.11*.

TABLE 4-III: Local numbering

Local numbering	Indicial numbering
0	(i, j, k)
1	$(i, j+1, k)$
2	$(i+1, j, k)$
3	$(i, j-1, k)$
4	$(i-1, j, k)$
5	$(i, j, k-1)$
6	$(i, j, k+1)$

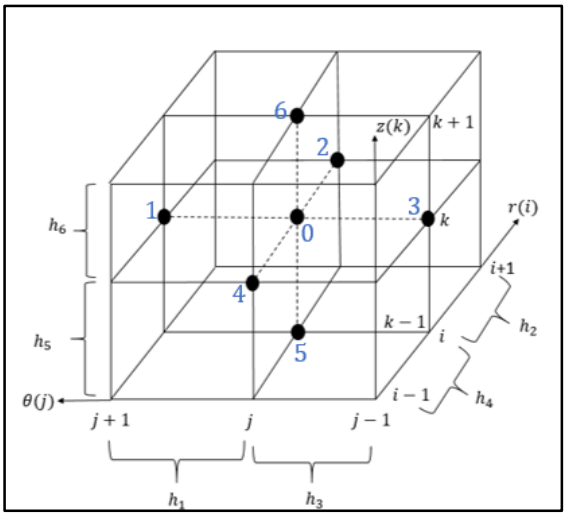

Figure 4-12: Local numbering: neighboring of node $P_0 = P_{i,j,k}$

4.10 Finite difference equations

The magnetic field equation in media, the continuity conditions on interfaces and the boundary conditions are expressed by partial derivative equations (PDE). In this section, these PDE are discretized using the finite difference method based on Taylor's development scheme. The obtained equations are called finite difference equations (FDE).

4.10.1FDE in interior nodes

In this section, the node of interest $P_{i,j,k}$ is neither on an interface nor on a boundary surface. Using (4.69) and the local numbering on *Figure 4.12*, the distances between the neighboring nodes and the interior node P_0 are defined in [ ].

$$\begin{cases} h_1 = \theta_{j+1} - \theta_j \\ h_2 = r_{i+1} - r_i \\ h_3 = \theta_j - \theta_{j-1} \\ h_4 = r_i - r_{i-1} \\ h_5 = z_k - z_{k-1} \\ h_6 = z_{k+1} - z_k \end{cases} \tag{4.72}$$

Using Taylor's development at order two [50], the potential ψ_1 on node P_1 or in indicial numbering $P_{i,j+1,k}$ can be approached by:

$$\psi_1 = \psi_0 + h_1 \left(\frac{\partial \psi}{\partial \theta}\right)_0 + \frac{h_1^2}{2} \left(\frac{\partial^2 \psi}{\partial \theta^2}\right)_0 \tag{4.73}$$

In the same manner, the potential on node P_3 is:

$$\psi_3 = \psi_0 - h_3 \left(\frac{\partial \psi}{\partial \theta}\right)_0 + \frac{h_3^2}{2} \left(\frac{\partial^2 \psi}{\partial \theta^2}\right)_0 \tag{4.74}$$

From (4.53) and (4.54) one may deduce the partial derivatives with respect to θ at P_0 of the potential:

$$\begin{cases} \left(\frac{\partial \psi}{\partial \theta}\right)_0 = \frac{h_1 - h_3}{h_1 h_3} \psi_0 + \frac{h_3}{h_1(h_1+h_3)} \psi_1 - \frac{h_1}{h_3(h_1+h_3)} \psi_3 \\ \left(\frac{\partial^2 \psi}{\partial \theta^2}\right)_0 = -\frac{2}{h_1 h_3} \psi_0 + \frac{2}{h_1(h_1+h_3)} \psi_1 + \frac{2}{h_3(h_1+h_3)} \psi_3 \end{cases} \tag{4.75}$$

In the same manner, the partial derivatives with respect to r at P_0 of the potential are:

$$\begin{cases} \left(\frac{\partial \psi}{\partial r}\right)_0 = \frac{h_2 - h_4}{h_2 h_4} \psi_0 + \frac{h_4}{h_2(h_2+h_4)} \psi_2 - \frac{h_2}{h_4(h_2+h_4)} \psi_4 \\ \left(\frac{\partial^2 \psi}{\partial r^2}\right)_0 = -\frac{2}{h_2 h_4} \psi_0 + \frac{2}{h_2(h_2+h_4)} \psi_2 + \frac{2}{h_4(h_2+h_4)} \psi_4 \end{cases} \tag{4.76}$$

and the partial derivatives with respect to z at P_0 of the potential are:

$$\begin{cases} \left(\frac{\partial \psi}{\partial z}\right)_0 = \frac{h_6 - h_5}{h_6 h_5} \psi_0 - \frac{h_6}{h_6(h_6+h_5)} \psi_5 + \frac{h_5}{h_6(h_6+h_5)} \psi_6 \\ \left(\frac{\partial^2 \psi}{\partial z^2}\right)_0 = -\frac{2}{h_6 h_5} \psi_0 + \frac{2}{h_5(h_6+h_5)} \psi_5 + \frac{2}{h_6(h_5+h_6)} \psi_6 \end{cases} \tag{4.77}$$

The FDE at node P_0, whose radial position is r_0, of PDE (4.32) is :

$$\left(-\frac{2}{h_2h_4}+\frac{1}{r_0}\frac{h_2-h_4}{h_2h_4}-\frac{1}{r_0^2}\frac{2}{h_1h_3}-\frac{2}{h_5h_6}\right)\psi_0+\frac{1}{r_0^2}\frac{2}{h_1(h_1+h_3)}\psi_1+\left(\frac{2}{h_2(h_2+h_4)}+\frac{1}{r_0}\frac{h_4}{h_2(h_2+h_4)}\right)\psi_2+\frac{1}{r_0^2}\frac{2}{h_3(h_1+h_3)}\psi_3+\left(\frac{2}{h_4(h_2+h_4)}-\frac{1}{r_0}\frac{h_2}{h_4(h_2+h_4)}\right)\psi_4+\frac{2}{h_5(h_6+h_5)}\psi_5+\frac{2}{h_6(h_5+h_6)}\psi_6=0 \quad (4.78)$$

4.10.2 FDE on interfaces with the ferromagnetic pole

The node P_0 is on an interface of the ferromagnetic pole with another medium.

The continuity conditions on the interface of the ferromagnetic pole and the airgap is given by (4.44). In the ferromagnetic pole side, the neighboring node of P_0 is P_5. Using the Taylor's development at first order, the potential at P_5 is given by:

$$\psi_5=\psi_0-h_5\left(\frac{\partial\psi}{\partial z}\right)_0^- \quad (4.79)$$

The derivative with respect to z in the ferromagnetic side is then:

$$\frac{\partial\psi}{\partial z}(r,\theta,Z_{L3}^-)=\left(\frac{\partial\psi}{\partial z}\right)_0^-=\frac{\psi_0-\psi_5}{h_5} \quad (4.80)$$

In the same manner, the derivative with respect to z in the airgap side is given by:

$$\frac{\partial\psi}{\partial z}(r,\theta,Z_{L3}^+)=\left(\frac{\partial\psi}{\partial z}\right)_0^+=\frac{\psi_6-\psi_0}{h_6} \quad (4.81)$$

The finite difference equation at node P_0 of the continuity condition at the interface ferromagnetic pole and the airgap is:

$$\left(\frac{\mu_{Fe}}{h_5}+\frac{\mu_0}{h_6}\right)\psi_0-\frac{\mu_{Fe}}{h_5}\psi_5-\frac{\mu_0}{h_6}\psi_6=0 \quad (4.82)$$

The continuity conditions on the interface of the ferromagnetic pole and the nonmagnetic bottom medium is given by (4.46). Using the previous procedure, the derivative with respect to z in the ferromagnetic side is:

$$\frac{\partial\psi}{\partial z}(r,\theta,Z_{L2}^+)=\left(\frac{\partial\psi}{\partial z}\right)_0^+=\frac{\psi_6-\psi_0}{h_6} \quad (4.83)$$

And in the bottom medium side:

$$\frac{\partial\psi}{\partial z}(r,\theta,Z_{L2}^-)=\left(\frac{\partial\psi}{\partial z}\right)_0^-=\frac{\psi_0-\psi_5}{h_5} \quad (4.84)$$

The finite difference equation at node P_0 of the continuity condition at the interface ferromagnetic pole and the bottom medium is:

$$\left(\frac{\mu_{Fe}}{h_6}+\frac{\mu_0}{h_5}\right)\psi_0-\frac{\mu_0}{h_5}\psi_5-\frac{\mu_{Fe}}{h_6}\psi_6=0 \quad (4.85)$$

The finite difference equation at node P_0 of the continuity condition (4.48) at the interface ferromagnetic pole and the interior nonmagnetic medium is:

$$\left(\frac{\mu_{Fe}}{h_2}+\frac{\mu_0}{h_4}\right)\psi_0-\frac{\mu_{Fe}}{h_2}\psi_2-\frac{\mu_0}{h_4}\psi_4=0 \quad (4.86)$$

The finite difference equation at node P_0 of the continuity condition (4.50) at the interface ferromagnetic pole and the exterior nonmagnetic medium is:

$$\left(\frac{\mu_{Fe}}{h_4}+\frac{\mu_0}{h_2}\right)\psi_0-\frac{\mu_0}{h_2}\psi_2-\frac{\mu_{Fe}}{h_4}\psi_4=0 \quad (4.87)$$

4.10.3 FDE on interfaces with the permanent magnet

The finite difference equation at node P_0 of the continuity condition (4.52) at the interface permanent magnet and the ferromagnetic pole is:

$$\left(\frac{\mu_{Fe}}{h_1}+\frac{\mu_{PM}}{h_3}\right)\psi_0-\frac{\mu_{Fe}}{h_1}\psi_1-\frac{\mu_{PM}}{h_3}\psi_3=\mu_{PM}r_0M \tag{4.88}$$

The finite difference equation at node P_0 of the continuity condition (4.54) at the interface permanent magnet and the airgap is:

$$\left(\frac{\mu_0}{h_6}+\frac{\mu_{PM}}{h_5}\right)\psi_0-\frac{\mu_{PM}}{h_5}\psi_5-\frac{\mu_0}{h_6}\psi_6=0 \tag{4.89}$$

The finite difference equation at node P_0 of the continuity condition (4.56) at the interface permanent magnet and the nonmagnetic bottom medium is:

$$\left(\frac{\mu_{PM}}{h_6}+\frac{\mu_0}{h_5}\right)\psi_0-\frac{\mu_0}{h_5}\psi_5-\frac{\mu_{PM}}{h_6}\psi_6=0 \tag{4.90}$$

The finite difference equation at node P_0 of the continuity condition (4.58) at the interface permanent magnet and the nonmagnetic interior medium is:

$$\left(\frac{\mu_{PM}}{h_2}+\frac{\mu_0}{h_4}\right)\psi_0-\frac{\mu_{PM}}{h_2}\psi_2-\frac{\mu_0}{h_4}\psi_4=0 \tag{4.91}$$

The finite difference equation at node P_0 of the continuity condition (4.60) at the interface permanent magnet and the nonmagnetic exterior medium is:

$$\left(\frac{\mu_{PM}}{h_4}+\frac{\mu_0}{h_2}\right)\psi_0-\frac{\mu_0}{h_2}\psi_2-\frac{\mu_{PM}}{h_4}\psi_4=0 \tag{4.92}$$

4.10.4 FDE on boundaries without magnetic sources

The node P_0 is on a surface boundary without magnetic sources.

At the internal surface boundary defined by equation (4.61), the magnetic field is tangential. The derivative with respect to r at point P_0 is approached by:

$$\frac{\partial\psi}{\partial r}(R_{L1},\theta,z)=\left(\frac{\partial\psi}{\partial r}\right)_0^+=\frac{\psi_2-\psi_0}{h_2} \tag{4.93}$$

The boundary condition (4.62) gives the following finite difference equation:

$$\psi_2-\psi_0=0 \tag{4.94}$$

In the same way, the boundary condition (4.64) on the external surface defined by (4.63) gives the following finite difference equation:

$$\psi_4-\psi_0=0 \tag{4.95}$$

The boundary condition (4.66) on the bottom surface defined by (4.64) gives the following finite difference equation:

$$\psi_6-\psi_0=0 \tag{4.96}$$

On the other surface boundary, the boundary conditions depend on the magnetic field problem: open circuit field problem, direct armature reaction field problem or quadrature armature reaction field problem.

4.11 Open circuit magnetic field problem

In the open circuit magnetic field problem, the currents in the winding are null. There are no magnetic sources except the permanent magnets. The study domain can be reduced to a half pole as shown on *Figure 4.3*. All the FDE are as previously presented. This section concerns the boundary conditions on three surfaces.

4.11.1 FDE on stator bore

The internal stator bore is defined by equation:

$$z = Z_{L4} \tag{4.97}$$

As the current are null, there are no surface current density wave on this boundary. The magnetic field is normal to the boundary, so the stator bore is an equipotential surface. On the node P_0 on this surface, the potential is null:

$$\psi_0 = 0 \tag{4.98}$$

4.11.2 FDE on eastern boundary surface

The eastern boundary surface is defined by equation:

$$\theta = \theta_{L1} = 0 \tag{4.99}$$

This surface is a surface of symmetry for the geometry and physical properties. The only magnetic source is the permanent magnet whose magnetization is normal to the surface. So the magnetic field is also normal to this boundary. It is also an equipotential surface. As it has an intersection with the stator bore, the potential is also null and boundary condition (4.98) is applied.

4.11.3 FDE on western boundary surface

The western boundary surface is defined by equation:

$$\theta = \theta_{L3} = \frac{\pi}{2p} \tag{4.100}$$

This surface is a surface of symmetry for the geometry and physical properties. With respect to this surface, the magnetic sources are antisymmetric. So the magnetic field is tangential to this boundary:

$$\frac{\partial \psi}{\partial \theta}(r, \theta_{L3}^{-}, z) = 0 \tag{4.101}$$

As the partial derivative with respect to θ at node P_0 is:

$$\frac{\partial \psi}{\partial \theta}(r, \theta_{L3}^{-}, z) = \left(\frac{\partial \psi}{\partial \theta}\right)_0^{-} = \frac{\psi_0 - \psi_3}{h_3} \tag{4.102}$$

the FDE is:

$$\psi_3 - \psi_0 = 0 \tag{4.103}$$

4.12 Direct armature reaction magnetic field problem

In the direct armature magnetic field problem, the magnetizations of permanent magnet are annulled. There are no magnetic sources except the currents in the stator winding. These currents produced a magnetic field whose axis is parallel to the direct axis i.e. to the axis of the open circuit magnetic field. The study domain can be reduced to a half pole as shown on *Figure 4.3*. All the FDE are as previously presented except that the magnetization M is null in equation (4.88). This section concerns the boundary conditions on three surfaces.

4.12.1 FDE on stator bore

The internal stator bore is defined by equation (4.97). As the current are not null, there is a surface current density wave on this boundary. At the time where the rotor is in the position defined by *Figure 4.3*, the surface current density distribution along the stator bore is of the form:

$$\overrightarrow{K_D}(r,\theta) = K_D(r,\theta)\overrightarrow{e_r} \tag{4.104}$$

The surface current density distribution $K_D(r,\theta)$ is given by (4.22) and shown on *Figure 4.6.*

The boundary condition on stator bore is given by (4.6c) which can be expressed with the partial derivative of the magnetic scalar potential:

$$\frac{\partial \psi}{\partial \theta}(r,\theta,Z_{L4}) = rK_D(r,\theta) \tag{4.105}$$

As the partial derivative with respect to θ at node P_0 is:

$$\frac{\partial \psi}{\partial \theta}(r,\theta,Z_{L4}) = \left(\frac{\partial \psi}{\partial \theta}\right)_0 = \frac{h_1-h_3}{h_1 h_3}\psi_0 + \frac{h_3}{h_1(h_1+h_3)}\psi_1 - \frac{h_1}{h_3(h_1+h_3)}\psi_3 \tag{4.106}$$

On the node P_0 on this surface, the FDE is:

$$\frac{h_1-h_3}{h_1 h_3}\psi_0 + \frac{h_3}{h_1(h_1+h_3)}\psi_1 - \frac{h_1}{h_3(h_1+h_3)}\psi_3 = r_0 K_{D0} \tag{4.107}$$

The radial position of P_0 is r_0 and the value of $K_D(r,\theta)$ at this node is K_{D0}.

4.12.2 FDE on eastern boundary surface

As for the open circuit magnetic field problem, the eastern boundary surface is a surface of symmetry and the magnetic field is normal to it. It is an equipotential surface and the potential is null.

4.12.3 FDE on western boundary surface

As for the open circuit magnetic field problem, the western surface is an antisymmetric surface and FDE (4.103) is applied.

4.13 Quadrature armature reaction magnetic field problem

In the quadrature armature magnetic field problem, the magnetizations of permanent magnets are annulled. The currents produce a magnetic field whose axis is parallel to the quadrature

axis which is materialized by the eastern surface. The study domain can be reduced to a half pole as shown on *Figure 4.3*. All the FDE are as previously presented except that the magnetization M is null in equation (4.88). This section concerns the boundary conditions on three surfaces.

4.13.1 FDE on stator bore

The internal stator bore is defined by equation (4.97). As the current are not null, there is a surface current density wave on this boundary. At the time where the rotor is in the position defined by *Figure 4.3*, the surface current density distribution along the stator bore is of the form:

$$\overrightarrow{K_Q}(r,\theta) = K_Q(r,\theta)\overrightarrow{e_r} \tag{4.108}$$

The surface current density distribution $K_Q(r,\theta)$ is given by (4.23) and shown on *Figure 4.7*. The boundary condition on stator bore is given by (4.6c) which can be expressed with the partial derivative of the magnetic scalar potential:

$$\frac{\partial \psi}{\partial \theta}(r,\theta,Z_{L4}) = rK_Q(r,\theta) \tag{4.109}$$

On the node P_0 on this surface the FDE is:

$$\frac{h_1-h_3}{h_1h_3}\psi_0 + \frac{h_3}{h_1(h_1+h_3)}\psi_1 - \frac{h_1}{h_3(h_1+h_3)}\psi_3 = r_0K_{Q0} \tag{4.110}$$

The radial position of P_0 is r_0 and the value of $K_Q(r,\theta)$ at this node is K_{Q0}.

4.13.2 FDE on eastern boundary surface

The eastern boundary surface is an antisymmetric surface and the magnetic field is tangential to it:

$$\frac{\partial \psi}{\partial \theta}(r,\theta_{L1}^{+},z) = 0 \tag{4.111}$$

The FDE is:

$$\psi_1 - \psi_0 = 0 \tag{4.112}$$

4.13.3 FDE on western boundary surface

The western surface is a symmetric surface. The magnetic field is normal to it. It is an equipotential surface and the potential is null on it.

4.14 3DFDM4STAFPM software

A software has been implemented in Matlab framework by appropriate scripts. The software is called 3D Finite Difference Method for Spoke-Type Axial Flux Permanent Magnet motor (3DFDM4STAFPM). The software is dedicated to one stator-one rotor STAFPM motor. The flowchart of the software is shown on *Figure 4.13*.

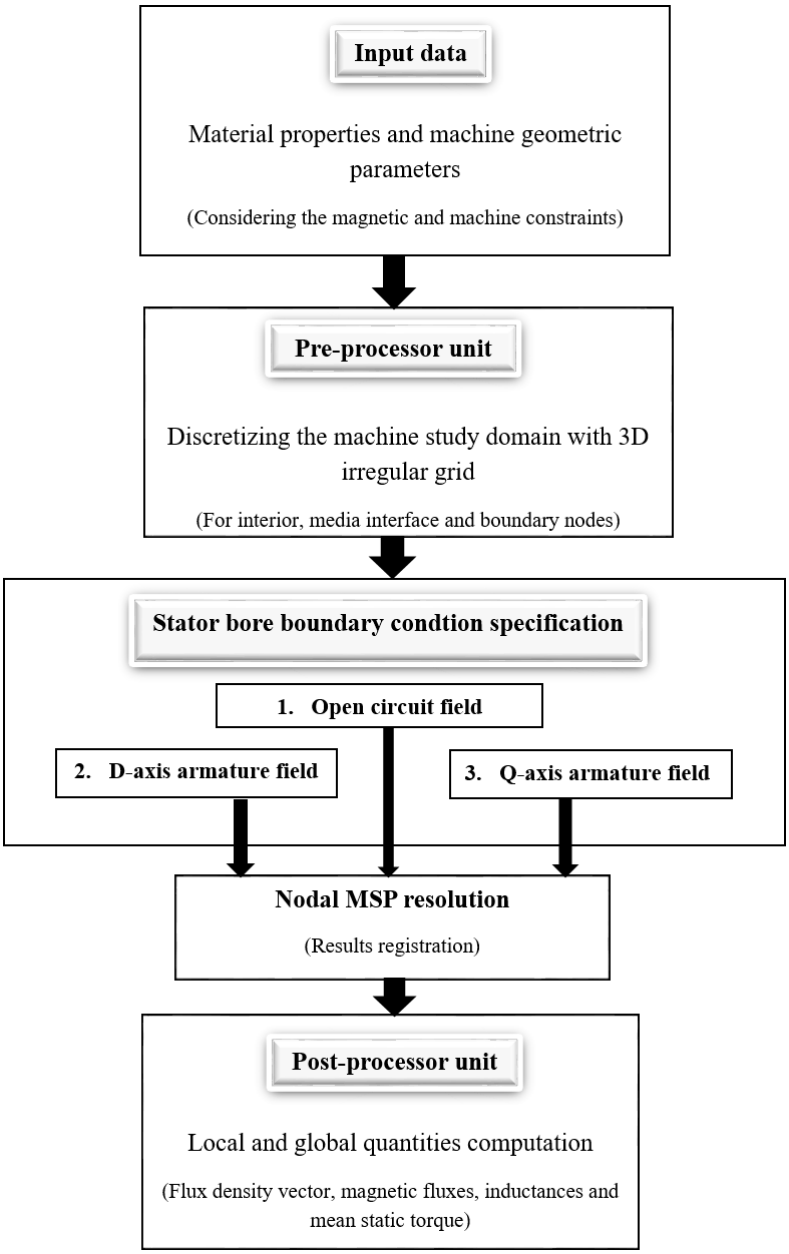

Figure 4-13: Flowchart of the 3DFDM4STAFPM software

4.14.1 Input data

The input data are the data that define the motor and the grid. There are three types of data. The first type of data are the material properties shown in TABLE 4.IV

TABLE 4-IV: Material properties

Permanent magnet polarization	$J(T)$
Permanent magnet relative permeability	μ_{rPM}
Permanent magnet permeability	$\mu_{PM} = \mu_{rPM}\mu_0$
North permanent magnet magnetization	$M(A.m^{-1}) = \frac{J}{\mu_{PM}}$
Ferromagnetic pole relative permeability	μ_{rFe}
Ferromagnetic pole permeability	$\mu_{Fe} = \mu_{rFe}\mu_0$

The second type of data are the geometry parameters of the study domain (TABLE 4.IV.a, b, c).

TABLE 4-V.a: Radial geometry parameters

Internal radius of the study domain	$R_{int}(m)$
Radial thickness of nonmagnetic internal medium	$L_{int}(m)$
Radial thickness of permanent magnet	$L_m(m)$
Radial thickness of nonmagnetic external medium	$L_{ext}(m)$

TABLE 4-V.b: Azimuthal geometry parameters

Number of poles pairs	p
East limit of the study domain	$t_E = 0°$
Angular width of one pole	$t_p = \frac{180°}{p}$
West limit of the study domain	$t_W = \frac{t_p}{2}$
Half angular width of a permanent magnet	$t_a(°)$

TABLE 4-V.c: Axial geometry parameters

Nonmagnetic bottom medium height	$h_{nm}(m)$
Permanent magnet height	$h_m(m)$
Airgap height	$g(m)$

The third type of data concerns the grid. As at the interface between two media a first order Taylor's development is applied, the medium near the interface need to be discretized densely. For that, each medium is divided in three zones along each axis: the zone near the interior limit, the central zone and the zone near the exterior limit. The thickness of the interior and exterior zones is twenty percent of the total thickness along each axis. The step of discretization of the interior and exterior zones are much less than the one of the central zone. It may be seen on *Figure 4.10*.

4.14.2 Pre-processor

The pre-processor processes the input data. The output data are mainly grid data. Visualization tools are at disposal to control the obtained grid. An example of visualization is shown on *Figure 4.9* which shows the coarsest grid made only of the limits of each media along each coordinate axis. An overall 3D view is given on *Figure 4.10*. There are also tools that visualize the grid on surfaces perpendicular to the lines of coordinates. *Figure 4.14* shows a 2D view of the grid in a surface inside the airgap and perpendicular to the z coordinate axis. The traces of the limits of media are in red and blue. It can be seen that near the media limits or near the boundary the grid lines are densified.

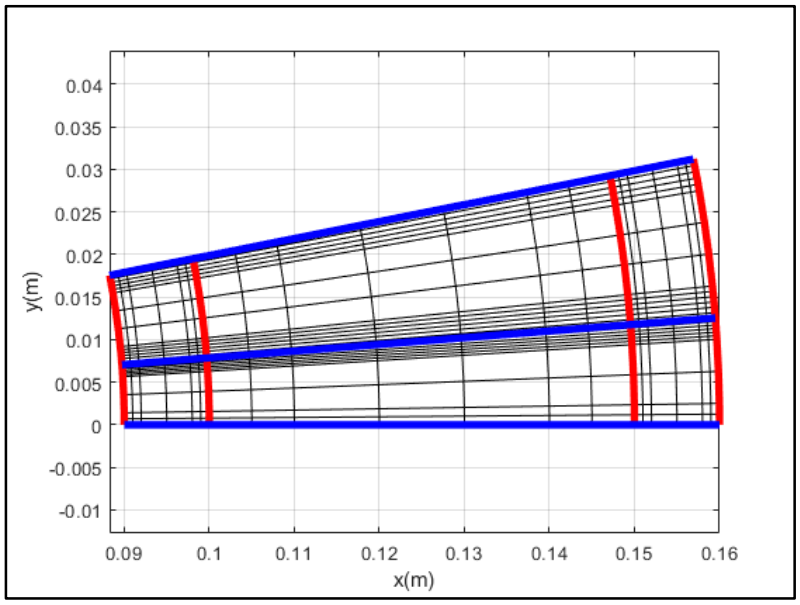

Figure 4-14: 2D view of the grid on a surface inside the airgap

4.14.3 Processor

From the input data and the grid data, the processor unit transforms the partial differential equation into an algebraic system composed by the finite difference equation (FDE) obtained on each node of the grid. It is done for each magnetic field problem: open circuit field problem, direct armature reaction field problem and quadrature reaction field problem (*Figure 4.13*). The obtained algebraic systems are solved with the simplest Matlab common linear solver as the well-known left division operator ($\{x\} = [A]\backslash\{b\}$). The solution obtained is a column matrix that contains the magnetic scalar potential value on each node.

4.14.4 Post-processor

When the value of the magnetic scalar potential is known on each node, it is possible to calculate the local quantities such as the components of the magnetic field intensity $\vec{H}$, those of the magnetic flux density $\vec{B}$ or the global quantities of the magnetic flux through a surface or the phases of the winding. For the sake of simplicity, only the calculations of the local

quantities are presented in this section. The calculation of the flux in the phases of the winding is presented in next section.

The component of the magnetic field intensity can be obtained from second order Taylor's development on interior nodes. On these nodes the first derivatives of the magnetic scalar potential with respect to each coordinates are given by (4.56), (4.57) and (4.58). From (4.8), the component of the magnetic field intensity $\overrightarrow{H_0}$ on an interior node P_0 is given by:

$$\overrightarrow{H_0} = -\left(\frac{\partial \psi}{\partial r}\right)_0 \overrightarrow{e_r} - \frac{1}{r}\left(\frac{\partial \psi}{\partial \theta}\right)_0 \overrightarrow{e_\theta} - \left(\frac{\partial \psi}{\partial z}\right)_0 \overrightarrow{e_z} \qquad (4.113)$$

In each media, the magnetic flux density on interior nodes is calculated using the constitutive law (4.2). The distribution of the local quantities may be visualized inside the study domain. The distribution of magnetic flux density inside all the study domain of the open circuit magnetic field problem is shown on *Figure 4.15*. It can be seen that the main flow of the magnetic flux goes from the eastern boundary to the stator bore and crossing the permanent magnet.

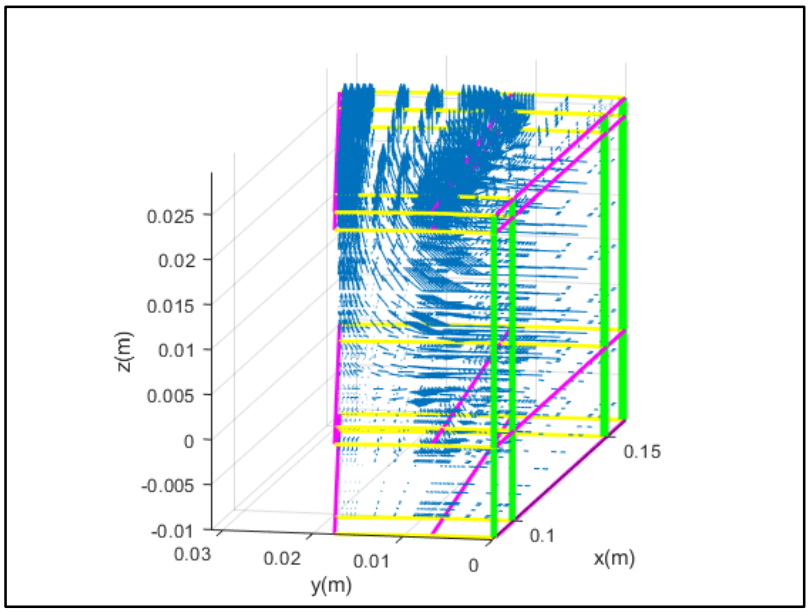

Figure 4-15: Distribution of the open circuit magnetic flux density inside the all study domain

To qualitatively control the armature reaction fields, the magnetic flux densities of the direct and quadrature reaction fields on surface with constant radial position are shown respectively on *Figure 4.16* and *Figure 4.17*. The surface is taken in the middle radial position of the permanent magnet.

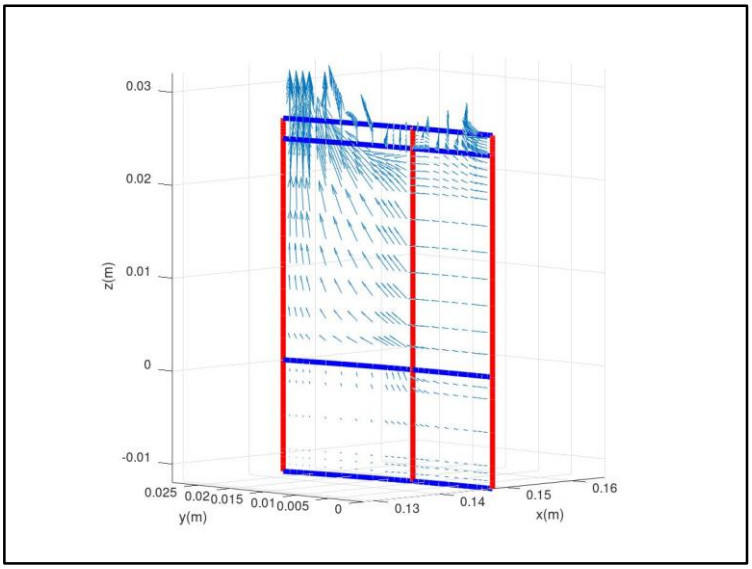

Figure 4-16: Distribution of the direct armature reaction magnetic flux density inside a surface

On *Figure 4.16* it can be seen that the main flow of the magnetic flux goes from the eastern boundary to the stator bore as for the open circuit field and on *Figure 4.17*, the main flow goes from western boundary to the stator bore but does not cross the permanent magnet.

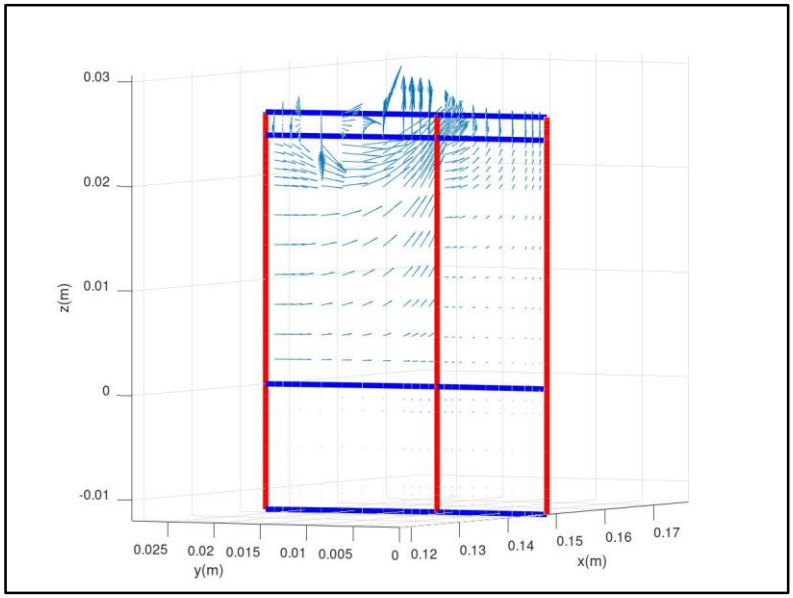

Figure 4-17: Distribution of the quadrature armature reaction magnetic flux density inside a surface

4.15 Flux model of integer distributed winding

The experimental studies undertaken in Chapter 3 have shown that the torque, the direct no-load flux density, the direct and quadrature armature reaction inductances in function of the rotor position have ripples. The mean values of the direct no-load flux density, the direct and quadrature armature reaction inductances give the mean torque following the DQ model.

In the 3D Finite Difference Sizing Model presented in this chapter many assumptions and simplifications have been adopted in order to speed up the calculation of the no-load magnetic field and the armature reaction magnetic fields. In this section, an original method of calculation of the magnetic flux in the phases of the winding stator is presented followed by the DQ model parameters which are compared to those deduced from measurement for the STAFPM prototype.

4.15.1 Elementary flux

According to the assumptions of the sizing model, the no-load and direct armature reaction magnetic flux density on the stator bore surface is axial:

$$\vec{B}(r,\theta) = B_z(r,\theta)\vec{e_z} \tag{4.114}$$

The linear distribution conductor function is expressed by (4.15) for phase k.

An elemental surface $dS(r,\theta)$ is defined with a radial length dr and with an angular width $\frac{\pi}{p}$ situated between two angular positions, $\theta - \frac{\pi}{p}$ and θ, on the stator bore as shown in *Figure 4.18.*

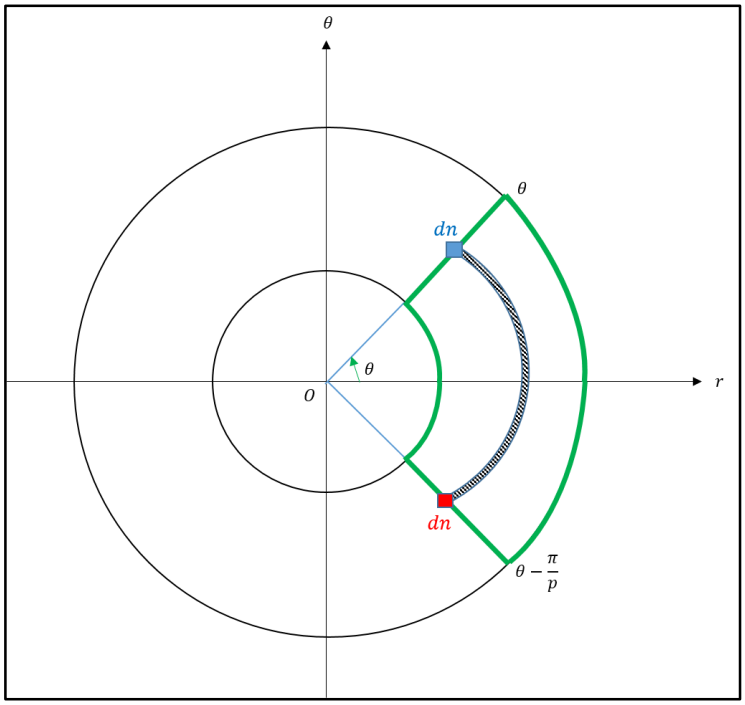

Figure 4-18: Elementary surface on the stator bore

The elementary magnetic flux, $d\varphi(r,\theta)$, crossing the elemental surface is given by:

$$d\varphi(r,\theta) = \iint_{dS(r,\theta)} \vec{B}.\overrightarrow{dS} = \iint_{dS(r,\theta)} B_z.rdrd\theta \tag{4.115}$$

It is convenient, for the following, to define the derivative:

$$\frac{d\varphi}{dr}(r,\theta) = r\int_{\theta-\frac{\pi}{p}}^{\theta} B_z(r,\theta)d\theta \tag{4.116}$$

4.15.2 Flux in one phase

As shown from *Figure 4.18* and [52], the number of "return" conductors at specific position (r, θ) is given by:

$$dn(r,\theta) = -C_k(r,\theta) r dr d\theta \tag{4.117a}$$

and at the position $(r, \theta - \frac{\pi}{p})$ the number of "go" conductors is :

$$dn\left(r, \theta - \frac{\pi}{p}\right) = C_k(r,\theta) r dr d\theta \tag{4.117b}$$

The elementary flux captured by one phase is thus:

$$d\varphi_{vk} = C_k(r,\theta) \frac{d\varphi}{dr}(r,\theta) r dr d\theta \tag{4.118}$$

By summing up the elementary fluxes all over phase k, the total flux is:

$$\varphi_k = p \int_{R_{L1}}^{R_{L2}} \int_{\frac{-\pi}{2p}}^{\frac{\pi}{2p}} C_k(r,\theta) \frac{d\varphi}{dr}(r,\theta) r dr d\theta \tag{4.119}$$

4.15.3 No-load and direct armature flux

The angular position $\theta_R^m$of the rotor in the study domain (*Figure 4.3*) is the reference position because the axis of the rotor, axis 'D', is facing the axis of phase 1:

$$\theta_R^m = 0$$

According to symmetries of the study domain defined in *Figure 4.3*, in this rotor position, the axial flux density for the no-load and direct armature reaction can be decomposed in Fourier series, of the form:

$$B_z(r,\theta,0) = \sum_{m=1}^{\infty} b_m(r) \sin((2m-1)p\theta) \tag{4.120}$$

If the rotor is moving at another position different from the reference position, the axial flux density is:

$$B_z(r,\theta,\theta_R^m) = B_z(r,\theta-\theta_R^m,0) = \sum_{m=1}^{\infty} b_m(r) \sin((2m-1)p(\theta - \theta_R^m)) \tag{4.121}$$

From (4.116) and (4.121), the elementary flux depends also on the rotor position:

$$\frac{d\varphi}{dr}(r,\theta,\theta_R^m) = \sum_{m=1}^{\infty} -\frac{2r b_m(r)}{(2m-1)p} cos((2m-1)p(\theta - \theta_R^m)) \tag{4.122}$$

From (4.15) and (4.121), for phase 1, the product in the flux (4.119) becomes:

$$\int_{\frac{-\pi}{2p}}^{\frac{\pi}{2p}} C_1(r,\theta) \frac{d\varphi}{dr}(r,\theta)\, r d\theta = \sum_{m=1}^{\infty}\sum_{n=1}^{\infty} \frac{-2r^2 b_m(r) a_n(r)}{(2m-1)p} \int_{\frac{-\pi}{2p}}^{\frac{\pi}{2p}} cos\big((2n-1)p\theta\big) cos\big((2m-1)p(\theta - \theta_R^m)\big) d\theta \tag{4.123}$$

The integral in the second member of (4.123) is decomposed in two integrals:

$$\int_{\frac{-\pi}{2p}}^{\frac{\pi}{2p}} cos\big((2m-1)p(\theta-\theta_R^m)\big) cos\big((2n-1)p\theta\big) d\theta = \frac{1}{2}\left(\int_{\frac{-\pi}{2p}}^{\frac{\pi}{2p}} cos(2(m+n-1)p\theta - (2m-1)p\theta_R^m) d\theta + \int_{\frac{-\pi}{2p}}^{\frac{\pi}{2p}} cos(2(m-n)p\theta - (2m-1)p\theta_R^m) d\theta \right) \tag{4.124}$$

The first integral of the second member of (4.124) is null, the second is not null if $m = n$:

$$\int_{\frac{-\pi}{2p}}^{\frac{\pi}{2p}} C_1(r,\theta) \frac{d\varphi}{dr}(r,\theta,\theta_R^m) r d\theta = \sum_{n=1}^{\infty} -\frac{2r^2 a_n(r) b_n(r)}{(2n-1)p} \frac{\pi}{2p} cos((2n-1)p\theta_R^m) \tag{4.125}$$

From (4.119) and (4.125), for the no-load and direct armature reaction fields, the magnetic flux of phase k in function of the rotor position is given by:

$$\varphi_k(\theta_R) = \sum_{n=1}^{\infty} -cos\left((2n-1)\left(p\theta_R^m - (k-1)\frac{2\pi}{3}\right)\right)\int_{R_{L1}}^{R_{L2}} \frac{a_n(r)b_n(r)r^2}{(2n-1)}\frac{\pi}{p}dr \qquad (4.126)$$

4.15.4 Quadrature armature reaction flux

According to symmetries of the study domain defined in *Figure 4.3*, in this rotor position, the axial flux density for the quadrature armature reaction can be decomposed in Fourier series, of the form:

$$B_z(r,\theta,0) = \sum_{m=1}^{\infty} b_m(r)\, cos((2m-1)p\theta) \qquad (4.127)$$

If the rotor is moving at another position different from the reference position, the axial flux density is:

$$B_z(r,\theta,\theta_R^m) = B_z(r,\theta-\theta_R^m,0) = \sum_{m=1}^{\infty} b_m(r)\, cos((2m-1)p(\theta-\ \theta_R^m)) \qquad (4.128)$$

From (4.128), for phase 1, the product in the flux (4.119) becomes:

$$\int_{-\frac{\pi}{2p}}^{\frac{\pi}{2p}} C_1(r,\theta)\frac{d\varphi}{dr}(r,\theta)\, rd\theta = \sum_{m=1}^{\infty}\sum_{n=1}^{\infty}\frac{2r^2 b_m(r)a_n(r)}{(2m-1)p}\int_{-\frac{\pi}{2p}}^{\frac{\pi}{2p}} cos\big((2n-1)p\theta\big)sin\big((2m-1)p(\theta-\ \theta_R^m)\big)d\theta \qquad (4.129)$$

The integral in the second member of (4.129) is decomposed in two integrals:

$$\int_{-\frac{\pi}{2p}}^{\frac{\pi}{2p}} sin\big((2m-1)p(\theta-\theta_R^m)\big)cos\big((2n-1)p\theta\big)d\theta = \frac{1}{2}\left(\int_{-\frac{\pi}{2p}}^{\frac{\pi}{2p}} sin(2(m+n-1)p\theta - (2m-1)p\theta_R^m)d\theta + \int_{-\frac{\pi}{2p}}^{\frac{\pi}{2p}} sin(2(m-n)p\theta-(2m-1)p\theta_R^m)d\theta\right) \qquad (4.130)$$

The first integral of the second member of (4.97) is null, the second is not null if $m = n$:

$$\int_{\frac{-\pi}{2p}}^{\frac{\pi}{2p}} C_1(r,\theta)\frac{d\varphi}{dr}(r,\theta,\theta_R^m)rd\theta = \sum_{n=1}^{\infty}\frac{2r^2 a_n(r)b_n(r)}{(2n-1)p}\frac{\pi}{2p}sin((2n-1)p\theta_R^m) \qquad (4.131)$$

From (4.131) and (4.119), for the quadrature armature reaction fields, the magnetic flux of phase k in function of the rotor position is given by:

$$\varphi_k(\theta_R^m) = \sum_{n=1}^{\infty} sin\left((2n-1)\left(p\theta_R^m - (k-1)\frac{2\pi}{3}\right)\right)\int_{R_{L1}}^{R_{L2}}\frac{a_n(r)b_n(r)r^2}{(2n-1)}\frac{\pi}{p}dr \qquad (4.132)$$

4.16 DQ model parameters

For the three magnetic field problems, the following steps are needed to calculate DQ model parameters with the 3DFDM4STAFPM software:

- Calculate the distribution of the axial magnetic flux density on the stator bore
- Calculate the flux in the three phases in function of the rotor position
- Use Park's transformation to calculate the DQ model parameters

4.16.1 Distribution of the axial magnetic flux density on stator bore

The 3DFDM4STAFPM software calculate the field on a reduced domain. The distribution of the axial magnetic flux density on the stator (half pole) for the no-load field is shown on *Figure 4.19.*

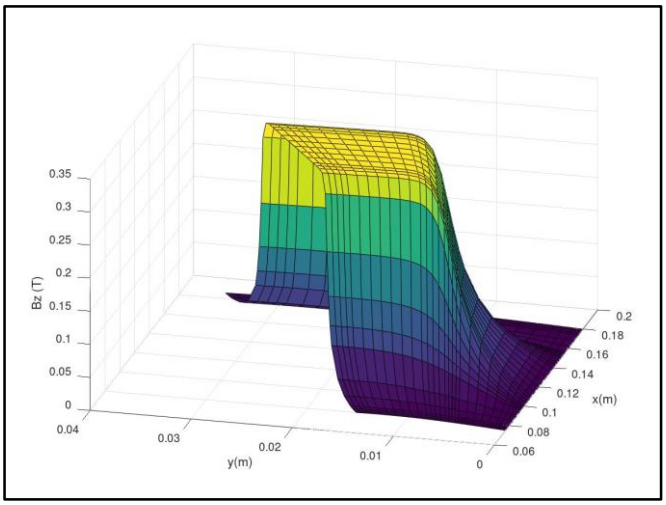

Figure 4-19: $B_z(r, \theta, z = h_m + g)$ on the stator for the no-load magnetic flux problem

For the armature reaction field problems, the distribution of the surface current density is first calculated. Its distribution on the stator bore across one pair of poles is shown on *Figure 4.7* and *Figure 4.8.* To calculate the magnetic field, these distributions must be applied on the stator bore of the reduced and discretized study domain shown in *Figure 4.20.* The azimuthal axis is discretized in 27 irregular intervals on half pole. Spanning on one pair of poles, there are 108 intervals. As the distributions of the surface current density have sharp fronts (*Figure 4.7* and *Figure 4.8),* applying Shannon's rule, only 18 azimuthal odd harmonics are taken into account to avoid noises. With 18 harmonics, the direct and quadrature armature surface current density distributions on half pole of the stator bore are shown on *Figure 4.20* and *Figure 4.21* respectively.

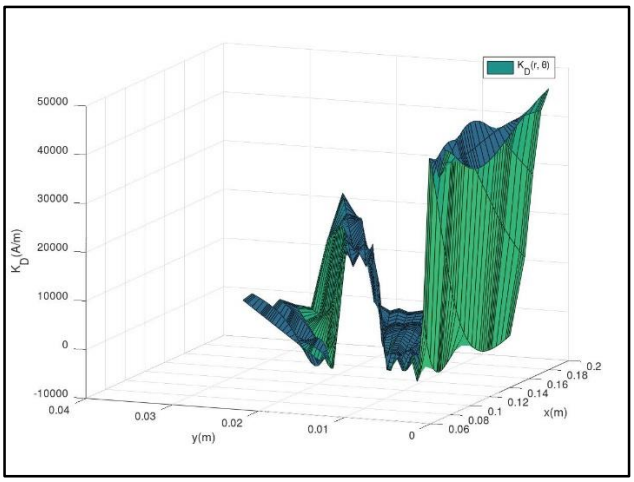

Figure 4-20: Distribution of the direct armature surface current density on the reduced domain

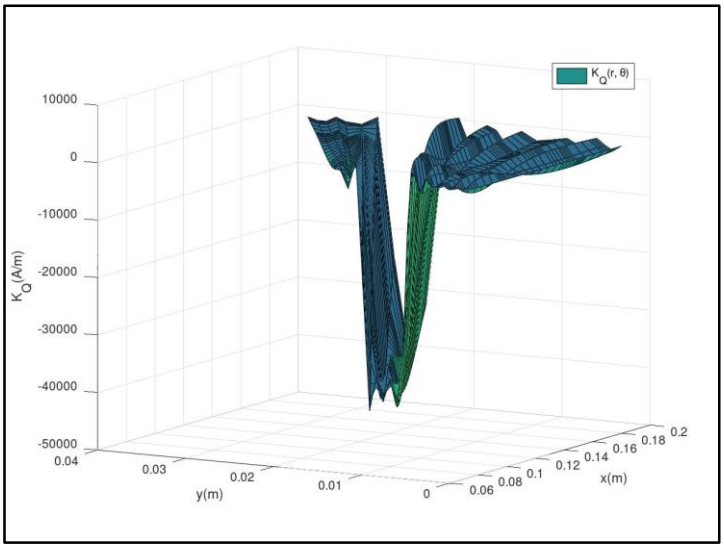

Figure 4-21: Distribution of the quadrature armature surface current density on the reduced domain

The distributions of the armature axial flux densities on the stator bore of the reduced domain are shown on *Figure 4.22* and *Figure 4.23*.

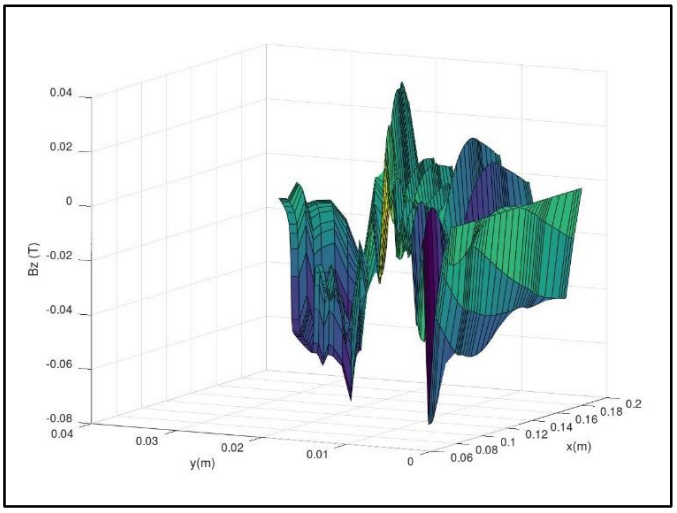

Figure 4-22: Direct armature axial flux density distribution on the reduced domain stator bore

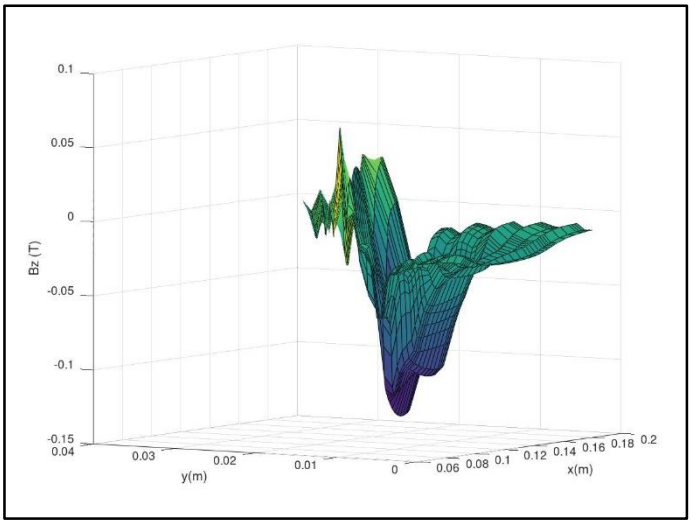

Figure 4-23: Quadrature armature axial flux density distribution on the reduced stator bore

Before computing the harmonics of these two distributions [51], they have to be spanned along one pair of poles as shown in (*Figure 4.24* and *Figure 4.25*).

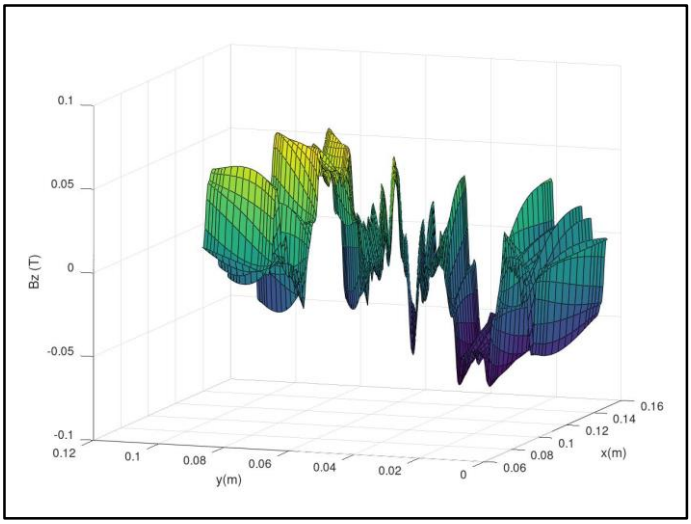

Figure 4-24: Spanning on pair of poles the direct armature axial flux density distribution

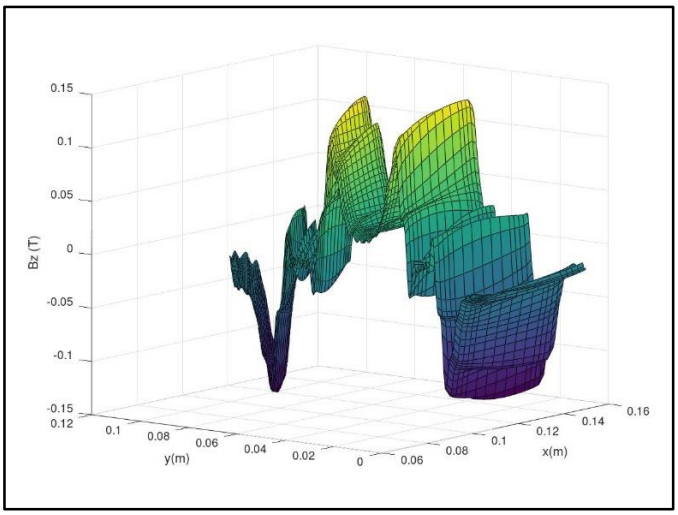

Figure 4-25: Spanning on pair of poles the quadrature armature axial flux density distribution

4.16.2 Flux in function of the rotor position

According to section 4.15, the harmonics of the axial flux densities (4.120) and (4.127) are calculated. The flux in function of the rotor position are shown on *Figure 4.2*6 to *Figure 4.28* for the no-load field, direct and quadrature armature reaction fields respectively.

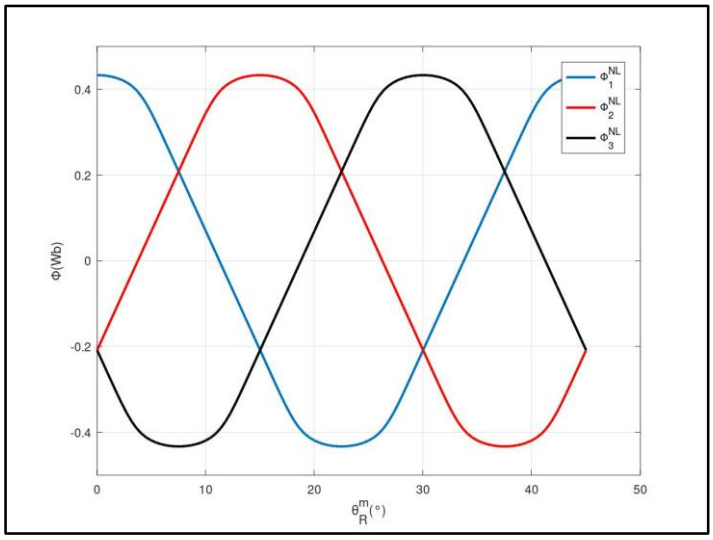

Figure 4-26: Flux in function of the rotor position from the no-load magnetic field

The no-load magnetic flux should be compared to *Figure 3-43* of Chapter 3 which shows the no-load magnetic flux deduced from the measurements. The waveforms of the calculated and measured magnetic flux are very similar. The relative error on the magnitude is quite acceptable during the sizing procedure.

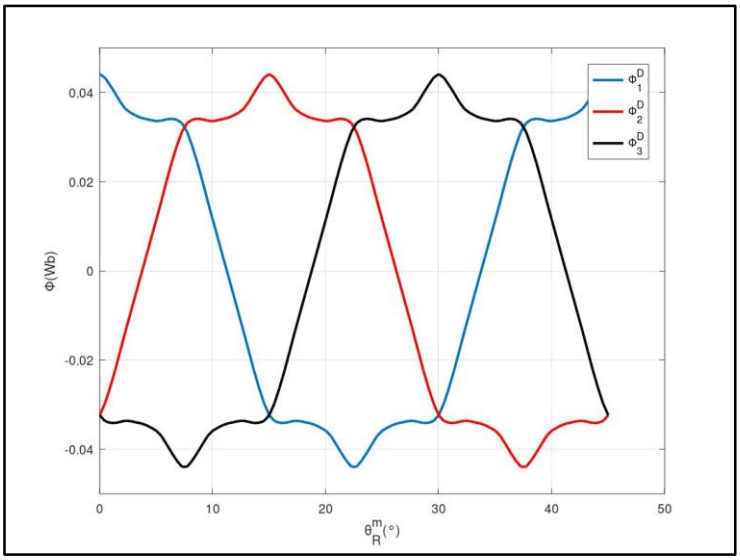

Figure 4-27: Flux in function of the rotor position from the direct armature reaction magnetic field

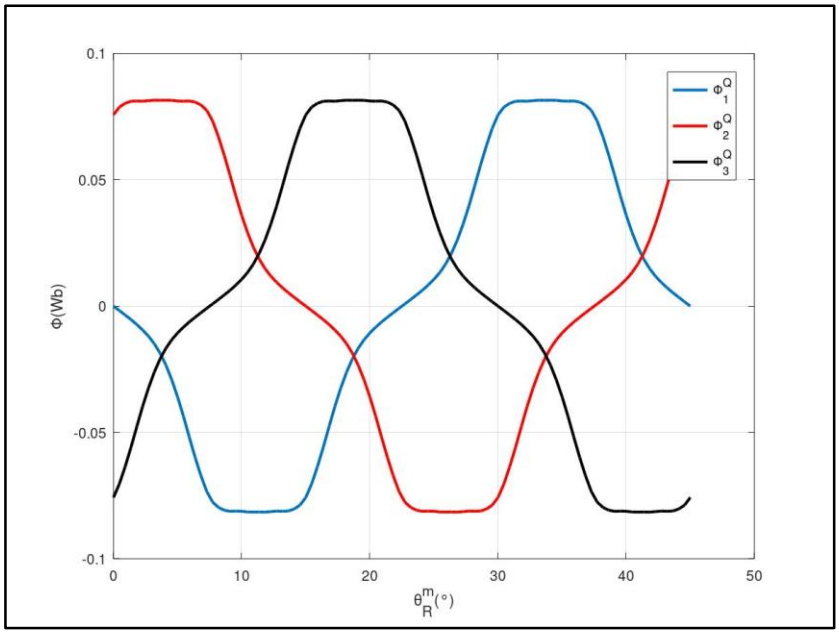

Figure 4-28: Flux in function of the rotor position from the quadrature armature reaction magnetic field

Direct and quadrature armature flux deduced from measurements are not shown but they have been calculated. The waveforms and the levels of the measured reaction flux are very different from those of the calculated reaction flux. This huge difference can be explained by the fact the model of flux does not take into account slot and head winding inductances.

4.16.3 Park's transformation

Park's transformation in section (3.70) has been applied to the calculated flux. The results are shown on *Figure 4.29* to *Figure 4.31*.

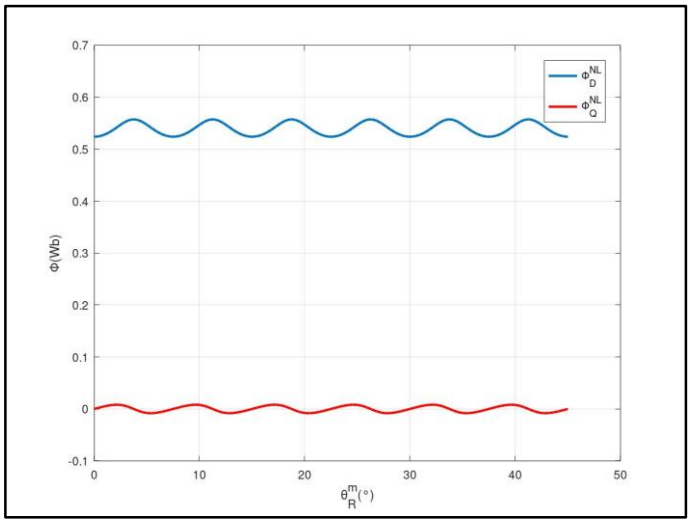

Figure 4-29: DQ components of the no-load flux in function of the rotor position

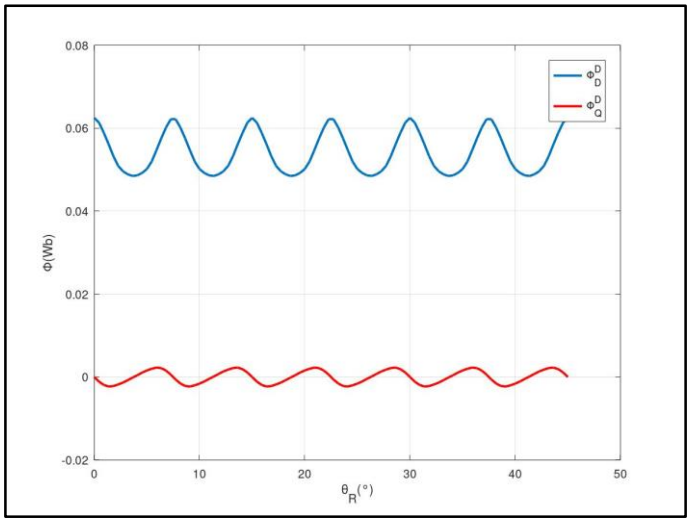

Figure 4-30: DQ components of the direct armature reaction flux in function of the rotor position

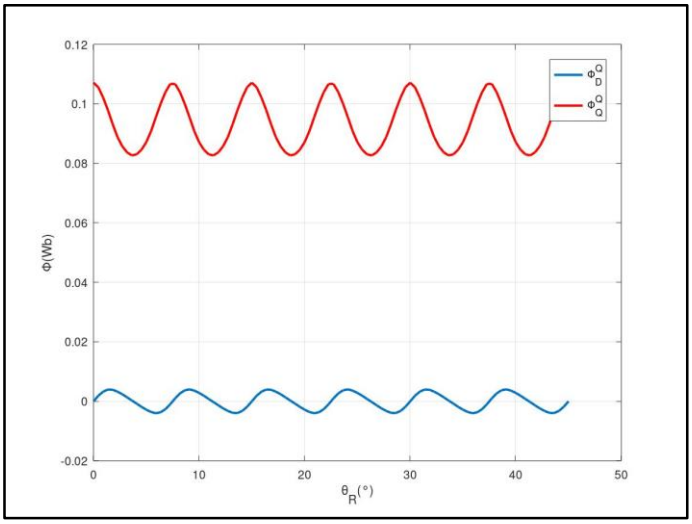

Figure 4-31: DQ components of the quadrature armature reaction flux in function of the rotor position

From the mean value of the DQ components of the fluxes, the DQ model parameters are calculated and compared to the ones deduced from measurements in TABLE 4.V

TABLE 4-VI: Comparison of the DQ model parameters

	Calculated	Measured	Relative error (%)
Direct no-load flux, $\Phi_{vD}(Wb)$	0.54	0.57	5.3
Direct inductance, $L_D(mH)$	20.9	48.5	56.9
Quadrature inductance, $L_Q(mH)$	36.1	61.9	41.9
$L_Q - L_D(mH)$	15.2	13.4	13.4

From TABLE 4. V, it can be seen that the no-load flux density is calculated with very small error. The values of the calculated inductances differ a lot from the values deduced from measurements. The relative error of the difference between the quadrature and direct

inductances is acceptable in a sizing procedure. It is important as the torque is given by (3.76) in Chapter 3.

The procedure to calculate the optimal torque from the DQ model parameters is presented in Chapter 3 section 3.13.2. Figure 4.32 shows the mean torque in function of the phase shift α between the current and the rotor.

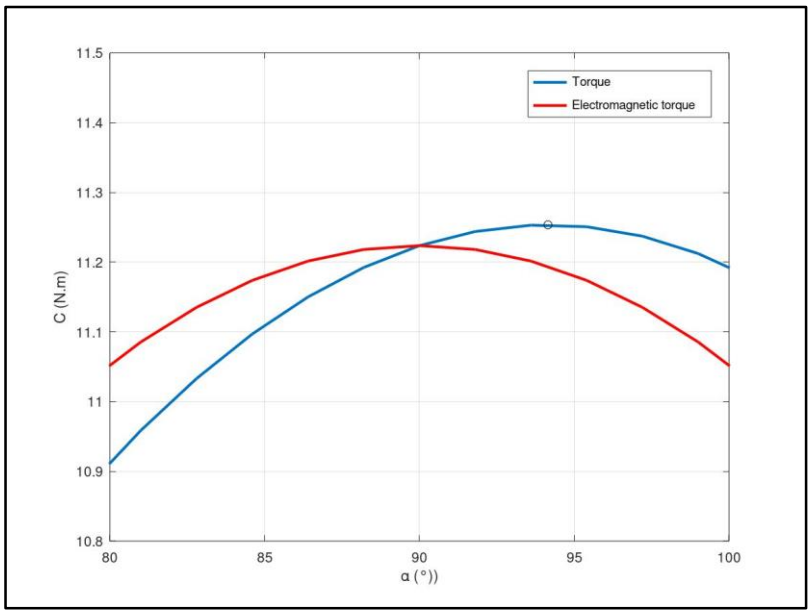

Figure 4-32: Torque versus phase shift α

The calculated value of the optimal torque is 11.25 N.m. The relative error from the value deduced from measurements is six percent which is quite acceptable in a sizing procedure.

4.17 Conclusion

In this chapter, a sizing model of STAFPM based on 3D magnetic field is proposed. Due to ferromagnetic poles, simple analytical models of the magnetic field do not exist up to now. A 3D numerical model of the magnetic field based on finite difference method is chosen. To speed up the computation all the symmetries of the motor have been taken into account and the study domain is reduced to a half pole. As for the analytical models of RFM and AFM surface mounted permanent magnet motor, the stator is taken into account by the distribution function of conductors and the distribution of surface current density along the stator bore.

Three magnetic field problems are solved: open circuit magnetic field problem, direct and quadrature reaction magnetic field problems. To solve these problems a magnetic scalar potential formulation is chosen.

An original method of calculation of the fluxes is developed. This method fits well with the magnetic scalar potential formulation. This method allows to calculate the flux in function of the rotor position for the three magnetic field problems. The open-circuit flux waveforms and magnitudes fit well with the ones deduced from measurements. Due to several assumptions done in the calculation of the armature reaction fields, the direct and quadrature flux waveforms do not match the ones deduced from measurements. These remarks apply also when Park's transformation is used to deduce the DQ model parameters from the flux waveforms.

The value of torque deduced from the calculated DQ model parameters is nevertheless quite acceptable. The relative error is six percent which is quite acceptable in a sizing procedure.

General conclusion

Spoke Type Axial Flux Permanent Magnet (STAFPM) motors are interesting due to their potentiality to concentrate the no-load magnetic flux produced by magnets in the airgap. This feature allows the use of Ferrite magnets instead of rare earth based magnets. The work is devoted to develop 3D magnetic field models to be associated to sizing procedure of Spoke Type Axial Flux Permanent Magnet (STAFPM) motor.

In the first chapter, a bibliographical study reviews the analytical magnetic field models for Surface Mounted Radial Flux Permanent Magnet (SMRFPM) and Surface Mounted Axial Flux Permanent Magnet (SMAFPM) motors. Taking into account the difficulties to adapt these analytical models to salient pole motors, 3D numerical magnetic field models to be associated to sizing equations are proposed for STAFPM motor. Then a state of the art on the test benchmarks, for salient pole motors, leads to propose the experimental identifications of the parameters of the general electromechanical model of electric motors from static torque measurements.

The second chapter is focused on the sizing approach to realize a STAFPM prototype. First a 1D mean radius analytical model of the magnetic field associated to sizing equations helps to calculate the thermal and magnetic theoretical loads of an existing SMAFPM motor. These loads are taken as references for the STAFPM prototype. The sizing procedure is also applied to compare, on the electromagnetic torque basis, SMAFPM and STAFPM motors which have the same stator. At our knowledge, it is the first time that surface mounted and spoke type permanent magnet motors are compared on the same basis. Indeed, it is often taken for granted that it is better to use spoke type Ferrite magnet motor than surface mounted Ferrite magnet motor. The comparison shows that it is not so simple. From the conclusions of this comparison and taking into account experimental constraints, a STAFPM prototype for the experimental studies in Chapter 3 is sized.

In Chapter 3, an original method to identify, in function of the rotor position, the main parameters of the general electromechanical model of electric motors is explained. These identifications are based on the measurements of static torques in function of the rotor position. Once the parameters identified, the electromechanical model provides quick computations of the static torque of the motor. These computations reproduce accurately in details the static torque waveforms measured on the test bench for different types of supply currents. Eventually, from the identified parameters, the DQ model parameters are calculated in function of the rotor position. It is shown that these parameters do have ripples. Their mean values allow to obtain the mean torque when the motor is supplied by sinusoidal currents.

In Chapter 4, a tool, based on 3D finite difference method, is developed in the MATLAB® environment. This tool is entitled “3DFDM4STAFPM”. This tool solves the open-circuit magnetic field problem, direct and quadrature armature reaction magnetic field problems by means of the magnetic scalar potential formulation. To speed up the calculation times needed to solve these problems, the study domain is reduced to a half pole.
The stator is modeled by the distribution function of conductors and the surface current densities. An original method for the calculations of the magnetic flux is set up. Indeed, the context of 3D finite difference method associated to the magnetic scalar potential formulation and the representation of stator by the distribution functions of conductors and surface current density is new. The state of art does not provide any available flux calculation method. By the

help of the flux calculation method, it is possible to calculate the no-load magnetic flux waveforms in function of the rotor position, the direct and quadrature armature reaction inductances of the DQ model. The no-load flux waveforms agree very well with those deduced from e.m.f measurements performed in Chapter 3. The values of the direct and quadrature inductances are very different from the mean values of these inductances deduced from the static torque measurements. These differences can be explained by the fact that the numerical magnetic field model takes only into account the airgap inductances. The inductances due to slots and to the winding heads must be added to the airgap inductances. The calculation of slot and winding head inductances are very well known. Nevertheless, the mean torque obtained from the DQ model using the calculated parameters is very close to the mean torque deduced from measurements. Furthermore, the optimal torques per ampere calculated from model and measurement results agree very well.
The good matching of the calculation and measurement results proofs the validity of the developed 3D numerical tool. Indeed, this tool seems to be very efficient considering the strong assumptions that have been taken to reduce the computation time.

The tool as it is, can take into account single rotor single stator topology but also double rotor and single stator topology.
A second version of the tool considering the double stator 'STAFPM' topology is very easy to set up. The study domain of a double stator single rotor topology is less complex because the air region at the bottom of the rotor can be removed and replaced by a simple boundary condition. A comparative study can then be performed between the single stator single rotor, double rotor single stator and double stator single rotor topologies.
The measurement results show that the torques do have ripples. Knowing the parameters of the general electromechanical model of the STAFPM motors, it is possible to optimize the supply currents to reduce or eliminate these ripples.
The developed tool can be applied to optimize the saliency and electromagnetic torques. This is possible because the difference between the quadrature and direct inductances is calculated with enough accuracy by the tool.

References

[1] A. Chebak, "*Modélisation, conception et optimisation des machines sans encoches à aimants permanents à haute vitesse*", Thèse de l'Université Laval, Québec, 2013.

[2] B. Nogarède, "*Étude de moteurs sans encoches aimants permanents de forte puissance à basse vitesse"*, Thèse de l'Institut National Polytechnique -Toulouse, France, 1990.

[3] T. Carpi, "*Modèles 3D hybrides pour les machines électriques",* Thèse de l'Institut National Polytechnique -Toulouse, France, 2021.

[4] V. B. Honsinger, "*Sizing equations for electric machinery*", IEEE Transactions on Energy Conversion, Vol EC-2, n°1, March 1987.

[5] G. R. Slemon, "*On the design of high-performance surface-mounted PM motors*", IEEE Transactions on Industry Applications, vol. 30, n°1, January/February 1994.

[6] S. Huang, J. Luo, F. Leonardi and T. A. Lipo, "*A general approach to sizing and power density equations to compare electrical machines",* IEEE Transactions on Industry Applications, vol. 34, n°1, January/February 1998.

[7] C. C. Chan, "*Axial-field electrical machines - Design and applications",* IEEE Transactions on Energy Conversion, Vol EC-2, n°2, June 1987.

[8] S. Huang, J. Luo, F. Leonardi and T. A. Lipo, "*A comparison of power density for axial flux machines based on general purpose sizing equations",* IEEE Transactions on Energy Conversion, vol. 14, n°2, June 1999.

[9] S. T. Vun and M. D. McCullogh, "*Optimal design method for large-scale YASA machines",* IEEE Transactions on Energy Conversion, vol. 30, n°3, June 2015.

[10] Y. Lefevre, S. El Aabid, J. F. Llibre, C. Henaux and S. Touhami, "*Performance assessment tool based on loadability concepts*", International Journal of Applied Electromagnetics and Mechanics, vol. 59, no. 2, pp. 687-694, 2019.

[11] S. Touhami, Y. Lefevre and J. F. Llibre, "*Joint Design of Halbach. Segmented Array and Distributed Stator Winding*", 13th International Conference on Electrical Machines (ICEM) pp. 2497-2503, Alexandroupoli, Greece, 3 - 6 September 2018.

[12] J. Pyrhönen, T. Jokinen and V. Hrabrovcova, "*Design of Rotating Electrica/ Machines",* John Wiley & Sons, 2008.

[13] S. Touhami, "*Analytical Sizing Models to Assess the Performances of High Specific Power Electric Motors for Hybrid Aircraft*", PhD thesis in Electrical Engineering, INP-Toulouse, September 2020.

[14] L. Branz, M. Degano, M. de Martin and A. Tessarolo, "*On the use of dimensioning equations for surface permanent magnet machines*", International Symposium on Power Eelectronics, Electrical Drives, Automation and Motion, Sorrento, Italy, 20-22 June 2012.

[15] A. Tessarolo et al, "*Explicit Torque and Back EMF Expressions for Slotless Surface Permanent Magnet Machines with Different Magnetization Patterns*", IEEE Transactions on Magnetics, vol. 52, n°8, August 2016.

[16] Daniel Closa, "*Conception, réalisation et essais de machines à aimants permanents et commutation électronique à encombrement axial réduit*", Thèse de Doctorat en Génie Electrique, Institut National Polytechnique, 1988.

[17] W. Zhao, T. A. Lipo and B. -I. Kwon, "*Comparative Study on Novel Dual Stator Radial Flux and Axial Flux Permanent Magnet Motors with Ferrite Magnets for Traction Application*," *IEEE Transactions on Magnetics*, vol. 50, no. 11, pp. 1-4, Nov. 2014

[18] T. Carpi, M. Bonnet, S. Touhami, Y. Lefevre and J.F. Llibre, "*Unified sizing model approach for radial and axial flux permanent magnet machines*", 24th International Conference on Electrical Machines (ICEM), Goteborg - Virtual Conference, Sweden, 23-26 August 2020.

[19] M. Lee, K. Nam and J. KIm,"*Optimizing PM Coverage Ratio in Flux Concentrating Axial Flux Machine*", IEEE Energy Conversion Congress and Exposition (ECCE), Milwaukee, WI, USA, 18-22 September 2016.

[20] F. Zhao, T. A. Lipo and B-I Kwon, "*Novel Dual-Stator Axial-Flux Spoke-Type Permanent Magnet Vernier Machine for Direct-Drive Applications*", IEEE Transactions on Magnetics, vol. 50, n°11, November 2014.

[21] R. Benlamine, F. Dubas, S. -A. Randi, D. Lhotellier and C. Espanet, "*Modeling of an axial-flux interior PMs machine for an automotive application using magnetic equivalent circuit*," 18th International Conference on Electrical Machines and Systems (ICEMS), pp. 1266-1271, 2015.

[22] R. Benlamine, "*Etude et réalisation d'une machine électrique à forte densité de couple et fort rapport de sur couple pour des applications de traction automobile*". Thèse de l'Université de Franche-Comté, 2015.

[23] A. Z. Gbégbé, B. Rouached, J. Cros, M. Bergeron and P. Viarouge, "*Damper Currents Simulation of Large Hydro-Generator Using the Combination of FEM and Coupled Circuits Models*", *IEEE Transactions on Energy Conversion*, vol. 32, no. 4, pp. 1273-1283, Dec. 2017.

[24] A. Ferrero and A. Raciti, "*A digital method for the determination of the magnetic characteristic of variable reluctance motors*", IEEE Transactions on Instrumentation and Measurement, vol. 39, no. 4, pp. 604-608, Aug. 1990.

[25] R. Gobbi, N. C. Sahoo and R. Vejian, "*Experimental Investigations on Computer-Based Methods for Determination of Static Electromagnetic Characteristics of Switched Reluctance Motors*", IEEE Transactions on Instrumentation and Measurement, vol. 57, no. 10, pp. 2196-2211, Oct. 2008.

[26] K. Lu, P. O. Rasmussen and A. E. Ritchie, "*Investigation of Flux-Linkage Profile Measurement Methods for Switched-Reluctance Motors and Permanent-Magnet Motors*", IEEE Transactions on Instrumentation and Measurement, vol. 58, no. 9, pp. 3191-3198, Sept. 2009

[27] Y. Ait-gougam, R. Ibtiouen, O. Touhami, J.-P. Louis, M. Gabsi, "*Inverse modelling and pulsating torque minimization of salient pole non-sinusoidal synchronous machines*", Electric Power Systems Research,Volume 78, Issue 1, Pages 88-96, 2008.

[28] G. Gallicchio, M. Palmieri, E. Grasso, M. Nienhaus and F. Cupertino, "*Inductances Computation Using Finite Element Analysis for PMSM Sensorless Control*," 2020 IEEE International Conference on Power Electronics, Drives and Energy Systems (PEDES), pp. 1-6,2020.

[29] G. T. de Paula, J. R. B. de A. Monteiro, B. P. de Alvarenga, T. E. P. de Almeida, W. C. A. Pereira and M. P. de Santana, "*On-Load Back EMF of PMSM Using Maxwell Stress Tensor*", IEEE Transactions on Magnetics, vol. 54, no. 7, pp. 1-15, July 2018.

[30] C. Filho, B. P. de Alvarenga and G. T. de Paula, "*On-Load Apparent Inductance Derivative of IPMSM: Assessment Method and Torque Estimation*", IEEE Transactions on Magnetics, vol. 56, no. 4, pp. 1-10, April 2020.

[31] O. A. Mohammed, S. Liu and Z. Liu, " Physical Modeling of PM Synchronous Motors for Integrated Coupling with Machine Drives", IEEE Transactions on Magnetics, Vol. 41, n° 5, May 2005.

[32] G. Heins, M. Thiele and T. Brown, "*Accurate Torque Ripple Measurement for PMSM*", IEEE Transactions on Instrumentation and Measurement, vol. 60, no. 12, pp. 3868-3874, Dec. 2011.

[33] A. Pouramin, R. Dutta, M. Farshadnia and M. F. Rahman, "*A Standstill Method to Measure Electromagnetically Induced Torque Ripple of Permanent Magnet Synchronous Machines*", IEEE Transactions on Instrumentation and Measurement, vol. 69, no. 10, pp. 7627-7635, Oct. 2020.

[34] S. Song, L. Ge, S. Ma, M. Zhang and L. Wang, "*Accurate Measurement and Detailed Evaluation of Static Electromagnetic Characteristics of Switched Reluctance Machines*", IEEE Transactions on Instrumentation and Measurement, vol. 64, no. 3, pp. 704-714, March 2015.

[35] M. Lajoie-Mazenc, R. Carlson, J. Hector, and J.J. Pesque, " *Characterisation of a new machine with ferrite magnets by resolving the partial differential equation for the magnetic field*", Proc. IEE, vol. 124, n° 8, August 1977.

[36] J. Azzouzi, G. Barakat and B. Dakyo, "*Quasi-3-D analytical modeling of the magnetic field of an axial flux permanent-magnet synchronous machine*", IEEE Transactions on Energy Conversion, vol. 20, no. 4, pp. 746-752, Dec. 2005.

[37] J. Li, "*General explicit difference formulas for numerical differentiation*", Journal of Computational and Applied Mathematics, vol. 183, Issue 1, Pages 29-52, 2005.

[38] S. R.K. Iyengar and A. Goyal, "*A note on multigrid for the three-dimensional Poisson equation in cylindrical coordinates*", Journal of Computational and Applied Mathematics, Volume 33, Issue 2, Pages 163-169, 1990.

[39] A. Shiferaw and R. C. Mittal, "*An Efficient Direct Method to Solve the Three Dimensional Poisson's Equation*", American Journal of Computational Mathematics, vol. 1, n° 4, pp. 285-293,2011.

[40] A. Shiferaw and R. C. Mittal, "*Fast Finite Difference Solutions of the Three Dimensional Poisson's Equation in Cylindrical Coordinates*", American Journal of Computational Mathematics, vol. 3, n° 4, pp. 356-361, 2013.

[41] B. Nogarede, M. Lajoie-Mazenc and B. Davat. "*Modélisation analytique des machines à aimants à induit sans encoches* ", Revue de Physique Appliquée, pp.707-720, Juillet 1990.

[42] F. Scuiller, E. Semail and J.F. Charpentier. "*General modeling of the windings for multi-phase ac machines*», Eur. Phys. J. Appl. Phys., vol. 50, n° 3, June 2010.

[43] X. Liu, H. Hu, J. Zhao, A. Belahcen and L. Tang, "*Armature Reaction Field and Inductance Calculation of Ironless BLDC Motor*", IEEE Transactions on Magnetics, vol. 52, no. 2, pp. 1-14, Feb. 2016

[44] C. Liu, S. Zuo, S. Hu, S. Qu and Z. Wu, "*Quasi-3-D Nonlinear Analytical Modeling of Magnetic Field in Axial-Flux Switched Reluctance Motors*", *IEEE Transactions on Magnetics*, vol. 58, no. 3, pp. 1-12, March 2022

[45] J. F. Gieras, R. J. Wang and M. J. Kamper, *Axial Flux Permanent Magnet Brsuhless Machines*, Kluwer Academic Publishers, 2004.

[46] Cogent steels catalogue for "Electrical Steel Non Oriented Fully Processed.pdf", pages: 22-23, UK

[47] "Ferram 27/23" technical sheet from ARELEC SA, pages: 1-2, created in 01/04/2003

[48] Paul C. Krause, (2013), "Analysis of Electric Machinery and Drive Systems", Published by John Wiley & Sons, Inc., Hoboken, New Jersey. ISBN: 9781118024294.

[49] Sandip Mazumder, "Numerical Methods for Partial Differential Equations: Finite Difference and Finite Volume Methods", Publisher: Academic Press, Amesterdam, 2016, ISBN: 978-0-12-849894-1

[50] R. Haberman," Applied partial differential equations: with Fourier series and boundary value problems", Publsiher: Pearson, Boston, 5th edition, 2013, ISBN: 978-0-321-79705-6

[51] Brigham, E. Oran, "The fast Fourier transform and its applications", Publisher: Prentice Hall, Englewood Cliffs, N.J, 1988, ISBN: 978-0-13-307505-2

[52] Franck Scuiller, "Dévelopment d'outils de conception de machines polyphasées à aimants utilisant l'approche multimachine", PhD thesis, "Ecole Nationale Supérieure d'Arts et Metiers", 2006

[53] A. Mrad, Y. Lefevre, J. -F. Llibre, M. Arnaout and C. Nadal, "3D Finite Difference Model of the Open Circuit Field of Permanent Magnet Spoke Type Axial Flux Machines," *2021 IEEE International Workshop of Electronics, Control, Measurement, Signals and their application to Mechatronics (ECMSM)*, 2021

[54] T. Carpi, Y. Lefèvre, C. Hénaux, J. F. Llibre and D. Harribey, "3-D Hybrid Model of the Axial-Flux Motor Accounting Magnet Shape", IEEE *Transactions on Magnetics*, vol. 58, no. 5, pp. 1-4, May 2022.